

The Dekel-Zhao profile: A mass-dependent dark-matter density profile with flexible inner slope and analytic potential, velocity dispersion, and lensing properties

Jonathan Freundlich,^{1,2★} Fangzhou Jiang,¹ Avishai Dekel,^{1,3} Nicolas Cornuault,¹ Omry Ginzburg,¹ Rémy Koskas,^{1,4} Sharon Lapiner,¹ Aaron Dutton,⁵ and Andrea V. Macciò^{5,6}

¹Centre for Astrophysics and Planetary Science, Racah Institute of Physics, The Hebrew University, Jerusalem 91904, Israel

²School of Physics and Astronomy, Tel Aviv University, Tel Aviv 69978, Israel

³Santa Cruz Institute for Particle Physics, University of California, Santa Cruz, CA 95064, USA

⁴École Nationale des Ponts et Chaussées, 77420 Champs-sur-Marne, France

⁵New York University Abu Dhabi, PO Box 129188, Saadiyat Island, Abu Dhabi, United Arab Emirates

⁶Max Planck Institute für Astronomie, Königstuhl 17, 69117 Heidelberg, Germany

Accepted 2020 September 9. Received 2020 September 9; in original form 2020 April 17.

ABSTRACT

We explore a function with two shape parameters for the dark-matter halo density profile subject to baryonic effects, which is a special case of the general Zhao family of models applied to simulated dark matter haloes by Dekel et al. This profile has variable inner slope and concentration parameter, and analytic expressions for the gravitational potential, velocity dispersion, and lensing properties. Using the NIHAO cosmological simulations, we find that it provides better fits than the Einasto profile and the generalized NFW profile with variable inner slope, in particular towards the halo centers. We show that the profile parameters are correlated with the stellar-to-halo mass ratio $M_{\text{star}}/M_{\text{vir}}$. This defines a mass-dependent density profile describing the average dark matter profiles in all galaxies, which can be directly applied to observed rotation curves of galaxies, gravitational lenses, and semi-analytic models of galaxy formation or satellite-galaxy evolution. The effect of baryons manifests itself by a significant flattening of the inner density slope and a 20% decrease of the concentration parameter for $M_{\text{star}}/M_{\text{vir}} = 10^{-3.5}$ to 10^{-2} , corresponding to $M_{\text{star}} \sim 10^{7-10} M_{\odot}$. The accuracy by which this profile fits simulated galaxies is similar to certain multi-parameter, mass-dependent profiles, but its fewer parameters and analytic nature make it most desirable for many purposes.

Key words: dark matter – galaxies:haloes – galaxies:evolution

1 INTRODUCTION

Dark matter (DM) halo density profiles in DM-only cosmological simulations are well described by the ‘NFW’ parametrization (Navarro et al. 1996, 1997; Springel et al. 2008; Navarro et al. 2010) from dwarf halos to large clusters, although with some systematic deviations (e.g., Navarro et al. 2004, 2010; Macciò et al. 2008; Gao et al. 2008; Springel et al. 2008). This density profile scales with radius as

$$\rho_{\text{NFW}}(r) = \frac{\rho_c}{x(1+x)^2}, \quad (1)$$

with $x = r/r_s$, r_s being a characteristic scale radius at which the density logarithmic slope equals 2 in absolute value. This radius

defines a concentration $c_{\text{DMO}} = R_{\text{vir}}/r_s$, which depends on the halo virial mass M_{vir} and redshift (e.g., Bullock et al. 2001; Wechsler et al. 2002; Dutton & Macciò 2014) – both M_{vir} and the virial radius R_{vir} being set by cosmology. The inner $\rho \propto r^{-1}$ ‘cusp’ of the NFW parametrization is at odds with observations of DM dominated dwarf, low-surface-brightness and dwarf satellite galaxies as well as clusters, which infer shallower ‘cores’ (e.g., Flores & Primack 1994; Moore 1994; McGaugh & de Blok 1998; van den Bosch & Swaters 2001; de Blok et al. 2008; de Blok 2010; Kuzio de Naray & Spekkens 2011; Oh et al. 2011, 2015; Newman et al. 2013a,b; Adams et al. 2014). The introduction of baryonic processes such as cooling, star formation and feedback resulting from star formation or active galactic nuclei (AGN) in the simulations can alleviate this ‘cusp-core discrepancy’ by transforming cusps into cores (e.g., Governato et al. 2010, 2012; Macciò et al. 2012,

★ E-mail: jonathan.freundlich@mail.huji.ac.il

2020; Zolotov et al. 2012; Martizzi et al. 2013; Teyssier et al. 2013; Di Cintio et al. 2014a; Chan et al. 2015; Tollet et al. 2016; Peirani et al. 2017).

Baryonic processes can affect DM haloes in different ways. When baryons cool slowly and accumulate at the center of a DM halo, they steepen the potential well, leading to an adiabatic contraction of the DM distribution and even more severe cusps (Blumenthal et al. 1986; Gnedin et al. 2004; Oñorbe et al. 2007). When a clump of gas or a satellite galaxy moves within the halo, it can transfer part of its orbital energy and angular momentum to the DM background through dynamical friction (Chandrasekhar 1943; Tremaine & Weinberg 1984). This latter process dynamically ‘heats’ the DM halo and has been shown to contribute to core formation (El-Zant et al. 2001, 2004; Tonini et al. 2006; Romano-Díaz et al. 2008; Del Popolo 2009; Goerdt et al. 2010; Cole et al. 2011; Nipoti & Binney 2015). When stellar winds, supernova explosions or AGNs generate outflows, they induce mass and potential fluctuations that can also dynamically heat the DM and form cores (Dekel & Silk 1986; Dekel et al. 2003a,b; Read & Gilmore 2005; Mashchenko et al. 2006, 2008; Peñarrubia et al. 2012; Pontzen & Governato 2012, 2014; Governato et al. 2012; Zolotov et al. 2012; Martizzi et al. 2013; Teyssier et al. 2013; Madau et al. 2014; Dutton et al. 2016b; El-Zant et al. 2016; Peirani et al. 2017; Freundlich et al. 2020). Other processes such as galactic bars (Weinberg & Katz 2002) or tidal effects at the halo outskirts (More et al. 2015) may also affect the DM distribution.

These different processes are reflected in hydrodynamical simulations, which display a variety of DM halo responses to the introduction of baryons, notably depending on stellar and halo masses. In particular, Di Cintio et al. (2014a), Chan et al. (2015), Tollet et al. (2016) and Dutton et al. (2016b) show that the inner slope of simulated DM haloes displays a minimum for stellar masses between 10^7 and $10^{10} M_\odot$ while it rises above the NFW slope when the stellar mass exceeds $10^{10} M_\odot$. This behaviour can be interpreted in terms of a competition between outflows induced by feedback and the confinement imposed by halo gravity (e.g., Dekel & Silk 1986; Peñarrubia et al. 2012): for very low stellar masses, the inner slope follows that of DM-only NFW haloes; between 10^7 and $10^{10} M_\odot$, outflows overcome halo gravity, leading to the expansion of the halo; above $10^{10} M_\odot$, the accumulation of baryons leads to adiabatic contraction, although the introduction of AGN feedback in simulations can partially counteract adiabatic contraction at high halo mass (Macciò et al. 2020). Hydrodynamical simulations of dwarf galaxies by Mashchenko et al. (2008), Madau et al. (2014), Verbeke et al. (2015), Read et al. (2016), and Dutton et al. (2016b) further suggest that the main parameter driving the halo response is the stellar-to-halo mass ratio rather than the stellar or halo mass itself. The different responses of the DM halo as well as the potentially smooth transition between cusps and cores motivates a parametrization of DM halo density profiles that would reflect the different halo shapes induced by baryonic physics or environment. In particular, a parametrization with free inner slope in addition to a free concentration parameter would enable to follow the transition between cusps and cores.

Different parametrizations allowing some inner slope flexibility have been proposed (Einasto 1965; Jaffe 1983; Hernquist 1990; Dehnen 1993; Evans 1994; Tremaine et al. 1994; Burkert 1995; Zhao 1996; Jing & Suto 2000; Navarro et al. 2004; Stoehr 2006; Merritt et al. 2006; An & Zhao 2013; Di Cintio et al. 2014a; Schaller et al. 2015; Oldham & Auger 2016; Dekel et al. 2017). Amongst them, the Einasto profile (Einasto 1965; Navarro et al. 2004; Mamon et al. 2010; Retana-Montenegro et al. 2012; An &

Zhao 2013) with two free shape parameters provides excellent fits to DM cusps and analytic expressions for the mass and the gravitational potential (involving incomplete gamma functions for the potential) as well as for the surface density, the deflection angle and the deflection potential relevant for lensing studies (involving Fox H functions, cf. Eq. (31) below for their definition and Retana-Montenegro et al. 2012), but does not seem to fully recover the innermost part of shallower density profiles (Dekel et al. 2017, and Section 3.2). Modified NFW and Einasto profiles allowing constant-density cores have been proposed by Read et al. (2016) and Lazar et al. (2020), but at the expense of analyticity (in particular, the analyticity of the concentration). The profile proposed by Dehnen (1993) and Tremaine et al. (1994) has the particularity to have analytic expressions for the mass, the gravitational potential, and the velocity dispersion (in terms of elementary functions) and, in certain cases, for the distribution function and the surface density (in terms of elementary functions for some of the cases), but its unique shape parameter does not allow to recover the diversity of DM haloes. More generally, Zhao (1996, hereafter Z96) shows that double power-law density profiles of the form

$$\rho(r) = \frac{\rho_c}{x^a(1 + x^{1/b})^{b(g-a)}} \quad (2)$$

where $x = r/r_c$, r_c a characteristic radius, and ρ_c a characteristic density, have analytic expressions for the gravitational potential, the enclosed mass, and the velocity dispersion (in terms of elementary functions) provided that $b = n$ and $g = 3 + k/n$, where n and k can be any natural numbers. Within this general Zhao family of profiles with four shape parameters (a , b , g , and the concentration $c = R_{\text{vir}}/r_c$ associated to the characteristic radius), Dekel et al. (2017, hereafter D17) show that the specific profile with $n = 2$ and $k = 1$, i.e., $b = 2$ and $g = 3.5$ in Eq. (2), provides excellent fits for DM haloes in simulations with and without baryons, ranging from steep cusps to flat cores. This specific profile with two remaining shape parameters (a and c), hereafter referred to as the Dekel-Zhao (DZ) profile, notably captures cores better than the Einasto profile. In Freundlich et al. (2020, hereafter F20), we accordingly used it to model the cusp-core transformation by outflow episodes induced by feedback, and further derived analytic expressions for the velocity dispersion in such DM halos with additional fiducial baryonic mass distributions (in terms of incomplete beta functions). We note that Zhao (1997) provides analytic approximations for the distribution function and the projected line-of-sight velocity dispersion of this profile, while An & Zhao (2013, hereafter AZ13) offers a general parametrization of density profiles¹ that includes both double power-law profiles (including the NFW and other profiles) and the Einasto profile, with general analytic expressions for the gravitational potential, the enclosed mass, the velocity dispersion (in terms of incomplete beta and gamma functions), and the surface density (in terms of Fox H functions).

Without being concerned by the non-analyticity of the potential and kinetic energy associated with most density profiles given by Eq. (2), Di Cintio et al. (2014a) analyse a suite of hydrodynamical simulations to obtain functional forms for the shape parameters a, b, g and the concentration parameter associated to r_c

¹ The AZ13 parametrisation is characterized by a logarithmic density slope

$$\frac{d \ln \rho}{d \ln r} = -\frac{a + x^{1/b}}{1 + s x^{1/b}}, \quad (3)$$

which leads to Eq. (2) with $g = s^{-1}$ for the density profile when $s > 0$ and to the Einasto density profile when $s = 0$ (cf. their equations (5a) and (6a)).

as a function of the stellar-to-halo mass ratio $M_{\text{star}}/M_{\text{vir}}$ at redshift $z = 0$. This enables them to define a mass-dependent density profile (hereafter **Di Cintio+**) for DM haloes, whose parameters are entirely set by the stellar and halo masses and which reflects the halo response to baryonic processes, since $M_{\text{star}}/M_{\text{vir}}$ represents an integrated star formation efficiency including the effects of feedback. The **Di Cintio+** profile not only enables to fit simulated DM distributions, but it is widely used to model observed rotation curves (e.g. [Allaert et al. 2017](#); [van Dokkum et al. 2019](#); [Wasserman et al. 2019](#); [Cautun et al. 2020](#)) and at times to parametrize semi-analytical models of satellite evolution (e.g. [Carleton et al. 2019](#)). It however lacks analytic expressions for the gravitational potential, the velocity dispersion, and lensing properties such as the projected surface density and mass, the deflection angle and the magnification.

In the present article, we review the analytic properties of the DZ parametrization of DM density profiles, as established in [Z96](#), [AZ13](#), [D17](#), and [F20](#), and further derive expressions for its lensing properties in terms of Fox H functions and series expansions. We systematically test this parametrization in a large suite of cosmological hydrodynamical zoom-in simulations, compare it both to the **Einstein** model and the generalized NFW model with variable inner slope, and obtain the dependences of its two shape parameters on stellar and halo mass. This enables us to establish it as a mass-dependent profile including the influence of baryons, whose accuracy is comparable to the **Di Cintio+** profile but with the advantage of having analytic expressions for the gravitational potential and the velocity dispersion. We further give an integral expression for its associated isotropic distribution function. This model can be directly applied to model rotation curves for assessing halo masses, and also to gravitational lenses and semi-analytical models.

This article unfolds as follows: in Section 2, we recall the analytic properties of the spherically-symmetric DZ profile, in particular its associated gravitational potential and velocity dispersion, and derive analytic expressions for its lensing properties; in Section 3, we systematically test the profile in the NIHAO suite of hydrodynamical cosmological simulations ([Wang et al. 2015](#)) and quantify the mass-dependence of its two free parameters, the inner logarithmic slope s_1 and the concentration c_2 ; in Section 4, we provide prescriptions to describe DM haloes given their stellar and halo masses and to model rotation curves with the DZ profile.

2 ANALYTICS

2.1 General case

2.1.1 Mean density profile

To describe the transition from cusps to cores and alterations of the DM distribution due to environmental effects while enabling straightforward analytic expressions of the density, mass and circular velocity profiles of DM haloes, [D17](#) proposed a functional form similar to Eq. (2) for the *mean* density profile within a sphere of radius r ,

$$\bar{\rho}(r) = \frac{\bar{\rho}_c}{x^a(1 + x^{1/b})^{b(\bar{g}-a)}}, \quad (4)$$

where $\bar{\rho}_c$ is a characteristic density, $x = r/r_c$ with $r_c = R_{\text{vir}}/c$ an intermediate characteristic radius, a and \bar{g} the inner and outer asymptotic slopes, b a middle shape parameter and c a concentration parameter. The normalisation factor $\bar{\rho}_c$ can be expressed as $\bar{\rho}_c = c^3 \mu \bar{\rho}_{\text{vir}}$, with $\mu = c^{a-3}(1 + c^{1/b})^{b(\bar{g}-a)}$, and $\bar{\rho}_{\text{vir}} = 3M_{\text{vir}}/4\pi R_{\text{vir}}^3$ the mean mass density within R_{vir} . As the virial radius R_{vir} is set by

cosmology for a given halo mass through $\bar{\rho}_{\text{vir}} = \Delta \rho_{\text{crit}}$ with Δ the overdensity, this functional form effectively depends on four shape parameters: a , b , \bar{g} and c .

2.1.2 Mass, velocity, force and density profiles

The enclosed mass, circular velocity, and force profiles stemming from Eq. (4) can be expressed as

$$M(r) = \frac{4\pi r^3}{3} \bar{\rho}(r) = \mu M_{\text{vir}} x^3 \bar{\rho}(r) / \bar{\rho}_c, \quad (5)$$

$$V^2(r) = \frac{GM(r)}{r} = c \mu V_{\text{vir}}^2 x^2 \bar{\rho}(r) / \bar{\rho}_c \quad (6)$$

and

$$F(r) = -\frac{GM(r)}{r^2} = -c^2 \mu F_{\text{vir}} x \bar{\rho}(r) / \bar{\rho}_c \quad (7)$$

where $V_{\text{vir}}^2 = GM_{\text{vir}}/R_{\text{vir}}$ and $F_{\text{vir}} = -GM_{\text{vir}}/R_{\text{vir}}^2$. In turn, the density profile is obtained by derivating the expression of the enclosed mass:

$$\rho(r) = \frac{1}{4\pi r^2} \frac{dM}{dr} = \frac{3-a}{3} \left(1 + \frac{3-\bar{g}}{3-a} x^{1/b} \right) \frac{1}{1+x^{1/b}} \bar{\rho}(r). \quad (8)$$

This expression reduces to Eq. (2) when $\bar{g} = 3$, with $g = 3 + 1/b$ and $\rho_c = (1 - a/3)\bar{\rho}_c$. More generally, each term of Eq. (8) is analogous to Eq. (2) with $g = \bar{g} + 1/b$ so the results of [Z96](#) apply: this density profile allows analytic expressions for the gravitational potential and the velocity dispersion provided that $b = n$ and $\bar{g} = 3 + k/n$, where n is a natural number and k a positive or null integer.

2.1.3 Inner slope and concentration

In the density profile derived from Eq. (4), the shape parameter a may not be the slope at the resolution limit ($0.01R_{\text{vir}}$ in the case of the NIHAO simulations, cf. [Wang et al. 2015](#)) and c does not necessarily reflect the actual concentration of the halo as for an NFW profile. The logarithmic slope of the density profile expressed in Eq. (8) is

$$s(r) = -\frac{d \ln \rho}{d \ln r} = \frac{a + (\bar{g} + b^{-1})x^{1/b}}{1 + x^{1/b}} - \frac{3 - \bar{g}}{3 - a} \frac{b^{-1}x^{1/b}}{1 + \frac{3-\bar{g}}{3-a}x^{1/b}}, \quad (9)$$

so $s_1 = s(0.01R_{\text{vir}})$ measures the inner logarithmic slope at the resolution limit in the NIHAO simulations. This Eq. (9) further enables to define a concentration parameter c_2 similar to the NFW parameter, corresponding to the radius r_2 at which the logarithmic slope s of the density profile equals 2. This radius is such that

$$c_2 \equiv \frac{R_{\text{vir}}}{r_2} = c \left(\frac{\bar{g} + b^{-1} - 2}{2 - a} \right)^b, \quad (10)$$

which coincides with c when $a + \bar{g} + b^{-1} = 4$. Another concentration parameter, c_{max} , can be defined from the radius r_{max} at which the circular velocity peaks (cf. Appendix A). The logarithmic slope at the resolution limit (s_1 for the NIHAO simulations) and c_2 (or c_{max}) can be used as effective inner slope and concentration when describing the density profile.

2.2 The Dekel-Zhao profile

Using three pairs of simulated haloes at different masses with and without baryons at $z = 0$ from the NIHAO suite of simulations ([Wang et al. 2015](#)), [D17](#) show that the functional form of Eq. (8)

with $b = 2$ and $\bar{g} = 3$ yields excellent fits for haloes ranging from steep cusps to flat cores. They notably show that this parametrization, here referred to as the Dekel-Zhao (DZ) profile, matches simulated profiles better than the NFW and Einasto profiles, capturing cores better, in addition to providing fully analytic expressions for the density, the mass, the gravitational potential, and the velocity dispersion. We further show in F20 that density profile fits using this parametrization enable to recover the simulated gravitational potentials and the velocity dispersions of simulated haloes. The upper left panel of Fig. 1 highlights the variety of density profiles from cusps to cores that can be described by the DZ profile, with four examples of different inner slope ($s_1 = 0$ and 1) and concentration ($c_2 = 5$ and 15). These fiducial examples correspond to different rotation curves, velocity dispersions, gravitational potentials and distribution functions.

In the following subsections, we recall the analytic expressions of the gravitational potential and velocity dispersion. In Section 2.3, we obtain analytic expressions for quantities relevant to gravitational lensing. In Appendix A, we further express the DZ profile in terms of r_{\max} and V_{\max} , which can notably be useful to describe satellite haloes (e.g., Jiang et al. 2020). In Appendices B and C, we recall sum expressions for the velocity dispersion obtained by Z96 and F20, which enable to express this quantity in terms of elementary functions, as well as expressions for the velocity dispersion in haloes with fiducial baryonic components from F20. In Appendix D, we give an integral expression of the distribution function. Finally, in the next Sections 3 and 4, we test the DZ profile over the whole NIHAO suite of simulations and establish it as a mass-dependant profile whose shape parameters s_1 and c_2 only depend on the stellar-to-halo mass ratio.

2.2.1 Shape parameters

Introducing $\bar{g} = 3$ and $b = 2$ in Eq. (8), the DZ density profile is

$$\rho(r) = \frac{\rho_c}{x^a(1 + x^{1/2})^{2(3.5-a)}} \quad (11)$$

with $x = r/r_c$, $\rho_c = (1 - a/3)\bar{\rho}_c$ while $\bar{\rho}_c = c^3\mu\bar{\rho}_{\text{vir}}$, $\mu = c^{a-3}(1 + c^{1/2})^{2(3-a)}$ and $\bar{\rho}_{\text{vir}} = 3M_{\text{vir}}/4\pi R_{\text{vir}}^3$, and two shape parameters a and $c = R_{\text{vir}}/r_c$. The inner logarithmic slope s_1 at the resolution r_1 from Eq. (9) is

$$s_1 = \frac{a + 3.5c^{1/2}(r_1/R_{\text{vir}})^{1/2}}{1 + c^{1/2}(r_1/R_{\text{vir}})^{1/2}}, \quad (12)$$

while the concentration parameters is

$$c_2 = c \left(\frac{1.5}{2-a} \right)^2. \quad (13)$$

A positive density imposes $a \leq 3$, a positive inner logarithmic slope $a + 3.5c^{1/2}(r_1/R_{\text{vir}})^{1/2} \geq 0$; negative values of a can be compatible with a positive logarithmic slope at the resolution limit, in particular for large values of c . Since the logarithmic slope tends to a when the radius goes to zero, c_2 is only defined when $a \leq 2$.

There are bijections between the couples (a, c) and (s_1, c_2) (and (s_1, c_{\max}) , cf. Appendix A) so these couples are equivalent in describing the density profile. Indeed, a and c can be expressed as functions of s_1 and c_2 ,

$$a = \frac{1.5s_1 - 2(3.5 - s_1)(r_1/R_{\text{vir}})^{1/2}c_2^{1/2}}{1.5 - (3.5 - s_1)(r_1/R_{\text{vir}})^{1/2}c_2^{1/2}} \quad (14)$$

and

$$c = \left(\frac{s_1 - 2}{(3.5 - s_1)(r_1/R_{\text{vir}})^{1/2} - 1.5c_2^{-1/2}} \right)^2. \quad (15)$$

In the following, analytic expressions are expressed in terms of (a, c) while numerical tests focus on (s_1, c_2) . Eqs. (12), (13), (14), and (15) enable to switch from the two couples of parameters at will.

It is further possible to define a core radius r_{core} corresponding to a given value of the logarithmic slope, namely

$$r_{\text{core}} = \frac{R_{\text{vir}}}{c} \left(\frac{s_{\text{core}} - a}{3.5 - s_{\text{core}}} \right)^2 \quad (16)$$

with $s_{\text{core}} = s(r_{\text{core}})$. Since the logarithmic slope s is an increasing function of radius with $s(r = 0) = a$, this equation is only valid when $s_{\text{core}} \geq a$. We find that $s_{\text{core}} = 1$ enables to retrieve a radius close to what one's eye identifies as a core (cf. Fig. 1). This value also corresponds to the slope at the core radius of a pseudo-isothermal halo. Moreover, we note from Fig. 8 below that $s_1 = 1$ lies right below the 1σ scatter of the inner slope s_1 at low mass and hence marks the threshold below which core formation occurs. By analogy with the Burkert (1995) and ‘‘Lucky13’’ (Li et al. 2020) cored profiles, one could also choose $s_{\text{core}} = 1.5$. We point out that the slopes at the core radii of the ‘‘core-NFW’’ (Read et al. 2016) and ‘‘core-Einasto’’ (Lazar et al. 2020) profiles are not fixed to a specific value. At given a and c , the core radii from Eq. (16) defined at different s_{core} can be related to one another through constant factors depending only on a .

Eq. (5) also enables to express the half-mass radius, or more generally the radius

$$r_f = \frac{R_{\text{vir}}}{c} \left(\left(\frac{\mu}{f} \right)^{1/(6-2a)} - 1 \right)^{-2} \quad (17)$$

enclosing a DM mass $M(r_f) = fM_{\text{vir}}$. The half-mass radius of a DZ halo truncated at the virial radius corresponds to $f = 0.5$ in this equation. We stress that neither the cuspy NFW profile, nor the cored pseudo-isothermal, Burkert (1995), and ‘‘Lucky13’’ (Li et al. 2020) profiles, nor the Einasto, ‘‘core-Einasto’’ (Lazar et al. 2020), ‘‘core-NFW’’ (Read et al. 2016), and generalized NFW profiles with flexible inner slope have analytic expressions for the half-mass radius and therefore r_f (cf. also the table of Fig. 15).

2.2.2 Gravitational potential

The mass, circular velocity, force and logarithmic slope profiles of the DZ profile can be expressed analytically from Eqs. (5), (6), (7), and (9) with $b = 2$ and $\bar{g} = 3$. Its density (Eq. (11)) follows the form of Eq. (2) with $b = 2$ and $g = 3 + 1/2$ so the DZ profile also allows analytic expressions for the gravitational potential and the velocity dispersion (Z96).

Assuming that the gravitational potential vanishes at infinity and that the halo density profile is truncated at the virial radius yields the gravitational potential per unit mass ²

$$U(r) = -\frac{GM_{\text{vir}}}{R_{\text{vir}}} - \int_r^{R_{\text{vir}}} \frac{GM(y)}{y^2} dy = -V_{\text{vir}}^2 \left(1 + 2c\mu \int_x^{x_c} \zeta^{3-2a}(1-\zeta) d\zeta \right) \quad (18)$$

within the virial radius, with $V_{\text{vir}}^2 = GM_{\text{vir}}/R_{\text{vir}}$, $x = r/r_c$,

² We use the variable change $\zeta = z^{1/2}/(1 + z^{1/2})$ with $z = y/r_c$, which is such that $z^{1/2} = \zeta/(1 - \zeta)$, $1 + z^{1/2} = 1/(1 - \zeta)$, and $dz = 2\zeta(1 - \zeta)^{-3} d\zeta$.

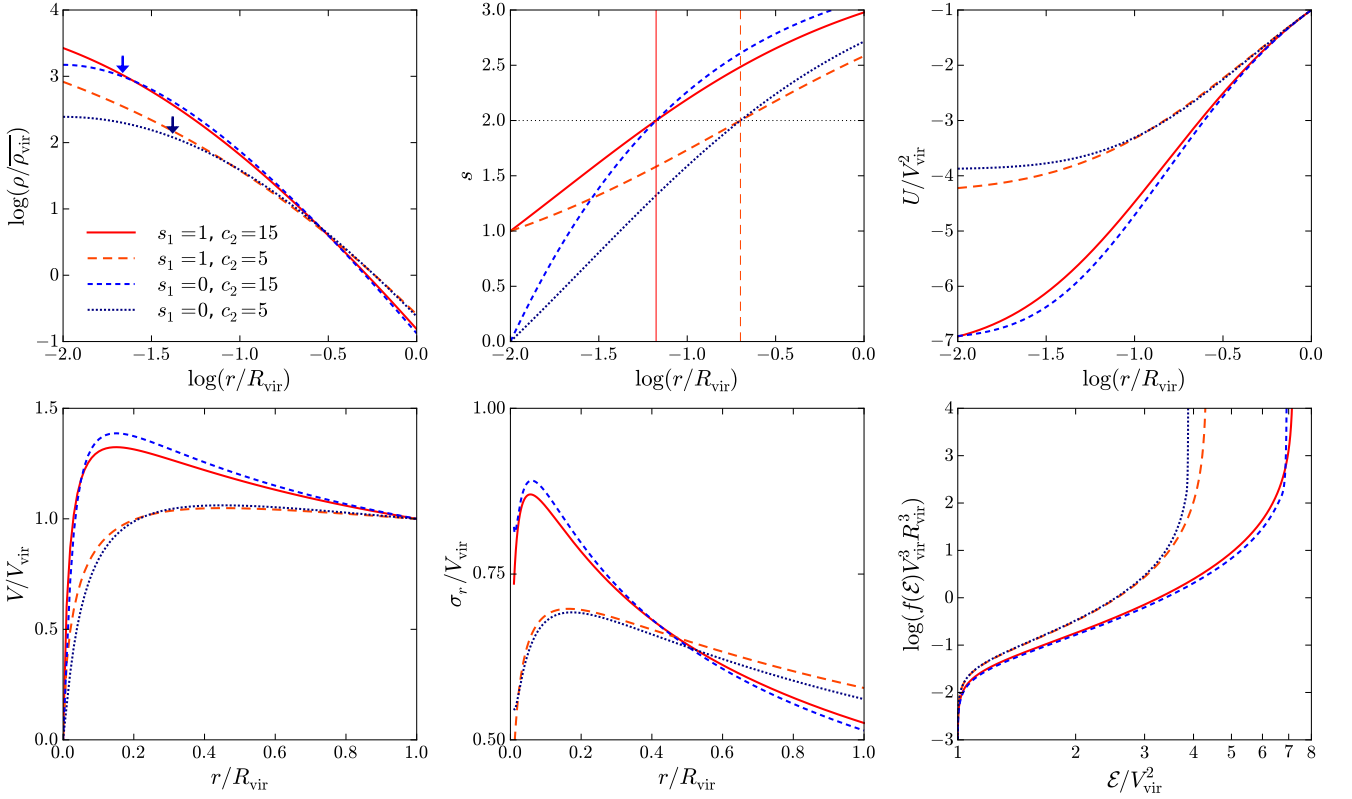


Figure 1. Fiducial DZ profiles: density (ρ), logarithmic slope (s), circular velocity (V), radial velocity dispersion (σ_r), and gravitational potential per unit mass (U) as a function of radius as well as the distribution function $f(\mathcal{E})$ associated to four DZ haloes truncated at the virial radius with different inner slope ($s_1 = 0$ or 1) and concentration ($c_2 = 5$ or 15). Eqs. (11), (9), (6), (22), (19) respectively provide analytic expressions for the radial profiles, while the distribution function is obtained by numerically integrating Eq. (D6). Arrows in the upper left panel indicate for the two cored profiles the core radii defined by Eq. (16) with $s_{\text{core}} = 1$. The vertical lines in the upper middle panel highlight the radius $r_2 = R_{\text{vir}}/c_2$ where $s = 2$. Dimensional quantities are in virial units, with $\bar{\rho}_{\text{vir}} = 3M_{\text{vir}}/4\pi R_{\text{vir}}^3$ and $V_{\text{vir}} = \sqrt{GM_{\text{vir}}/R_{\text{vir}}}$. The DZ profile enables to capture a variety of DM density profiles from cusps to cores with different concentrations. The concentration c_2 sets the depth of the potential well and hence the behaviours of the circular velocity, velocity dispersion, and distribution function.

$\chi = x^{1/2}/(1+x^{1/2})$, and $\chi_c = c^{1/2}/(1+c^{1/2})$. When $a \neq 2$ and $a \neq 5/2$, this yields³

$$U(r) = -V_{\text{vir}}^2 \left(1 + 2c\mu \left[\frac{\chi_c^{2(2-a)} - \chi^{2(2-a)}}{2(2-a)} - \frac{\chi_c^{2(2-a)+1} - \chi^{2(2-a)+1}}{2(2-a)+1} \right] \right). \quad (19)$$

As noted in Zhao (1997) and AZ13, Eq. (18) and hence Eq. (19) can be rewritten in terms of incomplete beta functions (cf. also Appendix C1).

2.2.3 Velocity dispersion

The equilibrium of a spherical collisionless system can be described by the spherical Jeans equation stemming from the Boltzmann equation (Binney & Tremaine 2008, Eq. (4.215)), which yields the radial velocity dispersion

$$\sigma_r^2(r) = \frac{G}{\rho(r)} \int_r^{R_{\text{vir}}} \rho(r') M(r') r'^{-2} dr' \quad (20)$$

for a halo truncated at the virial radius when the anisotropy parameter $\beta \equiv 1 - \sigma_t^2/2\sigma_r^2$, where σ_t is the tangential velocity dispersion, is

³ If $a = 2$, it instead yields $U(r) = -V_{\text{vir}}^2 (1 + 2c\mu[\ln(\chi_c/\chi) + \chi - \chi_c])$ and if $a = 5/2$, $U(r) = -V_{\text{vir}}^2 (1 + 2c\mu[1/\chi - 1/\chi_c - \ln(\chi_c/\chi)])$ but such specific rational values of a are unlikely to arise from fits.

null (isotropic case) and the boundary condition is $\lim_{r \rightarrow +\infty} \sigma_r^2 = 0$. For a DZ density profile as in Eq. (11), this leads to

$$\sigma_r^2(r) = 2c\mu \frac{GM_{\text{vir}}}{R_{\text{vir}}} \frac{\rho_c}{\rho(r)} \int_{\chi}^{\chi_c} \zeta^{3-4a} (1-\zeta)^8 d\zeta, \quad (21)$$

or

$$\sigma_r^2(r) = 2c\mu \frac{GM_{\text{vir}}}{R_{\text{vir}}} \frac{\rho_c}{\rho(r)} \left[\mathcal{B}(4-4a, 9, \zeta) \right]_{\chi}^{\chi_c} \quad (22)$$

where $\mathcal{B}(a, b, x) = \int_0^x t^{a-1} (1-t)^{b-1} dt$ is the incomplete beta function and the brackets denote the difference of the enclosed function between 1 and χ , i.e., $[f(\zeta)]_{\chi}^{\chi_c} \equiv f(\chi_c) - f(\chi)$. We extend here the definition of the incomplete beta function appearing inside the brackets to negative parameters since the integral of Eq. (21) is well-defined as long as $\chi > 0$ such that the bracketed term is also well-defined. This equation is a specific case of Eq. (B6) of AZ13, and it can further be expressed in terms of finite sums (Z96, F20), as recalled in the present Appendix B. The sum expressions enable to express the velocity dispersion in terms of elementary functions.

In Appendix C, we further recall expressions from Appendix B of F20 for the velocity dispersion in haloes with baryons (i) where the ratio between the DM and the total masses follows a power-law, (ii) where the baryons are concentrated to a central point mass, (iii) where they constitute a uniform sphere, (iv) where they constitute a singular isothermal sphere, and (v) where they themselves follow the DZ profile.

When the anisotropy parameter β is constant but not necessarily equal to zero, the Jeans equation corresponds to a differential equation in $\rho\sigma_r^2$ whose solution is

$$\sigma_r^2(r) = \frac{G}{r^{2\beta}\rho(r)} \int_r^{R_{\text{vir}}} \rho(r') M(r') r'^{2\beta-2} dr' \quad (23)$$

assuming that $\lim_{r \rightarrow +\infty} \sigma_r^2 = 0$ (Binney & Tremaine 2008, Eq. (4.216)). Following similar steps as for Eq. (22), this leads to

$$\sigma_r^2(r) = 2c\mu \frac{GM_{\text{vir}}}{R_{\text{vir}}} \frac{\rho_c}{\rho(r)} \frac{1}{x^{2\beta}} \left[\mathcal{B}(4-4a+4\beta, 9+4\beta, \zeta) \right]_{\chi}^{\chi_c}. \quad (24)$$

2.3 Lensing properties

2.3.1 Surface density

The mass surface density of a spherically-symmetric lens is obtained by integrating the three-dimensional density profile along the line of sight,

$$\Sigma(R) = \int_{-\infty}^{+\infty} \rho(r) dz \quad (25)$$

where R is the projected radius measured from the center of the lens and $r = \sqrt{R^2 + z^2}$ is the three-dimensional radius. This expression can be written as the Abel transform

$$\Sigma(R) = 2 \int_R^{+\infty} \frac{\rho(r) r dr}{\sqrt{r^2 - R^2}}, \quad (26)$$

which yields

$$\Sigma(X) = 2\rho_c r_c \int_X^{\infty} \frac{xdx}{x^a(1+x^{1/2})^{2(3.5-a)} \sqrt{x^2 - X^2}} \quad (27)$$

with $X = R/r_c$ and $c = R_{\text{vir}}/r_c$ for a DZ density profile truncated at the virial radius. This integral can be broken into two terms such that $\Sigma(X) = \tilde{\Sigma}(X) - \tilde{\Sigma}(c)$ with

$$\tilde{\Sigma}(X) = 2\rho_c r_c \int_X^{\infty} \frac{xdx}{x^a(1+x^{1/2})^{2(3.5-a)} \sqrt{x^2 - X^2}} \quad (28)$$

the surface density associated with an untruncated DZ profile. When $a < 1$, this expression yields at the center

$$\tilde{\Sigma}(0) = 4\rho_c r_c \mathcal{B}(2-2a, 5) \quad (29)$$

with the variable change used to obtain Eqs. (19) and (22). However, the integral can not be easily expressed in terms of elementary functions for all values of a when $X \neq 0$. Following Mazure & Capelato (2002), Baes & van Hese (2011), Baes & Gentile (2011) and Retana-Montenegro et al. (2012), who expressed similar integrals involving Sérsic and Einasto profiles in terms of the Meijer G and Fox H functions, we use the Mellin transform method (Marichev 1983; Adamchick 1996; Fikioris 2007) to evaluate it as the Mellin-Barnes integral

$$\tilde{\Sigma}(R) = 4\sqrt{\pi}\rho_c r_c \frac{X}{2\pi i} \int_{\mathcal{L}} \frac{\Gamma(4y-2a)\Gamma(7-4y)}{\Gamma(7-2a)} \frac{\Gamma(y-\frac{1}{2})}{\Gamma(y)} [X^2]^{-y} dy \quad (30)$$

where \mathcal{L} is a vertical line in the complex plane (cf. Appendix E). This integral can be recognized as a Fox H function (e.g., Fox 1961; Mathai & Saxena 1978; Srivastava et al. 1982; Kilbas & Saigo 1999, 2004; Mathai et al. 2009), which is generally defined as the inverse Mellin transform of a product of gamma functions,

$$H_{p,q}^{m,n} \left[\begin{matrix} (\mathbf{a}, \mathbf{A}) \\ (\mathbf{b}, \mathbf{B}) \end{matrix} \middle| z \right] = \frac{1}{2\pi i} \int_{\mathcal{L}} \frac{\prod_{j=1}^m \Gamma(b_j + B_j y) \prod_{j=1}^n \Gamma(1 - a_j - A_j y)}{\prod_{j=m+1}^q \Gamma(1 - b_j - B_j y) \prod_{j=n+1}^p \Gamma(a_j + A_j y)} z^{-y} dy \quad (31)$$

where the couples (\mathbf{a}, \mathbf{A}) and (\mathbf{b}, \mathbf{B}) indicate the coefficients in the gamma functions with $A_j, B_j > 0$ and a_j, b_j complex numbers while $0 \leq m \leq q$ and $0 \leq n \leq p$ are integers. With this definition, the surface density associated with the untruncated DZ profile can be compactly written as

$$\tilde{\Sigma}(X) = \frac{4\sqrt{\pi}\rho_c r_c}{\Gamma(7-2a)} X H_{2,2}^{2,1} \left[\begin{matrix} (-6, 4), (0, 1) \\ (-\frac{1}{2}, 1), (-2a, 4) \end{matrix} \middle| X^2 \right]. \quad (32)$$

This expression has explicit series expansions depending on the nature of the poles of the gamma functions at the denominator of the integrand of the Mellin-Barnes integral (e.g., Kilbas & Saigo 1999; Baes & Gentile 2011), which are given in Appendix F. We note that Eq. (32) is a specific case of Eq. (C1) of AZ13, which includes both other double power-law profiles and the Einasto profile, and that AZ13 also provide analytic expressions for the limiting behaviours of this surface density when $X \rightarrow 0$ and $X \rightarrow \infty$ in terms of elementary functions.

The cumulative mass contained within an infinite cylinder of radius R is

$$\tilde{\mathcal{M}}(R) = 2\pi \int_0^R \tilde{\Sigma}(R') R' dR' \quad (33)$$

for an untruncated DZ profile and $\mathcal{M}(R) = \tilde{\mathcal{M}}(R) - \pi R^2 \tilde{\Sigma}(c)$ for a DZ profile truncated at the virial radius. Injecting Eq. (30) and inverting the two integrals involved yields

$$\tilde{\mathcal{M}}(X) = \frac{4\pi^{3/2}\rho_c r_c^3}{\Gamma(7-2a)} X^3 H_{3,3}^{2,2} \left[\begin{matrix} (-6, 4), (-\frac{1}{2}, 1), (0, 1) \\ (-\frac{1}{2}, 1), (-2a, 4), (-\frac{3}{2}, 1) \end{matrix} \middle| X^2 \right], \quad (34)$$

which also has an explicit series expansion (Appendix F).

2.3.2 Deflection angle

A gravitational lens deflects light from background sources depending on their projected distance R in the lens plane. The deflection angle $\hat{\alpha}(R)$ of a thin axially-symmetric lens where the distances between the source, the lens, and the observer are much larger than the size of the lens is directly related to its cumulative mass $\mathcal{M}(R)$ through

$$\hat{\alpha}(R) = \frac{4GM(R)}{c^2 R} \quad (35)$$

(Schneider et al. 1992, Eq. (8.5)), c being here the speed of light. Introducing D_L , D_S , and D_{LS} the angular distances respectively between the observer and the lens, between the observer and the source, and between the lens and the source, one can express the scaled deflection angle

$$\alpha(R) \equiv \frac{D_L D_{LS}}{r_c D_S} \hat{\alpha}(R) \quad (36)$$

and the convergence

$$\kappa(R) \equiv \frac{\Sigma(R)}{\Sigma_{\text{crit}}} \quad (37)$$

where distances in the lens plane are scaled in units of r_c and $\Sigma_{\text{crit}} = c^2 D_S / 4\pi G D_L D_{LS}$ is the lensing critical surface density. Introducing $\tilde{\kappa}_0 \equiv \tilde{\Sigma}(0)/\Sigma_{\text{crit}}$ with Eq. (29) and $\mathcal{B}(a, b) = \Gamma(a)\Gamma(b)/\Gamma(a+b)$, the scaled deflection angle for an untruncated DZ profile yields

$$\tilde{\alpha}(X) = \frac{\sqrt{\pi} \tilde{\kappa}_0}{\Gamma(2-2a)\Gamma(5)} X^2 H_{3,3}^{2,2} \left[\begin{matrix} (-6, 4), (-\frac{1}{2}, 1), (0, 1) \\ (-\frac{1}{2}, 1), (-2a, 4), (-\frac{3}{2}, 1) \end{matrix} \middle| X^2 \right], \quad (38)$$

which has a series expansion analogous to that of $\widetilde{M}(X)$. For a DZ profile truncated at the virial radius, $\alpha(X) = \widetilde{\alpha}(X) - X\widetilde{\Sigma}(c)/\Sigma_{\text{crit}}$. We give analytic expressions for the lensing potential in Appendix F.

For an axially-symmetric lens, multiple images occur if and only if the central convergence $\kappa_0 \equiv \Sigma(0)/\Sigma_{\text{crit}} > 1$ when the surface density does not increase with X , while there is only one image when $\kappa_0 \leq 1$ (Schneider et al. 1992, Section 8). If $a \geq 1$, the DZ profile has a singular surface density at the center and there can be multiple images for all masses. However if $a < 1$, the surface density is not singular and there can be multiple images only if $\kappa_0 > 1$.

2.3.3 Shear and magnification

The Jacobian between the unlensed and lensed coordinate systems depends on the convergence κ and on the lensing shear, which for an axially-symmetric lens reads

$$\gamma(X) \equiv \frac{\widetilde{\Sigma}(X) - \Sigma(X)}{\Sigma_{\text{crit}}} \quad (39)$$

with

$$\widetilde{\Sigma}(X) = \frac{2}{X^2} \int_0^X x \Sigma(x) dx \quad (40)$$

the average surface density within X . The average surface density for an untruncated DZ profile can be expressed as

$$\widetilde{\Sigma}(X) = \frac{4\sqrt{\pi}\rho_c r_c}{\Gamma(7-2a)} X H_{3.3}^{2.2} \left[\begin{matrix} (-6, 4), (-\frac{1}{2}, 1), (0, 1) \\ (-\frac{1}{2}, 1), (-2a, 4), (-\frac{3}{2}, 1) \end{matrix} \middle| X^2 \right] \quad (41)$$

in terms of a Fox H function while the average surface density of a DZ profile truncated at the virial radius is $\widetilde{\Sigma}(X) = \widetilde{\Sigma}(X) - \widetilde{\Sigma}(c)$. Both have series expansions (Appendix F). Eqs. (32), (41), and the definitions of the convergence κ (Eq. (37)) and of the shear γ (Eq. (39)) enable to determine the magnification factor $\mu(X) = [(1 - \kappa(X))^2 - \gamma^2(X)]^{-1}$ by which the source luminosity is amplified (Schneider et al. 1992, Eqs. (5.21) and (5.25)). This factor, which is the inverse of the determinant of the Jacobian between the unlensed and lensed coordinate systems, comprises of a term depending on the convergence κ that describes the isotropic focussing of the light rays in the lens plane and of a term depending on the shear γ that accounts for the anisotropic focusing due to the tangential stretching of the image.

Fig. 2 displays the radial profiles of some of the lensing properties of the four fiducial DZ haloes of different inner slope and concentration shown in Fig. 1, assumed to be truncated at the virial radius. We note that the shear γ mainly depends on the concentration away from the halo center, with higher concentration leading to more shear, while steeper inner densities induce more shear near the center. The quantities expressed in this Section as well as those shown in Fig. 2 assume spherically-symmetric haloes. Generalizations to elliptical DZ haloes can be obtained by substituting the projected radius R with an expression depending on the ellipticity of the lens (e.g., Schneider et al. 1992; Golse & Kneib 2002; Meneghetti et al. 2003).

3 THE DEKEL-ZHAO PROFILE IN SIMULATIONS

3.1 The NIHAO simulations

We systematically test the DZ profile on the simulated DM haloes at $z = 0$ of the Numerical Investigation of a Hundred Astrophysical

Objects project (NIHAO; Wang et al. 2015), which provides a set of about 90 cosmological zoom-in hydrodynamical simulations run with the improved Smoothed Particle Hydrodynamics (SPH) code *gasoline2* (Wadsley et al. 2017). Each simulation is run at the same resolution with and without baryons, but we focus here on the hydrodynamical simulations including the effects of baryons. The simulations assume a flat Λ CDM cosmology with Planck Collaboration et al. (2014) parameters, namely $\Omega_m = 0.3175$, $\Omega_r = 0.00008$, $\Omega_\Lambda = 1 - \Omega_m - \Omega_r = 0.6824$, $\Omega_b = 0.0490$, $H_0 = 67.1 \text{ km s}^{-1} \text{ Mpc}^{-1}$, $\sigma_8 = 0.8344$ and $n = 0.9624$.

They include a subgrid model describing the turbulent mixing of metals and thermal energy (Wadsley et al. 2008), cooling via hydrogen, helium and other metal lines in a uniform ultraviolet ionizing and heating background (Shen et al. 2010) and star formation according to the Kennicutt-Schmidt relation when the temperature falls below 15000 K and the density reaches 10.3 cm^{-3} (Stinson et al. 2013). Stars inject energy back to their surrounding interstellar medium (ISM) through ionizing feedback from massive stars (Stinson et al. 2013) and supernovae (Stinson et al. 2006). During the pre-supernova feedback phase, 13% of the total stellar luminosity – which is typically $2 \times 10^{50} \text{ erg}$ per M_\odot of the entire stellar population over the 4 Myr preceding the explosion of high-mass stars – is ejected into the surrounding gas. During the supernova feedback phase, stars whose mass is comprised between 8 and 40 M_\odot eject 4 Myr after their formation both an energy $E_{\text{SN}} = 10^{51} \text{ erg}$ and metals into their surrounding ISM according to the blast-wave formalism described in Stinson et al. (2006). Cooling is delayed for 30 Myr inside the blast region to prevent the energy from supernova feedback to be radiated away. Without cooling, the added supernova energy heats the surrounding gas, which both prevents star formation and models the high pressure of the blastwave. AGN feedback is not included.

The NIHAO sample comprises isolated haloes chosen from dissipationless cosmological simulations (Dutton & Macciò 2014) with halo masses between $\log(M_{\text{vir}}/\text{M}_\odot) = 9.5 - 12.3$. Their merging histories, concentrations and spin parameters were not taken into account in the selection. The virial radius R_{vir} is defined as the radius within which the average total density is Δ times the critical density of the Universe, where Δ is defined according to Bryan & Norman (1998). The virial mass M_{vir} is the total mass enclosed within R_{vir} . The particle masses and force softening lengths are chosen to resolve the DM mass profile below 1% of the virial radius at all masses in order to resolve the half-light radius of the galaxies. Stellar masses, which are calculated within $0.15R_{\text{vir}}$, range from $5 \cdot 10^4$ to $2 \cdot 10^{11} \text{ M}_\odot$, i.e., from dwarfs to Milky Way sized galaxies, with morphologies, colors and sizes that correspond well with observations (e.g., Wang et al. 2015; Stinson et al. 2015; Dutton et al. 2016a). As shown by Tollet et al. (2016), Dutton et al. (2016b), D17, F20, and Macciò et al. (2020), NIHAO DM haloes display a variety of inner slopes ranging from steep cusps to flat cores, cores being more prevalent at $z = 0$ for stellar masses comprised between 10^7 and 10^{10} M_\odot .

3.2 Fitting procedure and results

3.2.1 Density profile fits and rotation curves

We fit the logarithm of the density profile of each simulated halo at $z = 0$ according to the DZ parametrisation (Eq. (11)) through a least-square minimization between $0.01R_{\text{vir}}$ (the resolution limit) and R_{vir} . Since R_{vir} and M_{vir} are set, a and c are the only free parameters. We impose the inner logarithmic slope at the resolution

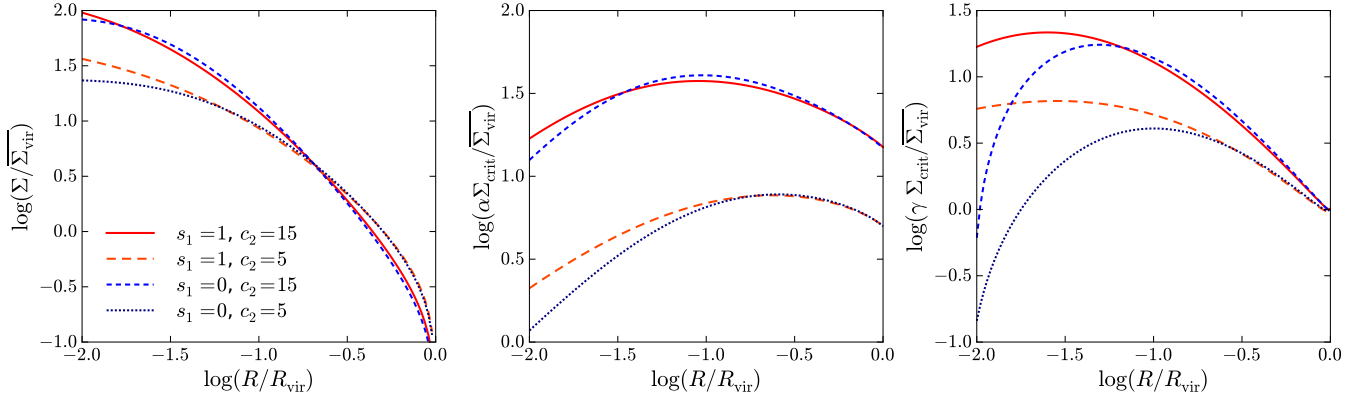


Figure 2. Lensing properties of fiducial spherical DZ DM haloes: two-dimensional projected surface density (Σ), scaled deflection angle (α), and lensing shear (γ) as a function of the projected radius in the lens plane (R) for the four DZ haloes truncated at the virial radius with different inner slope ($s_1 = 0$ or 1) and concentration ($c_2 = 5$ or 15) of Fig. 1. Eqs. (32), (38), and (41) as well as the series expansions of Appendix F provide analytical expressions for the different profiles. Quantities are normalized by $\bar{\Sigma}_{\text{vir}} = M_{\text{vir}}/\pi R_{\text{vir}}^2$ and $\Sigma_{\text{crit}} = c^2 D_S/4\pi G D_L D_{LS}$, with c being here the speed of light and D_L , D_S , D_{LS} the distances respectively between the observer and the lens, between the observer and the source, and between the lens and the source. While the deflection angle mainly depends on the concentration c_2 , the shear towards the center is very sensitive to the inner slope s_1 .

limit to be positive, namely $s_1 \geq 0$ with $s_1 = s(0.01R_{\text{vir}})$ expressed in Eq. (12). The profile radii r are spaced logarithmically, with $N \sim 100$ radii r_i between $0.01R_{\text{vir}}$ and R_{vir} . The inner slope s_1 and the concentration parameter c_2 associated to the fit result can be derived from a and c with Eqs. (12) and (13). The rms

$$\sigma = \sqrt{\frac{1}{N} \sum_{i=1}^N (\log \rho_i - \log \rho_{\text{model}}(r_i))^2} \quad (42)$$

of the residuals between the simulated $\log \rho$ and the model is used to evaluate the relative goodness of fit in the range $0.01R_{\text{vir}} - R_{\text{vir}}$, and we also define σ_c the rms of the residuals in the central region of the halo between $0.01R_{\text{vir}}$ and $0.1R_{\text{vir}}$. The residuals themselves can be seen in Appendix H. The absolute value of σ (or σ_c) is sensitive to the smoothness of the simulated profile, in particular to the resolution of the simulations, the number of radii used, and the binning procedure for the profile. We thus mostly use it to compare the performance of different models in fitting a given target profile. We notably note that with profile radii spaced logarithmically, the effective weight assigned to the inner region of the halo is larger than it would have been with linearly-spaced radii.

Fig. 3 displays the DZ fit results to the DM density profile for eight fiducial $z = 0$ NIHAO haloes of different masses, simulated with baryons. This selection includes the two haloes studied more specifically in F20, g1.08e11 and g6.12e10, but is otherwise arbitrary in each mass range. The best-fit profile parameters a and c as well as the corresponding inner slope s_1 and concentration c_2 are indicated. The mass-dependence of the DM halo response to baryons described by Di Cintio et al. (2014a), Tollet et al. (2016), and Dutton et al. (2016b) is already visible in this figure, with the lowest-mass halo having a relatively steep cusp, haloes with stellar masses between 10^7 and $10^{10} M_\odot$ shallower cores, and the two most massive haloes steeper inner slopes.

The figure further compares the fits according to the DZ parametrization with fits according to the Einasto and the generalized NFW with free inner slope (gNFW) parametrizations. We recall that the Einasto density profile (Einasto 1965; Navarro et al.

2004, AZ13) can be expressed as

$$\rho_{\text{Einasto}}(r) = \rho_2 \exp\left(-\frac{2}{\nu} \left[\left(\frac{r}{r_2}\right)^\nu - 1\right]\right) \quad (43)$$

with r_2 the radius where the logarithmic density slope equals 2, ρ_2 the corresponding density and ν a shape parameter. The gNFW profile refers to Eq. (2) with $b = 1$ and $g = 3$ (e.g., AZ13), i.e.,

$$\rho_{\text{gNFW}}(r) = \frac{\rho_c}{x^a(1+x)^{3-a}} \quad (44)$$

with $x = r/r_c$ and a the innermost slope. These two profiles have two free shape parameters ($c_2 = R_{\text{vir}}/r_2$ and ν for the Einasto profile, a and $c = R_{\text{vir}}/r_c$ for the gNFW profile) as is the case for the DZ parametrization. As notably indicated by the rms σ and σ_c , Einasto fits are significantly worse for shallow inner density slopes than the other two, which seem to follow each other closely. This is particularly visible in the inner part of the density profile.

Fig. 4 compares the DM circular velocity profiles of the eight fiducial haloes of Fig. 3 with those resulting from the density profile fits. As for the density profile fits, we define σ_v and $\sigma_{v,c}$ the rms of the residuals between the simulated circular velocity V_c and the model, in the ranges $0.01R_{\text{vir}} - R_{\text{vir}}$ and $0.01R_{\text{vir}} - 0.1R_{\text{vir}}$, respectively. Although we note that there may be some $\lesssim 10\%$ offset in the velocity prescription at high masses, the DZ profile fares significantly better than the other two parametrizations in recovering the DM circular velocity profiles, as indicated by the systematically lower values of σ_v and $\sigma_{v,c}$. The inadequation of the Einasto and gNFW profiles is striking towards the innermost part of the rotation curve. Fig. 5 confirms the trends seen in Figs. 3 and 4 over the whole NIHAO sample at $z = 0$ by systematically comparing the rms σ , σ_c , σ_v , and $\sigma_{v,c}$ distributions of the three two-parameter models. We point out that the circular velocities at small radii obtained for the DZ, Einasto, and gNFW profiles are significantly impacted by the behavior of these profiles below the resolution limit of $0.01R_{\text{vir}}$.

3.2.2 Model versus simulated parameters

To quantify further the adequation of the different profile parametrizations, we define an inner slope s_1^* and a concentration

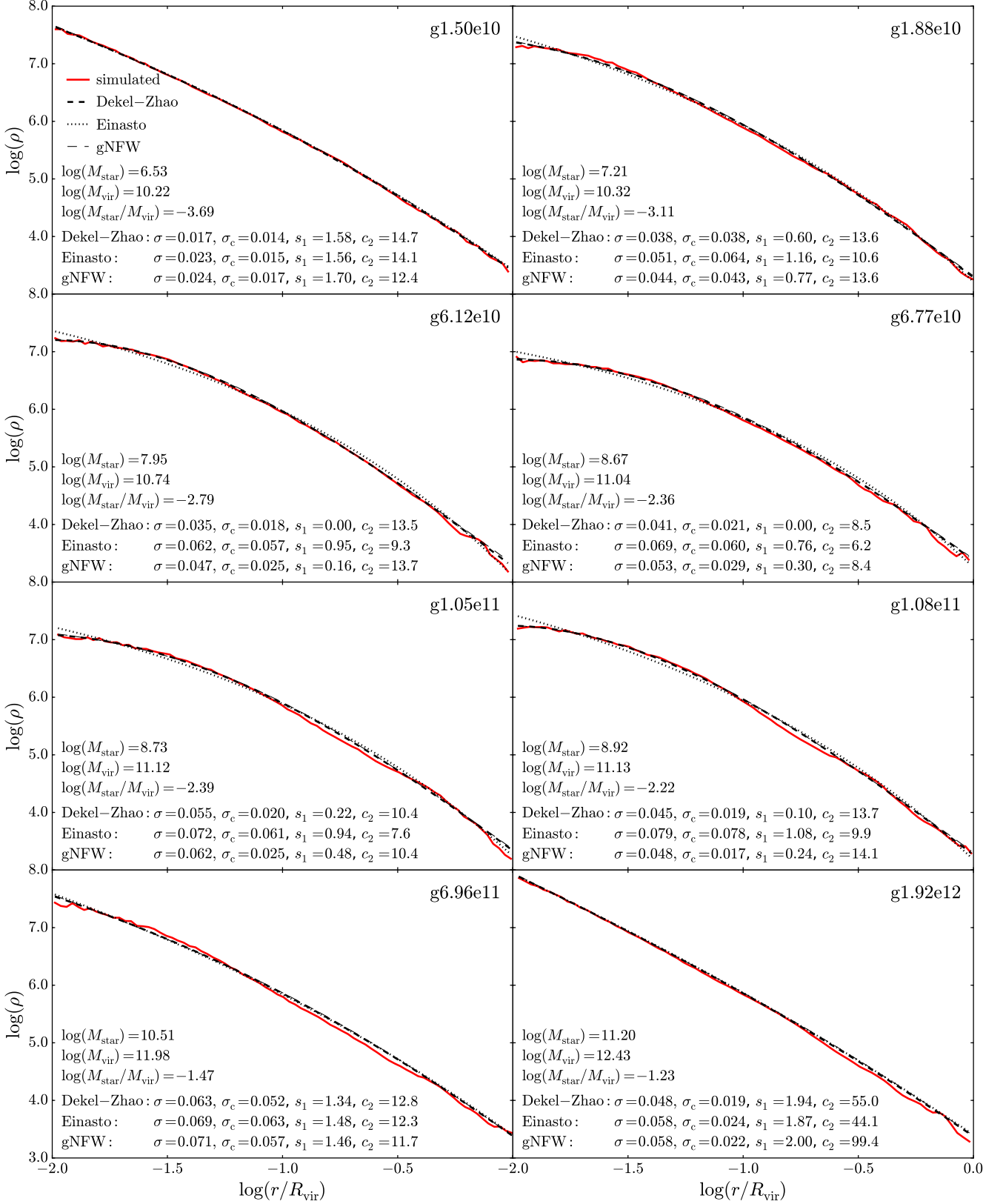


Figure 3. Model versus simulated density profiles: the dark matter density profiles at $z = 0$ of eight arbitrary NIHAO galaxies with baryons (plain red line) at different masses with their best-fitting DZ, Einasto and gNFW profiles (dashed, dotted, and thin dashed black lines, respectively), for radii covering the range between $0.01R_{\text{vir}}$ and R_{vir} . The rms errors σ and σ_c and the best-fit parameters s_1 and c_2 of the different parametrizations are indicated, as well as M_{star} , M_{vir} , and $M_{\text{star}}/M_{\text{vir}}$. The gNFW fits follow closely the DZ fits; the Einasto fits do not recover the inner density profiles as well as the others.

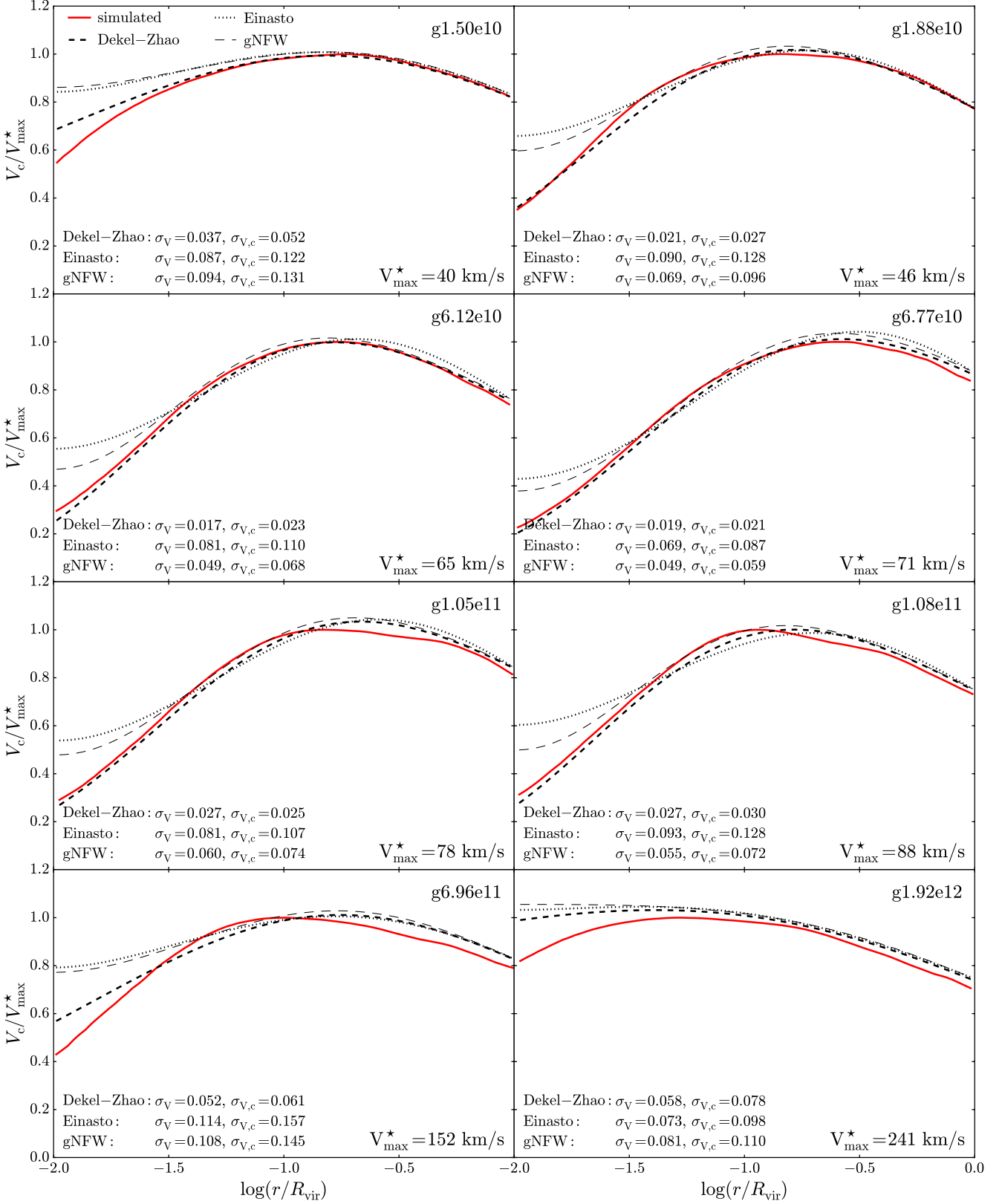


Figure 4. Model versus simulated rotation curves: dark matter circular velocity profiles, $V_c(r) = \sqrt{GM(r)/r}$, of the eight $z=0$ NIHAO galaxies shown in Fig. 3 (plain red line) together with those inferred from the DZ, Einasto and gNFW fits to their density profiles (dashed, dotted, and thin dashed black lines, respectively). The velocity of each galaxy is normalized to its maximum value V_{\max}^* , which is an increasing function of mass. The rotation curves inferred from the DZ fits to the density profiles recover better the simulated curves than those inferred from the Einasto and gNFW fits. The residuals of V_c/V_{\max}^* are shown in Appendix H.

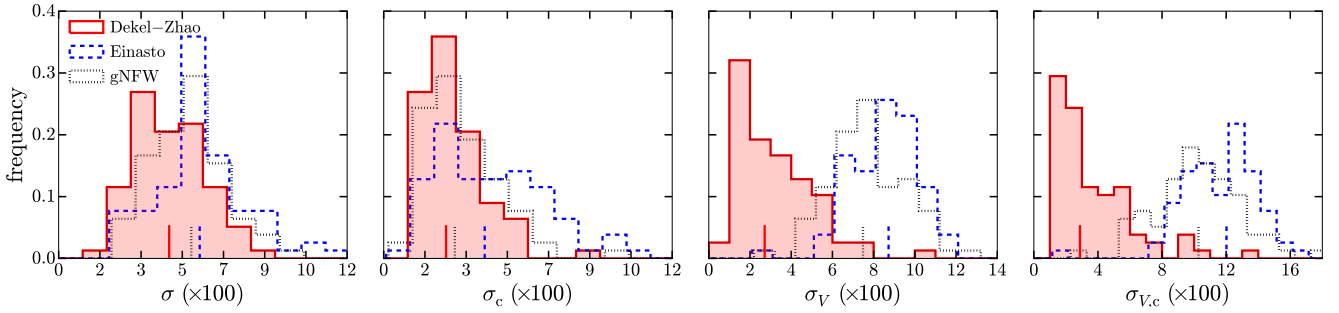


Figure 5. Comparing the model fits in terms of their rms errors: rms errors in $\log \rho$ and V_c/V_{\max} of the DZ (plain red line), Einasto (blue dashed line) and gNFW (black dotted line) fits over the ranges $0.01R_{\text{vir}} - R_{\text{vir}}$ and $0.01R_{\text{vir}} - 0.1R_{\text{vir}}$ for all NIHAO galaxies at $z = 0$. The median values for the three models, which are highlighted by vertical lines above the x-axis, respectively yield 0.046, 0.059, and 0.055 for σ , 0.026, 0.042, and 0.030 for σ_c , 0.027, 0.087, and 0.075 for σ_V , 0.029, 0.120, and 0.103 for $\sigma_{V,c}$. The standard deviations respectively yield 0.015, 0.019, and 0.015 for σ , 0.013, 0.023, and 0.015 for σ_c , 0.018, 0.016, and 0.018 for σ_V , 0.025, 0.023, and 0.026 for $\sigma_{V,c}$. The residuals from which the rms errors are computed are shown in Appendix H. The DZ profile provides better fits to the DM density profile than the Einasto and gNFW profiles, the difference being particularly striking in the resulting circular velocity profiles through σ_V and $\sigma_{V,c}$.

c_2^* directly measured from the simulated density and logarithmic slope profiles. The former is the average slope between $0.01R_{\text{vir}}$ and $0.02R_{\text{vir}}$, as notably used by Tollet et al. (2016); the latter corresponds to the radius where the logarithmic slope equals 2. Since the simulated slope profile can be relatively noisy, we smooth it using a Savitsky-Golay filter with maximum window size when measuring c_2^* . Fig. H1 in Appendix H illustrates how s_1^* and c_2^* are obtained from the simulated profiles. The definitions of these two quantities each have their own shortcomings, notably as s_1^* may in principle be different than the innermost slope at $0.01R_{\text{vir}}$ and as c_2^* may be affected by the smoothing, but do enable to capture reasonable inner slopes and concentrations. We use these quantities as references to describe the inner slope and concentration differences between model and simulation, $\Delta s = s_{1,\text{model}} - s_1^*$ and $\Delta c = c_{2,\text{model}} - c_2^*$.

Fig. 6 compares the inner slopes and concentrations derived from the DZ fits (s_1 and c_2) with those measured on the simulated profiles (s_1^* and c_2^*), highlighting very strong correlations (with Pearson correlation coefficients $r > 0.85$) with some scatter (0.26 for s_1 , 0.10 for $\log c_2$): the DZ fits enable to retrieve the inner slope and concentration measured from the simulated profiles. We further define V_{\max}^* and R_{\max}^* the maximum velocity and the corresponding radius on the simulated circular velocity profiles such as those shown in Fig. 4, as well as $\Delta V = (V_{\max,\text{model}} - V_{\max}^*)/V_{\max}^*$ and $\Delta R = (R_{\max,\text{model}} - R_{\max}^*)/R_{\max}^*$ the relative difference between the values derived from the density profile fits and those measured on the simulated profiles. Fig. 7 shows the distributions of Δs , Δc , ΔV , and ΔR for the DZ, Einasto, and gNFW fits for all NIHAO galaxies with baryons at $z = 0$. The figure shows that the DZ parametrization provides inner slopes closest to s_1^* on average while the other two, and in particular the Einasto parametrization, systematically overestimate the inner slope. This can already be seen in Fig. 3, where the Einasto fit is in most cases above the simulated density profile in the innermost part. The three parametrizations slightly tend to underestimate the concentration compared to that measured from the slope profile, but we recall that the latter may be affected by the smoothing. In this regard, the Einasto parametrization seems to yield a higher systematic offset than the other two, but the scatterers are similar. The three parametrizations recover the maximum velocity with a relative error $\lesssim 5\%$, but with a systematic overestimation of $\sim 1\%$ on average for DZ and Einasto, $\sim 3\%$ for gNFW. The maximum radius is less well recovered by all parametrizations, with relative errors spread around a 10% overestimate in the DZ

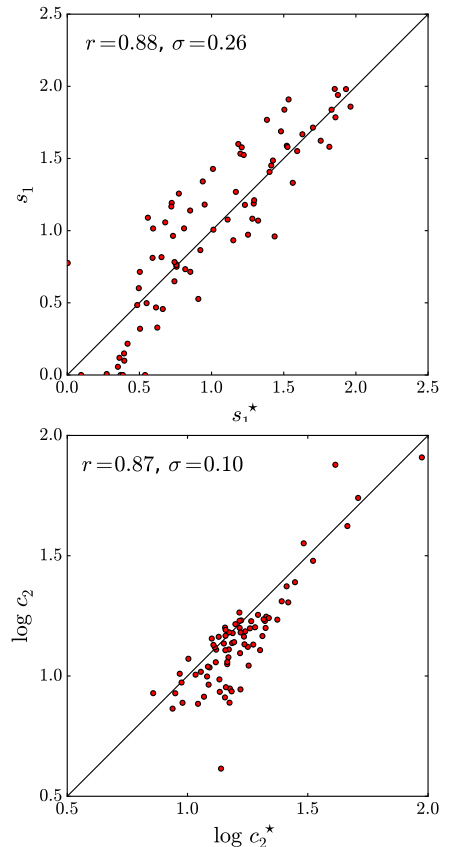


Figure 6. Model versus simulated parameters: comparison between the inner slope and concentration stemming from the DZ fits to the density profiles of the $z = 0$ NIHAO galaxies with baryons, s_1 and c_2 , and those obtained directly from the simulated profiles, s_1^* and c_2^* . The plain lines corresponds to a linear least-square fits. The Pearson correlation coefficient (r) and the residual scatter (σ) are indicated. The DZ fits enable to retrieve the inner slope and concentration measured from the simulated profiles.

case (6% for gNFW, 20% for Einasto) with a $\sim 30\%$ standard deviation.

We conclude from this analysis that the DZ parametrization provides significantly better fits to DM density profiles than Einasto and marginally better than gNFW, and infer better fits than both to

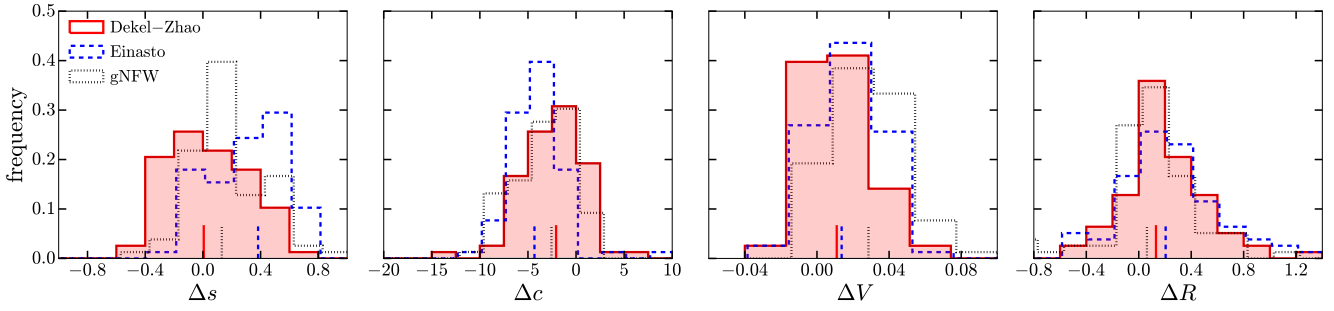


Figure 7. Comparing the model fit parameters: inner slope and concentration differences, $\Delta s = s_{1,\text{model}} - s_1^*$ and $\Delta c = c_{2,\text{model}} - c_2^*$, as well as the maximum velocity and radius relative differences, $\Delta V = (V_{\text{max,model}} - V_{\text{max}}^*)/V_{\text{max}}^*$ and $\Delta R = (R_{\text{max,model}} - R_{\text{max}}^*)/R_{\text{max}}^*$, between the DZ (plain red line), Einasto (blue dashed line) and gNFW (black dotted line) fits and the simulated profiles for all $z = 0$ NIHAO galaxies simulated with baryons. The median values for the three models, which are highlighted by vertical lines above the x-axis, respectively yield 0.01, 0.38, and 0.13 for Δs , -2.1 , -4.3 , and -2.6 for Δc , 0.011, 0.014, and 0.029 for ΔV , 0.13, 0.21, and 0.06 for ΔR . The standard deviations respectively yield 0.27, 0.27, and 0.25 for Δs , 5.1, 4.9, and 7.3 for Δc , 0.018, 0.018, and 0.020 for ΔV , 0.30, 0.35, and 0.34 for ΔR . The DZ profile provides better fits to the DM density profile than the Einasto and gNFW profiles, in particular with Δs , Δc , and ΔV generally closer to zero. We do note however that R_{max} is on average overestimated by $\sim 10\%$.

the circular velocity profile. It enables to recover the inner density slope s_1 with a ± 0.27 scatter but a negligible systematic error, the concentration c_2 with a ± 5 scatter and a limited -2 systematic offset on average (0.1 dex scatter and -0.05 dex offset in $\log c_2$). It retrieves the maximum velocity V_{max} with a $\pm 2\%$ scatter and a $+1\%$ systematic offset, the corresponding radius with a $\pm 30\%$ scatter and a $+13\%$ offset (0.11 dex scatter and $+0.05$ dex offset in $\log R_{\text{max}}$).

3.3 Mass-dependence of the profile parameters

3.3.1 Mass-dependence of s_1 and c_2

Fig. 8 shows the dependence of the inner slope s_1 and the concentration c_2 derived from the DZ density profile fits on the stellar mass M_{star} , the halo mass M_{vir} and the stellar-to-halo mass ratio $M_{\text{star}}/M_{\text{vir}}$. At low stellar mass, halo mass, and stellar-to-halo mass ratio, the halo is dominated by DM and hence follow the NFW slope ($s_1 \approx 1.25$) and concentration ($c_2 \approx 10$); at intermediate mass and stellar-to-halo mass ratio, stellar feedback is strong enough to overcome the gravitational potential and expand the halo; at high mass and stellar-to-halo mass ratio, there is adiabatic contraction of the halo due to the steepening of the gravitational potential. Halo expansion occurs for stellar masses between 10^7 to $10^{10} M_{\odot}$, halo masses between $10^{10.5}$ and $10^{11.5} M_{\odot}$, and stellar-to-halo mass ratios between $10^{-3.5}$ and 10^{-2} . As noted by Di Cintio et al. (2014a), the range in stellar-to-halo mass ratio where core formation occurs is in agreement with the analytic calculation of Peñarrubia et al. (2012) comparing the energy baryons must inject into a DM halo to remove its central cusp and the energy released by Type II supernovae explosions. We note that there is a hint of a small drop of the concentration c_2 in the range where core formation happens: feedback not only affect the inner part of the DM distribution, but also puffs-up the halo at larger scales. We recall that the NIHAO simulations used here do not include AGN feedback. As a consequence, the most massive haloes of the sample are partially overcooled, with $\log(M_{\text{star}}/M_{\text{vir}})$ close to -1 . When AGN feedback is included, the stellar mass of the most massive haloes is reduced, their dark matter distribution relaxes, and their inner slope slightly decreases (Blank et al. 2019; Macciò et al. 2020).

We try to capture the behaviour of the inner slope s_1 as a func-

tion of M_{star} , M_{vir} and $M_{\text{star}}/M_{\text{vir}}$ using the function

$$s_1(x) = \frac{s'}{1 + \left(\frac{x}{x_0}\right)^v} + s'' \log \left(1 + \left(\frac{x}{x_0}\right)^v \right) \quad (45)$$

where x_0 , s' , s'' , and v are adjustable parameters and $\log = \log_{10}$. We impose s' and s'' to be similar for the three variables x , which yields a unique asymptotical value $s' = 1.25$ when x goes to zero. This value corresponds approximately to an NFW cusp in the absence of baryons. Figure 8 further displays the fitting function obtained by Tollet et al. (2016) for the measured slope s_1^* between 1% and 2% of the virial radius R_{vir} in the same suite of cosmological zoom-in simulations with baryons. Motivated by Dutton & Macciò (2014) and Di Cintio et al. (2014b), we try to capture the behaviour of the concentration c_2 as a function of M_{star} , M_{vir} and $M_{\text{star}}/M_{\text{vir}}$ using the function

$$c_2(x) = c' \left(1 + \left(\frac{x}{x_0}\right)^v \right) \quad (46)$$

where x_0 , c' , and v are adjustable parameters. We impose c' to be similar for the three variables x , yielding $c' = 11.5$. This asymptotical value when x goes to zero is in accordance with fitting functions for the NFW concentration (e.g., Dutton & Macciò 2014). The values of the different fitting parameters are indicated in Table 1, together with the rms of the residuals (σ). This latter quantity is obtained through an iterative process excluding points beyond 3σ : this process does not affect the rms values of s_1 , which are equal to the standard deviation of the residuals, but does affect those of c_2 as it excludes some of the points at high mass or high mass ratio. The steep exponential rise of c_2 indeed leads to artificially high residuals when taking only y-axis errors into account, which is reflected in the standard deviation of the residuals. The value of σ obtained by the iterative process and indicated in the figure and the table corresponds to a very good approximation to the standard deviation inferred from the difference between the 16% and 84% quantiles of the residuals (which should be equal to 2σ).

Although the different panels highlight significant scatter, we note that the tightest relations are those as a function of the stellar-to-halo mass ratio: both the inner slope s_1 and the concentration c_2 react to the presence of baryons. The smaller scatter obtained for the stellar-to-halo mass ratio than for the stellar and halo masses is in agreement with the results of Di Cintio et al. (2014a) and Tollet et al. (2016), who show that the stellar-to-halo mass ratio (the

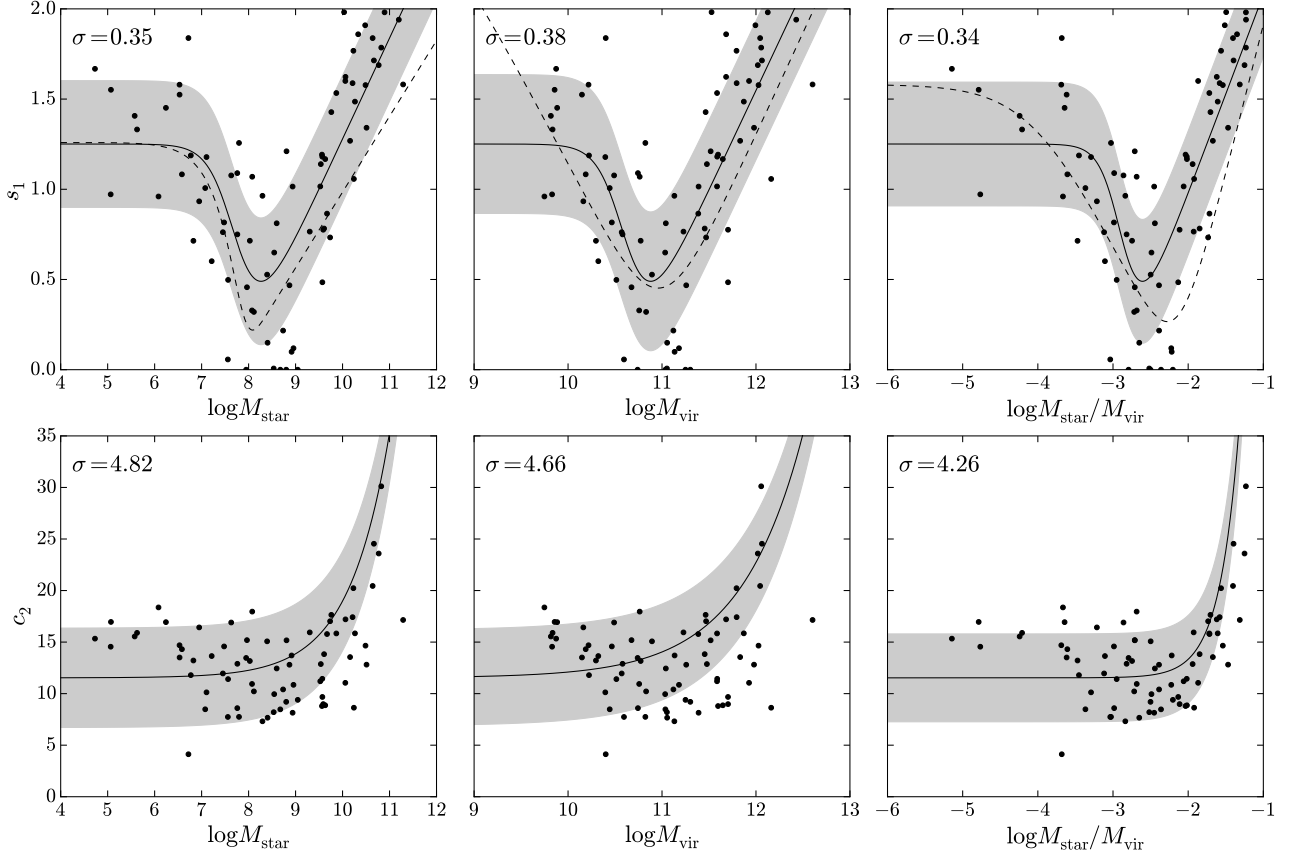


Figure 8. Mass-dependence of the DZ parameters: the inner slope s_1 and the concentration c_2 derived from the density profile fits as a function of stellar mass M_{star} , halo mass M_{vir} and stellar-to-halo mass ratio $M_{\text{star}}/M_{\text{vir}}$. The inner slope s_1 is fitted using the function proposed by Tollet et al. (2016) specified in Eq. (45); the best-fit curve is shown as the plain black line, while the Tollet et al. (2016) fit to s_1^* is shown as the dashed black line. The concentration c_2 is fitted using the function specified in Eq. (49). The values of the best-fitting parameters are indicated in Table 1. The rms σ of the residuals, which is highlighted in gray, is obtained through an iterative process excluding points beyond 3σ : this process does not affect the rms for s_1 but does affect that of c_2 as it excludes some of the points at high masses. The mass-dependence of s_1 is marked by the presence of cores for M_{star} between 10^7 and $10^{10} M_{\odot}$, M_{vir} between $10^{10.5}$ and $10^{11.5} M_{\odot}$, and $\log M_{\text{star}}/M_{\text{vir}}$ between -3.5 and -2 , adiabatic contraction above. The mass-dependence of c_2 also reflects adiabatic contraction at high masses. The tightest relations are those as a function of the stellar-to-halo mass ratio.

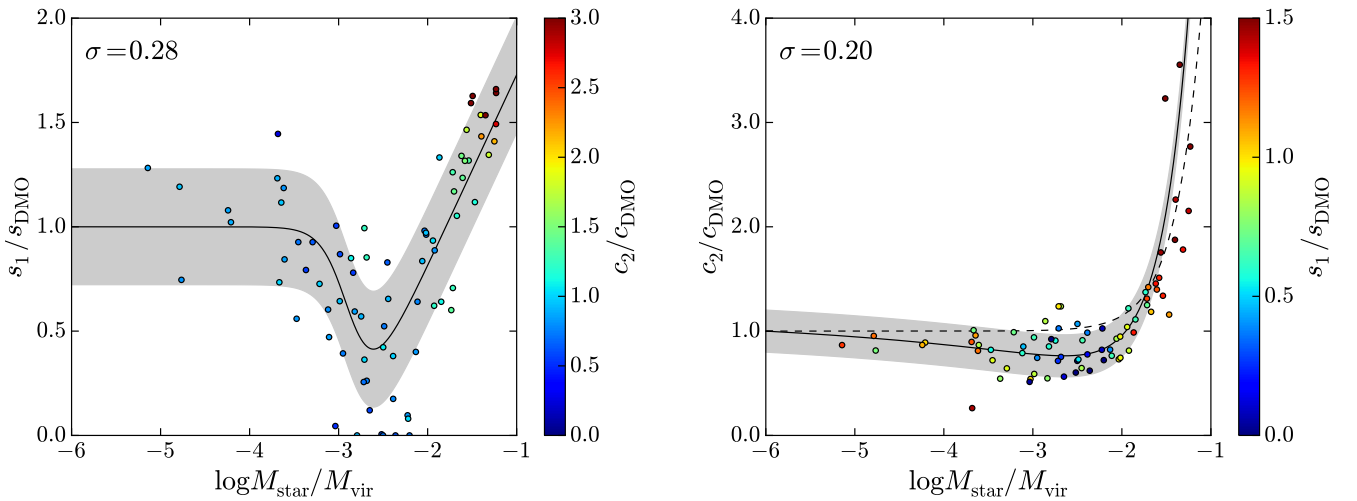


Figure 9. Mass-dependence of the DZ parameters at $z = 0$ with respect to those of dark-matter-only NFW profiles: the inner slope and concentration s_1 and c_2 derived from the DZ density profile fits divided by their expected values for NFW haloes of similar halo mass using the Dutton & Macciò (2014) relation (Eqs. 47 and 48), s_{DMO} and c_{DMO} , as a function of the stellar-to-halo mass ratio $M_{\text{star}}/M_{\text{vir}}$. The best-fit function following Eqs. (45) and (49), whose parameters are indicated in Table 1, are shown as plain black lines. The rms σ of the residuals, which is highlighted in gray, is obtained through an iterative process excluding points beyond 3σ as in Fig. 8. The best-fit function for c_2/c_{DMO} obtained by Di Cintio et al. (2014b), whose parameters following Eq. (46) are $c' = 1.0$, $c'' = 1.32 \times 10^2$, $\nu = 7.83$ (cf. their Eq. (6)), is indicated as a dashed black line. Colors in each panel correspond to the y-axis of the other panel. Core formation and halo expansion for $\log M_{\text{star}}/M_{\text{vir}}$ between -3.5 and -2 as well as adiabatic contraction are visible both in terms of s_1/s_{DMO} and c_2/c_{DMO} .

Table 1. Best-fitting parameters and relative errors for the slope and concentration relations shown in Figs. 8 and 9. The fitting functions are specified in Eqs. (45), (46), and (49). We impose s' , s'' , and c' to be the same as a function of the three variables M_{star} , M_{vir} , and $M_{\text{star}}/M_{\text{vir}}$ for s_1 and c_2 . The rms σ of the residuals within 3σ is also indicated.

Relation	x_0	s'	s''	ν	σ
$s_1(M_{\text{star}})$	$5.18 \cdot 10^7$	1.25	0.37	1.51	0.35
$s_1(M_{\text{vir}})$	$3.99 \cdot 10^{10}$	1.25	0.37	3.00	0.38
$s_1\left(\frac{M_{\text{star}}}{M_{\text{vir}}}\right)$	$1.30 \cdot 10^{-3}$	1.25	0.37	2.98	0.34
$\left(\frac{s_1}{s_{\text{DMO}}}\right)\left(\frac{M_{\text{star}}}{M_{\text{vir}}}\right)$	$1.30 \cdot 10^{-3}$	1	0.32	2.86	0.28
Relation	x_0	c'	ν	μ	σ
$c_2(M_{\text{star}})$	$2.38 \cdot 10^{10}$	11.5	0.50	-	4.82
$c_2(M_{\text{vir}})$	$1.05 \cdot 10^{12}$	11.5	0.65	-	4.66
$c_2\left(\frac{M_{\text{star}}}{M_{\text{vir}}}\right)$	$3.04 \cdot 10^{-2}$	11.5	1.67	-	4.26
$\left(\frac{c_2}{c_{\text{DMO}}}\right)\left(\frac{M_{\text{star}}}{M_{\text{vir}}}\right)$	$2.43 \cdot 10^{-2}$	1.14	1.37	0.142	0.20

‘integrated star formation efficiency’) is the best parameter to capture the effect of baryons on the DM distribution. This was also suggested by hydrodynamical simulations of dwarf galaxies (e.g., Mashchenko et al. 2008; Madau et al. 2014; Verbeke et al. 2015; Read et al. 2016), which showed that core formation occurs above a critical mass depending on the halo mass.

3.3.2 Comparison with the dark-matter-only parameters

To isolate the effect of the introduction of baryonic processes on the inner slope s_1 and the concentration c_2 , we normalize these two quantities by their expected NFW values in dark-matter-only simulations, s_{DMO} and c_{DMO} . Namely, we use the best-fitting relation for the NFW concentration as a function of halo mass (measured using Bryan & Norman 1998) from Dutton & Macciò (2014),

$$\log c_{\text{DMO}} = 1.025 - 0.097 \log \left(\frac{h M_{\text{vir}}}{10^{12} M_{\odot}} \right) \quad (47)$$

with $h = 0.671$ the dimensionless Hubble parameter (Planck Collaboration et al. 2014), the corresponding NFW slope at $0.01 R_{\text{vir}}$ being

$$s_{\text{DMO}} = \frac{1 + 0.03 c_{\text{DMO}}}{1 + 0.01 c_{\text{DMO}}}. \quad (48)$$

Fig. 9 shows the slope and concentration ratios s_1/s_{DMO} and c_2/c_{DMO} as a function of the stellar-to-halo mass ratio $M_{\text{star}}/M_{\text{vir}}$, which is the variable leading to the lowest scatter in Fig. 8. Fig. 9 highlights the formation of shallow cores for $\log M_{\text{star}}/M_{\text{vir}}$ between -3.5 and -2 and adiabatic contraction above. Both effects are visible not only in terms of s_1/s_{DMO} , but also in terms of c_2/c_{DMO} : while the slope ratio decreases from 1 to below 0.5 before increasing above 1.5 as $M_{\text{star}}/M_{\text{vir}}$ increases, the concentration ratio decreases to ~ 0.8 before sharply rising up to ~ 3 . This drop in halo concentration for $\log(M_{\text{star}}/M_{\text{vir}})$ between -3.5 and -2 had not been seen previously, as highlighted by the dashed line obtained by Di Cintio et al. (2014b), but was also recently reported by Lazar et al. (2020) using the FIRE-2 simulations.

We fit the slope ratio s_1/s_{DMO} as a function of $M_{\text{star}}/M_{\text{vir}}$ with the function of Eq. (45) and $s' = 1$ to impose an NFW slope when $M_{\text{star}}/M_{\text{vir}}$ goes to zero. The concentration ratio is fitted as a function of $M_{\text{star}}/M_{\text{vir}}$ with the function of Eq. (49) plus a second power-law term to account for the dip of concentration when $\log M_{\text{star}}/M_{\text{vir}}$

is between -3.5 and -2, namely

$$\left(\frac{c_2}{c_{\text{DMO}}} \right) (x) = c' \left(1 + \left(\frac{x}{x_0} \right)^{\nu} \right) - x^{\mu} \quad (49)$$

with x_0 , c' , ν , and μ four adjustable parameters constrained to yield $c_2/c_{\text{DMO}} = 1$ at $\log M_{\text{star}}/M_{\text{vir}} = -6$. Table 1 lists the best-fit parameters of the functions describing the slope and concentration ratios and the rms of the residuals, which indicates the scatter of the two relations. A large part of this scatter has a physical origin related to the individual merger and star formation histories of the simulated galaxies. In particular, we note that the scatter in stellar mass at fixed halo mass is estimated to be between 0.16-0.2 dex at $z = 0$ (e.g., More et al. 2009; Reddick et al. 2013; Behroozi et al. 2013). The processes responsible for this scatter, such as mergers, star formation, and feedback, are expected to affect DM haloes as well (cf. introduction) and hence the inner slope and the concentration parameter associated to the DZ fits. We further note from the colorscale on both panels that the inner slope and concentration ratios s_1/s_{DMO} and c_2/c_{DMO} are correlated.

4 A MASS-DEPENDENT PROFILE

4.1 Prescriptions

Section 3.3 establishes the DZ profile as a mass-dependent profile, whose shape parameters s_1 and c_2 (or equivalently, a and c) are set by the stellar-to-halo mass ratio $M_{\text{star}}/M_{\text{vir}}$. It further provides fitting functions for the dependences of s_1 and c_2 on $M_{\text{star}}/M_{\text{vir}}$. As for the Di Cintio+ profile, it is thus possible to derive the shape of the DM distribution taking into account the effect of baryons for any halo given its stellar or halo mass. While the Di Cintio+ profile uses four shape parameters including the concentration, the DZ profile describes the DM distribution with only two parameters, with the advantage to have analytic expressions for the gravitational potential and the velocity dispersion (cf. Z96, D17), the resulting kinetic energy (cf. F20), and lensing properties (cf. Section 2). Inspired by the Appendix of Di Cintio et al. (2014b), we provide here prescriptions to derive the DZ DM profile associated to any given halo.

(i) The inputs are the halo mass M_{vir} and the stellar mass M_{star} . If only one of the two quantities is known, one can use an abundance matching $M_{\text{star}}/M_{\text{vir}}$ relation to derive the other one (e.g. Moster et al. 2013; Behroozi et al. 2013, 2019; Rodríguez-Puebla et al. 2017).

(ii) Determine the virial radius R_{vir} using the overdensity criterion

$$M_{\text{vir}} = \frac{4\pi}{3} R_{\text{vir}}^3 \Delta \rho_{\text{crit}} \quad (50)$$

with $\Delta = 18\pi^2 + 82x - 39x^2$ at $z = 0$ for $x = \Omega_m - 1$ from Bryan & Norman (1998) and $\rho_{\text{crit}} = 3H^2/8\pi G$ the critical density of the Universe. With the Planck Collaboration et al. (2014) parameters, $\Delta = 103.5$ and $\rho_{\text{crit}} = 124.9 M_{\odot} \text{kpc}^{-3}$.

(iii) Compute the inner slope and concentration ratios s_1/s_{DMO} and c_2/c_{DMO} from the stellar-to-halo mass ratio $M_{\text{star}}/M_{\text{vir}}$ using the fitting functions from Eqs. (45) and (49), whose best-fit parameters are indicated in Table 1. These functions were obtained in the range $-5 \leq \log(M_{\text{star}}/M_{\text{vir}}) \leq -1$ and converge to 1 for smaller values of $\log(M_{\text{star}}/M_{\text{vir}})$.

(iv) Obtain the slope s_1 and the concentration c_2 from the corresponding ratio using the typical concentration c_{DMO} of a DM-only NFW halo from Dutton & Macciò (2014), recalled in Eq. (47),

and the corresponding inner slope at $0.01R_{\text{vir}}$, s_{DMO} , expressed in Eq. (48).

(v) Convert s_1 and c_2 into the DZ parameters a and c using Eqs. (14) and (15). We recall that these latter parameters are not as physically meaningful as s_1 and c_2 .

(vi) Obtain the scale radius r_c and the characteristic density ρ_c entering the expression of the density, $r_c = R_{\text{vir}}/c$ and $\rho_c = (1 - a/3)c^3\mu\bar{\rho}_{\text{vir}}$, with $\mu = c^{a-3}(1 + c^{1/2})^{2(3-a)}$ and $\bar{\rho}_{\text{vir}} = 3M_{\text{vir}}/4\pi R_{\text{vir}}^3 = \Delta\rho_{\text{crit}}$.

(vii) Determine the mass-dependent density profile using Eq. (11); the corresponding circular velocity profile using Eqs. (4) and (6), with $\rho_c = c^3\mu\bar{\rho}_{\text{vir}}$, $b = 2$, and $\bar{g} = 3$. The gravitational potential profile is obtained from Eq. (19), the velocity dispersion profile from Eq. (22), the projected surface density profile from Eq. (32) or its series expansion (Eq. F5), the scaled deflexion angle from Eq. (38) or its series expansion (deduced from Eq. (F6)), the lensing shear from the average projected surface density of Eq. (41) or its series expansion (Eq. (F10)). Table 2 below summarizes the different analytic expressions available for the DZ profile.

In the following section, we show that these prescriptions for the DZ profile are in relatively good agreement with simulated density and circular velocity profiles and fare as good as the *Di Cintio+* prescriptions given the stellar and halo masses. When fitting rotation curves of galaxies, we however advocate to release the mass-dependent prescription for the concentration c_2 and to leave this parameter free (as advocated for the *Di Cintio+* profile by *Di Cintio et al. 2014b*). This enables to obtain extremely good fits to simulated density and circular velocity profiles (cf. Section 4.3).

4.2 Accuracy of the mass-dependent prescriptions

Fig. 10 compares the inner logarithmic slope and the concentration stemming from the mass-dependent prescriptions of Section 4.1 with s_1^* and c_2^* determined directly from the simulated profiles (cf. Section 3.2). Although the Pearson correlation coefficients are slightly lower than those of Fig. 6, the inner slope and concentration are well recovered. Overall, these mass-dependent prescriptions enable to retrieve the inner slope s_1 with a ± 0.31 scatter and a negligible systematic error and the concentration c_2 with a ± 9 scatter and a small -1.5 systematic offset (0.12 dex scatter and -0.05 dex offset in $\log c_2$). As further shown in Figs. G3 and G4, these prescriptions retrieve the maximum velocity V_{max} with a $\pm 9\%$ scatter and a $+3\%$ offset, and the corresponding radius R_{max} with a $\pm 31\%$ scatter and a $+12\%$ offset (0.14 dex scatter and $+0.05$ dex offset in $\log R_{\text{max}}$). The scatters and offsets in Δs , Δc , ΔV , and ΔR are comparable to those described for the fits in Section 3.2 but the rms errors and the discrepancies between prescribed and simulated profiles are significantly higher (σ progressing on average from 0.046 to 0.080, σ_V from 0.027 to 0.072, and similar trends for σ_{center} and $\sigma_{V,\text{center}}$), especially at high stellar-to-halo mass ratio: while the overall scatters and offsets are preserved, discrepancies arise on a case by case basis. The difference between the parametrized and the simulated rotation curves can be as high as 20%. As discussed in the following section, releasing the constraint on the concentration when fitting rotation curves enables to significantly improve the fits.

In Appendix G, we further compare the current mass-dependent prescriptions with those of *Di Cintio et al. (2014b)*. For this other mass-dependent profile, the four shape parameters entering Eq. (2) – namely a , b , g , and the concentration parameter associated to the scale radius r_c – are expressed as a function of the stellar-to-halo mass ratio while the scale density ρ_c is deduced from the halo mass, since the enclosed mass associated to the profile must

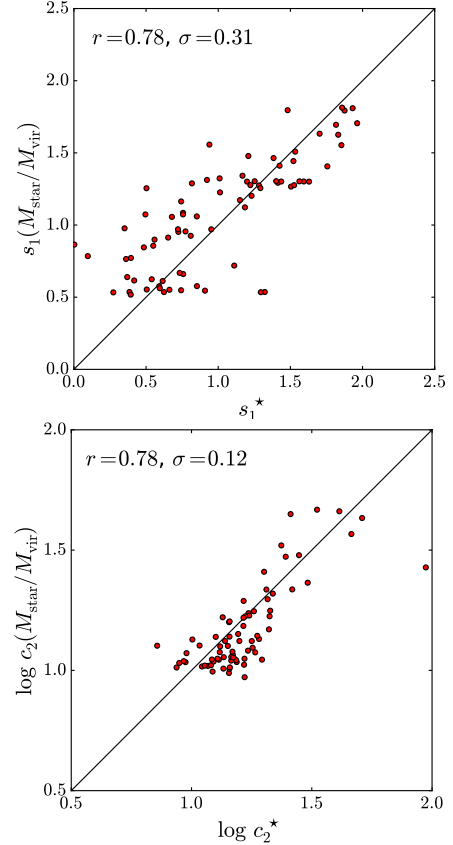


Figure 10. Prescribed versus simulated parameters: comparison between the inner slope and concentration stemming from the mass-dependent prescriptions for the $z = 0$ NIHAO galaxies with baryons, and those obtained directly from the simulated profiles, s_1^* and c_2^* . The plain lines corresponds to a linear least-square fits. The Pearson correlation coefficient and the residual scatter are indicated. The prescriptions enable to retrieve the inner slope and concentration.

verify $M(R_{\text{vir}}) = M_{\text{vir}}$. Both for the current and *Di Cintio+* prescriptions, all the parameters describing the profiles are set given the stellar and halo masses. Appendix G shows that the prescriptions of Section 4.1 provide equally good (or even marginally better) fits to the simulated density and velocity profiles than the *Di Cintio+* prescriptions. We caution however that while the current prescriptions stem from the NIHAO sample itself, the *Di Cintio+* prescriptions were obtained from a smaller sample of 10 simulated galaxies (the MaGICC sample; *Brook et al. 2012*; *Stinson et al. 2013*), such that the slightly better accuracy of the current prescriptions is most likely due to the different nature and size of the simulations used. We thus prefer to conclude that the accuracy of the two prescriptions are comparable. An update of the *Di Cintio+* prescriptions with the NIHAO simulations would indeed slightly increase their accuracy within the current sample, but is left for future work – especially as it would only lead to small differences and as the *Di Cintio+* prescriptions are widely used as they are.

4.3 Modelling rotation curves

To fit circular velocity profiles, *Di Cintio et al. (2014b)* use their prescriptions for the three shape parameters a , b , g describing the density profile (cf. Eq. (2)) but leave the scale radius r_c and the scale density ρ_c as free parameters. The right panel of Fig. 9 showing the concentration ratio c_2/c_{DMO} as a function of the stellar-to-halo mass

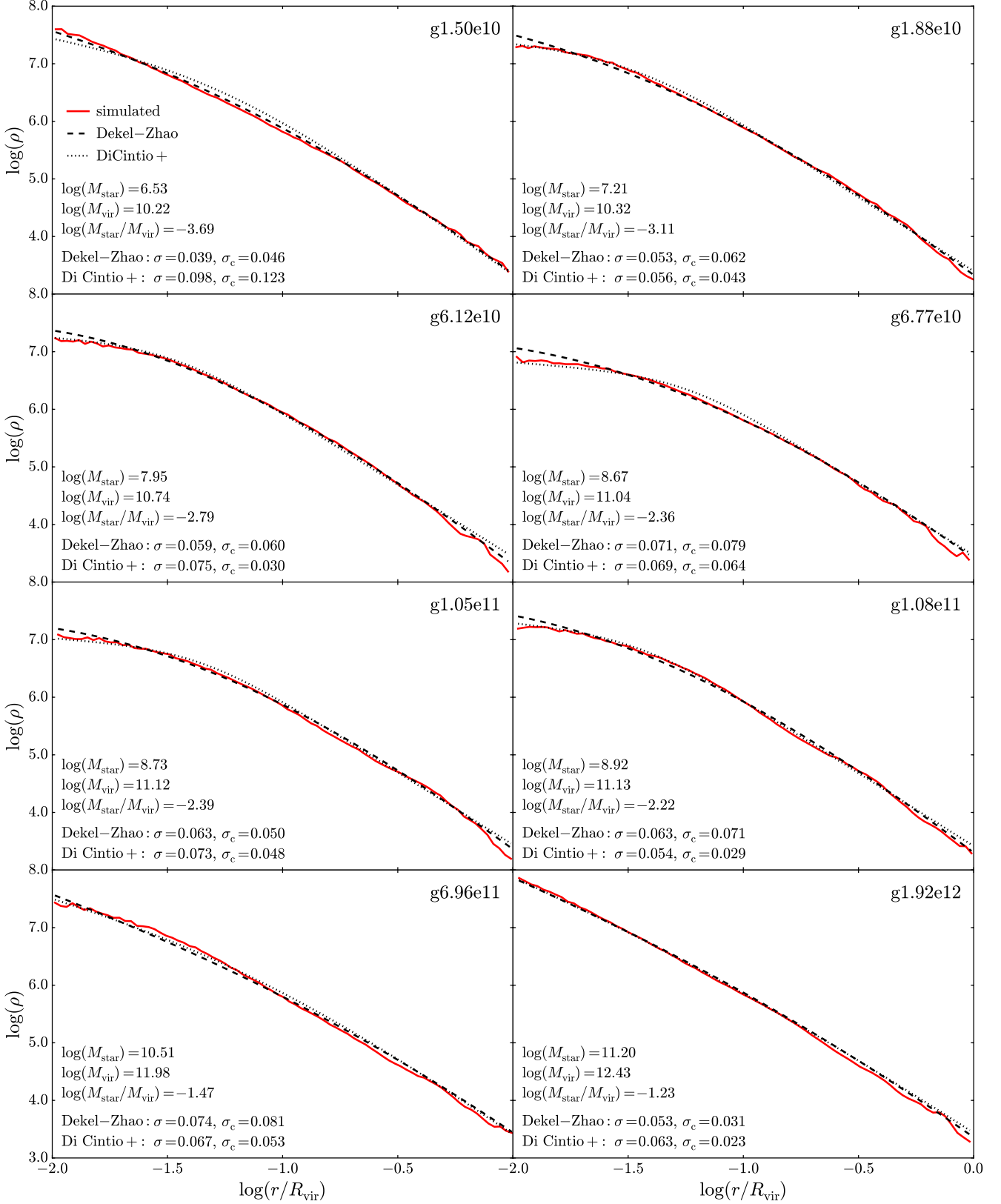


Figure 11. Prescribed versus simulated density profiles when fitting rotation curves (leaving the concentration free): the dark matter density profiles at $z = 0$ of the 8 arbitrary NIHAO galaxies shown in Fig. 3 (plain red line) with their DZ (dashed) and DiCintio+ (dotted) one-parameter fit to the rotation curves. For the DZ profile, the inner slope s_1 is set by the fitting function of Fig. 9 (cf. Eq. (45) and Table 1) but the concentration c_2 is allowed to vary; for the DiCintio+ profile, the shape parameters a , b , g of Eq. (2) are set by their mass-dependent prescriptions (DiCintio et al. 2014b, Eq. (3)), the scale radius r_c is allowed to vary, and the characteristic density ρ_c is constrained by the halo mass M_{vir} . The masses M_{star} , M_{vir} , $M_{\text{star}}/M_{\text{vir}}$ and the rms errors σ and σ_{center} are indicated. Both the DZ and the DiCintio+ parametrizations provide extremely good fits to the density profiles.

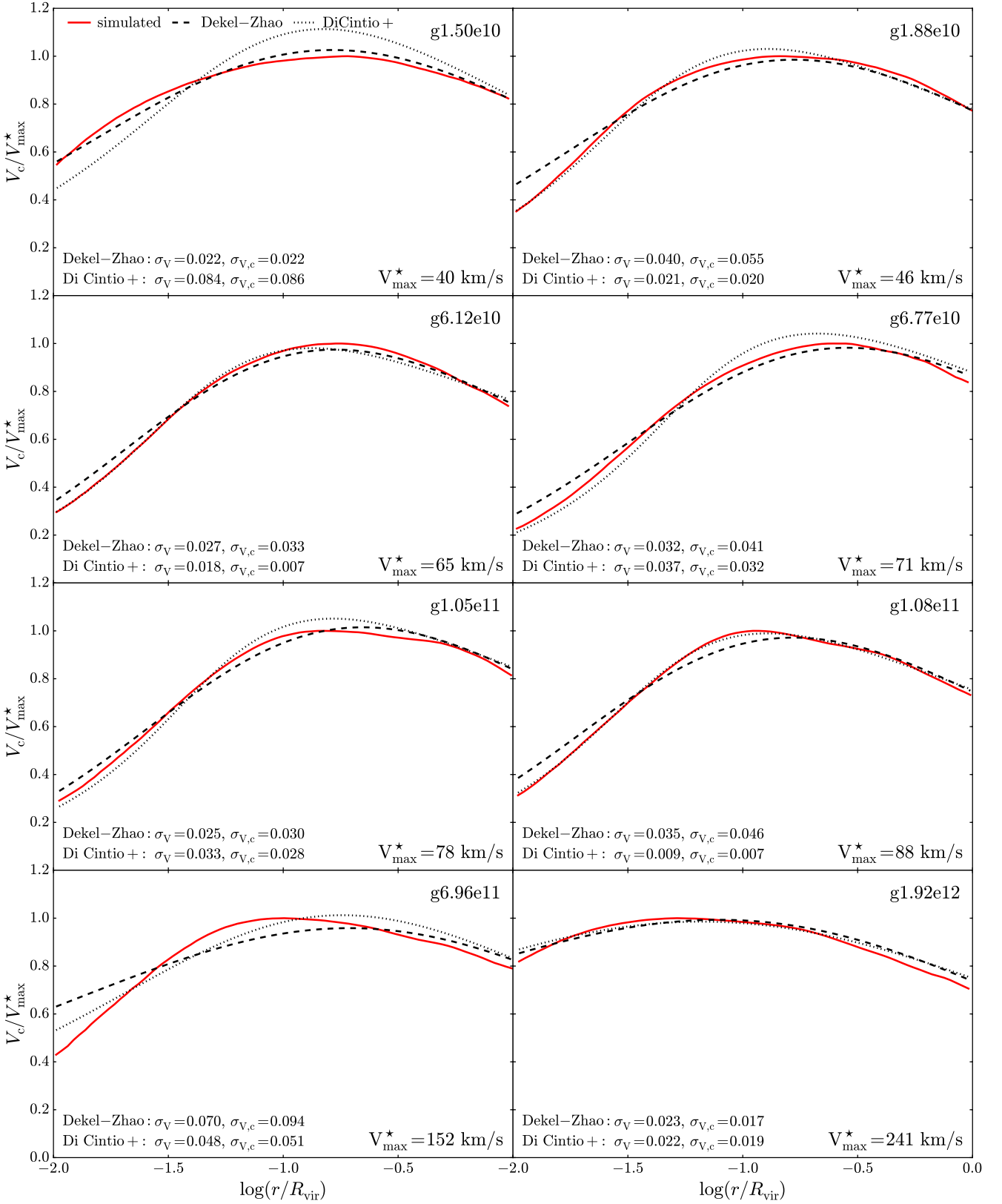


Figure 12. Prescribed versus simulated rotation curves when leaving the concentration free: dark matter circular velocity profiles, $V_c(r) = \sqrt{GM(r)/r}$, of the eight $z = 0$ NIHAO galaxies shown in Fig. 3 (plain red line) together with those inferred from the DZ and Di Cintio+ one-parameter fit to the rotation curves (dashed and dotted lines, respectively). For the DZ profile, the inner slope s_1 is set by the fitting function of Fig. 9 (cf. Eq. (45) and Table 1) but the concentration c_2 is allowed to vary; for the Di Cintio+ profile, the shape parameters a , b , g of Eq. (2) are set by their mass-dependent prescriptions (Di Cintio et al. 2014b, Eq. (3)), the scale radius r_c is allowed to vary, and the characteristic density ρ_c is constrained by the halo mass M_{vir} . The velocity of each galaxy is normalized to its maximum value V_{\max}^* , which is an increasing function of mass. Both the DZ and the Di Cintio+ parametrizations provide extremely good fits to the rotation curves, with differences below 10% that are well within observational errors.

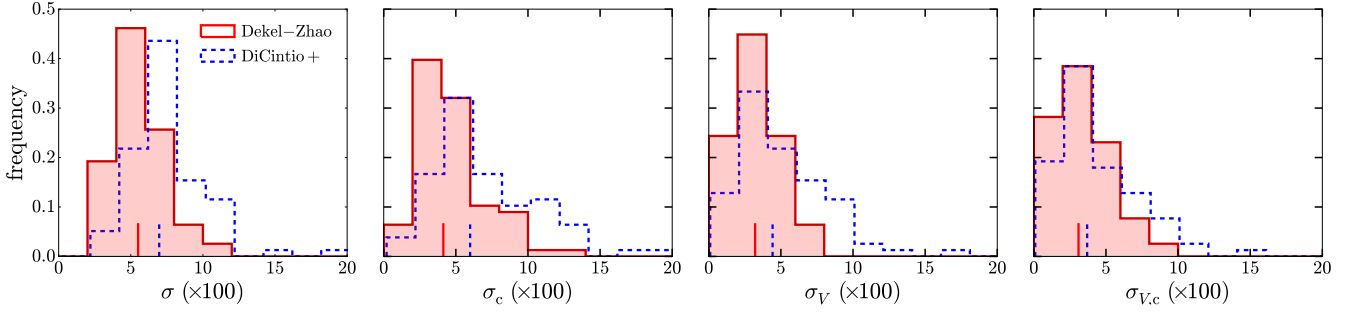


Figure 13. Comparing the current DZ and *Di Cintio+* rotation curve fits in terms of their rms errors: rms errors in $\log \rho$ and V_c/V_{\max} of the current (plain red line) and *Di Cintio+* (blue dashed line) one-parameter fit to the rotation curves over the ranges $0.01R_{\text{vir}} - R_{\text{vir}}$ and $0.01R_{\text{vir}} - 0.1R_{\text{vir}}$ for all NIHAO galaxies at $z = 0$. The median values for the two prescriptions, which are highlighted by vertical lines above the x-axis, respectively yield 0.055 & 0.070 for σ , 0.041 & 0.060 for σ_{center} , 0.032 & 0.044 for σ_V , 0.031 & 0.037 for $\sigma_{V,\text{center}}$. The standard deviations respectively yield 0.017 & 0.026 for σ , 0.022 & 0.035 for σ_{center} , 0.015 & 0.030 for σ_V , 0.019 & 0.027 for $\sigma_{V,\text{center}}$. The DZ profile provides marginally better fits than the *Di Cintio+* profile.

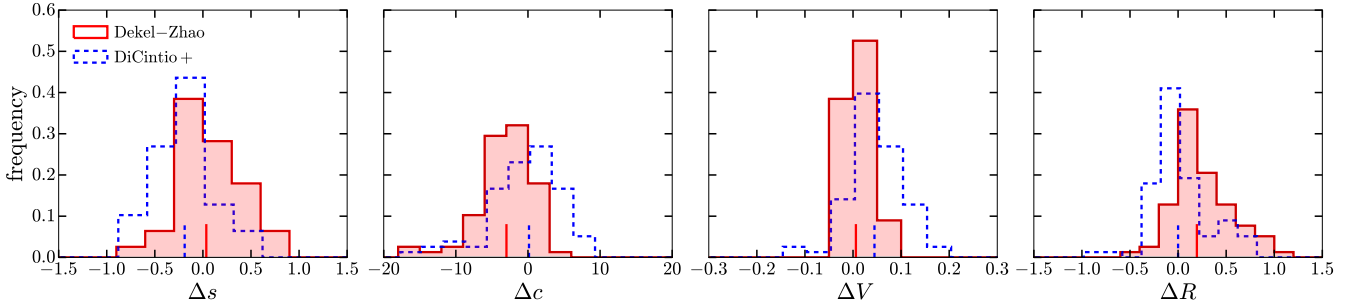


Figure 14. Comparing the current DZ and *Di Cintio+* rotation curve fit parameters: inner slope and concentration differences, $\Delta s = s_{1,\text{model}} - s_1^*$ and $\Delta c = c_{2,\text{model}} - c_2^*$, as well as the maximum velocity and radius relative differences, $\Delta V = (V_{\text{max,model}} - V_{\text{max}}^*)/V_{\text{max}}^*$ and $\Delta R = (R_{\text{max,model}} - R_{\text{max}}^*)/R_{\text{max}}^*$, between the DZ (plain red line) and the *Di Cintio+* (blue dashed line) one-parameter fit to the rotation curves and the simulated profiles for all $z = 0$ NIHAO galaxies simulated with baryons. The median values for the two prescriptions, which are highlighted by vertical lines above the x-axis, respectively yield 0.04 & -0.19 for Δs , -3.0 & 0.1 for Δc , 0.01 & 0.05 for ΔV , 0.20 & 0.00 for ΔR . The standard deviations respectively yield 0.31 & 0.29 for Δs , 8.6 & 9.0 for Δc , 0.03 & 0.06 for ΔV , 0.30 & 0.30 for ΔR . The mass-dependent prescription for the inner logarithmic slope s_1 enables extremely good fits to rotation curves of simulated galaxies when the concentration c_2 is allowed to vary.

ratio $M_{\text{star}}/M_{\text{vir}}$ (as well as Figs. G1 and G2) highlights the difficulty to account for the scatter in concentration at high stellar-to-halo mass ratio, which leads to significant discrepancies in the density and velocity profiles derived from the current mass-dependent prescriptions in the domain where c_2/c_{DMO} increases exponentially. This motivates to release the mass constraint on the concentration c_2 when modelling rotation curves of galaxies with the DZ profile, thus treating it as a two-parameter profile (the two parameters being M_{vir} and c_2 given the stellar mass M_{star}). This is similar to what is advocated for the *Di Cintio+* profile. When applied to simulated haloes whose mass M_{vir} is known, enforcing $M(R_{\text{vir}}) = M_{\text{vir}}$ effectively leaves one free parameter (r_c or its associated concentration).

Figs. 11 and 12 show the density and circular velocity profiles resulting from one-parameter fits to the rotation curves using the DZ profile and its current mass-dependent prescription for the inner logarithmic slope s_1 for the eight fiducial NIHAO haloes shown in Figs. 3, together with the corresponding *Di Cintio+* one-parameter fits and the simulated profiles. The inner slope s_1 of the DZ profile is set by the fitting function of Fig. 9 (cf. Eq. (45) and Table 1) given the stellar and halo masses while its concentration c_2 is allowed to vary. The shape parameters a , b , g of the *Di Cintio+* profile (Eq. (2)) are set by their mass-dependent prescriptions (*Di Cintio et al. 2014b*, Eq. (3)), while the scale radius r_c is allowed to vary. The *Di Cintio+* characteristic density ρ_c is constrained by the halo mass M_{vir} . Fig. 13 further shows the distributions of the rms of the residuals in density and velocity between model and simulation

within the whole NIHAO sample, while Fig. 14 shows the corresponding distributions of Δs , Δc , ΔV , and ΔR . Both the DZ and the *Di Cintio+* profiles provide extremely good fits to the density and circular velocity profiles, with rms values comparable to those obtained from the two-parameter fits of Section 3.2 and much smaller than those obtained in Section 4.2. The one-parameter DZ fits to the rotation curves enable to retrieve the inner slope s_1 with a ± 0.3 scatter and a negligible systematic error (as in the previous Section 4.2, since s_1 is set by its mass-dependent prescription), the concentration c_2 with a ± 8.6 scatter and a small -3.0 systematic offset (0.1 dex scatter and -0.08 dex offset in $\log c_2$), the maximum velocity V_{max} with a 3% scatter and a $+0.6\%$ offset, and the corresponding radius R_{max} with a $\pm 30\%$ scatter and a $+20\%$ offset (0.11 dex scatter and $+0.08$ dex offset in $\log R_{\text{max}}$). These scatters and offsets are comparable to those obtained previously, except for ΔV where they are significantly smaller. The differences between the parametrized and the simulated rotation curves are below 10% at any radius and for any galaxy, i.e., well within observational errors. In contrast, the NFW profile used for DM haloes is in contrast unable to describe such rotation curves in the presence of baryons, with differences as high as 50% in the intermediate mass range where core formation occurs (*Di Cintio et al. 2014b*).

5 CONCLUSION

Baryonic processes affect the dark matter haloes in which galaxies are embedded, their inner density profiles ranging from steep NFW-like cusps as in DM-only simulations (Navarro et al. 1996, 1997) at low stellar masses, flat cores in the stellar mass range between 10^7 and $10^9 M_\odot$, and cusps steeper than NFW at higher stellar masses (e.g., Di Cintio et al. 2014b; Tollet et al. 2016; Dutton et al. 2016b). In the present article, we study a parametrisation of DM haloes that enables to describe this variety of halo responses to baryonic processes with a variable inner logarithmic slope s_1 and a variable concentration parameter c_2 . This parametrization, which we refer to here as the Dekel-Zhao (DZ) profile, is a specific case of the Zhao family of double power-law models (Eq. (2), Z96) in which the outer logarithmic slope is set to $g = 3.5$ and the exponent describing the transition between the inner and outer regions to $b = 2$. As shown by Z96 and AZ13, it allows analytic expressions for the gravitational potential and the velocity dispersion, which we recall in Section 2.2.2 (Eqs. (19) and (22)). Using three pairs of haloes at different masses with and without baryons at $z = 0$, taken from the NIHAO suite of hydrodynamical cosmological zoom-in simulations (Wang et al. 2015), D17 show that this parametrization yields excellent fits to the density and circular velocity profiles of DM haloes ranging from steep cusps to flat cores, notably capturing cores better than the NFW and Einasto (1965) profiles. In F20, we further derive the kinetic energy associated to this DZ profile and show that it fits well with the simulated quantity.

In the present article, we extend the work done by Z96, AZ13, D17 and F20 by gathering most analytic expressions obtained for the DZ profile (Sections 2.1 and 2.2), by deriving additional analytic expressions for its lensing properties in terms of Fox H functions (Section 2.3) and by testing this profile over the whole NIHAO suite of simulations at $z = 0$ (Section 3). We also provide analytic expressions in terms of the maximum circular velocity and radius V_{\max} and r_{\max} (Appendix A), a second-order Taylor expansion of the distribution function (Appendix D), expressions for the velocity dispersion and the kinetic energy in the presence of an additional baryonic component (Appendix C), and series expansions of the lensing properties (Appendix F). Table 2 summarizes the analytic expressions available for the DZ profile. The systematic test on the NIHAO simulations enables us to quantitatively show that the DZ profile provides better fits to the density and circular velocity profiles of DM haloes than the other two-parameter Einasto and generalized NFW with variable inner slope profiles, in particular in the innermost regions (Section 3.2).

But most importantly, this test enables us to describe the mass dependence of the inner slope s_1 and concentration parameters c_2 associated with the DZ profile (Section 3.3) and to establish it as a mass-dependent profile (Section 4) on par with the double power-law Di Cintio+ profile proposed by Di Cintio et al. (2014b) – with the advantage to have analytic expressions for many of its properties and only two shape parameters instead of four. We show that both s_1 and c_2 correlate with stellar and halo mass, especially with the stellar-to-halo mass ratio $M_{\text{star}}/M_{\text{vir}}$, and we provide fitting functions for the corresponding relations. The inner logarithmic slope s_1 corresponds to the NFW slope for $\log(M_{\text{star}}/M_{\text{vir}}) \leq -4$, to flatter inner density profiles for $\log(M_{\text{star}}/M_{\text{vir}})$ between -3.5 and -2 , and to steeper-than-NFW inner density profiles for $\log(M_{\text{star}}/M_{\text{vir}}) > -2$ (Fig. 9, Eq. (45), and Table 1). The concentration c_2 similarly corresponds to the NFW concentration at low $M_{\text{star}}/M_{\text{vir}}$, becomes slightly ($\sim 20\%$) smaller than the NFW concentration for $\log(M_{\text{star}}/M_{\text{vir}})$ between -3.5 and -2 , and increases

Table 2. Analytic expressions for the DZ profile, which depends on two shape parameters – a and c , or equivalently, the inner slope s_1 and the concentration c_2 .

Quantity	Equation
Density	$\rho(r) = \frac{\rho_c}{x^a (1 + x^{1/2})^{2(3.5-a)}}$ with $x = \frac{r}{r_c}$
Characteristic radius	$r_c = R_{\text{vir}}/c$
Characteristic density	$\rho_c = (1 - a/3)\bar{\rho}_c$
Characteristic av. density	$\bar{\rho}_c = c^3 \mu \bar{\rho}_{\text{vir}}$
Average virial density	$\bar{\rho}_{\text{vir}} = 3M_{\text{vir}}/4\pi R_{\text{vir}}^3 = \Delta\rho_{\text{crit}}$
Mass factor	$\mu = c^{a-3}(1 + c^{1/2})^{2(3-a)}$
Inner slope s_1 from a, c	Eq. (12)
Concentration c_2 from a, c	Eq. (13)
Parameter a from s_1, c_2	Eq. (14)
Parameter c from s_1, c_2	Eq. (15)
Core radius r_{core}	Eq. (16)
Half-mass radius and r_f	Eq. (17)
Maximum velocity radius r_{\max}	Eq. (A1) with $b = 2$ and $\bar{g} = 3$
Maximum velocity V_{\max}	Eq. (A2) with $b = 2$ and $\bar{g} = 3$
Concentration c_{\max} from a, c	Eq. (A7)
Parameter a from s_1, c_{\max}	Eq. (A8)
Parameter c from s_1, c_{\max}	Eq. (A9)
Average density	Eq. (4) with $b = 2$ and $\bar{g} = 3$
Enclosed mass	Eq. (5)
Circular velocity	Eq. (6)
Gravitational force	Eq. (7)
Logarithmic slope	Eq. (9) with $b = 2$ and $\bar{g} = 3$
Gravitational potential	Eq. (19)
Velocity dispersion	Eqs. (22), (B1) and (B3)
Surface density	Eqs. (32) and (F5)
Average surface density	Eqs. (41) and (F10)
Projected mass	Eqs. (34) and (F6)
Deflection angle	Eq. (38) and from Eq. (F6)
Lensing shear	Eq. (39)
Lensing potential	Eqs. (F8) and (F9)
Distribution function	Eqs. (D5) and (D6) (integral forms)
$s_1(M_{\text{star}}/M_{\text{vir}})$	Eqs. (45) and (48), Table 1
$c_2(M_{\text{star}}/M_{\text{vir}})$	Eqs. (49) and (47), Table 1

exponentially compared to NFW for $\log(M_{\text{star}}/M_{\text{vir}}) > -2$ (Fig. 9, Eq. (49), and Table 1). In terms of stellar mass, the range for core formation and halo expansion corresponds to 10^7 to $10^{10} M_\odot$.

The DZ profile thus enables to follow the expansion of the halo due to baryons in the mass range with $\log(M_{\text{star}}/M_{\text{vir}})$ between -3.5 and -2 not only in terms of inner logarithmic slope as for the Di Cintio+ profile but also in terms of concentration – i.e., at larger radii than those concerned by the inner slope. With the fitting functions of s_1 and c_2 as functions of $M_{\text{star}}/M_{\text{vir}}$, the DM distribution in haloes ranging from dwarfs to Milky-Way-like in stellar mass is set by the stellar and halo masses. We show that the mass-dependent DZ profile thus established is as accurate as the multi-parameter Di Cintio+ profile to describe density and circular velocity profiles of DM haloes (Section 4.2), in particular when the concentration parameter is left free (Section 4.3). In Fig. 15, we compare the DZ profile with existing parametrisations of DM halo density profiles, emphasizing on the number of parameters, the availability of analytic expressions, and the availability of mass-dependent prescriptions derived from simulations. Amongst the parametrisations with variable inner slope, the DZ profile stands out for its available analytic expressions and its mass-dependent prescriptions as a function of the stellar-to-halo mass ratio, taking into account the effect of baryons.

We caution that this study relies on a specific suite of hydro-

Profile	Expression & shape parameters	Analytic expressions c_2 $M(r)$ $V(r)$ $\sigma_r(r)$ $\Phi(r)$ $\Sigma(r)$ $\bar{\Sigma}(r)$ $f(\mathcal{E})$	Mass-dependence
NFW NFW 1996 An & Zhao 2013 superNFW Lilley+2018	$\rho = \frac{\rho_c}{x(1+x^2)}$ $\rho = \frac{\rho_c}{x(1+x)^{5/2}}$	c c	$c(M_{\text{halo}})$ \times
pISO Burkert 1995 Lucky13 Li+2020	$\rho = \frac{\rho_c}{1+x^2}$ $\rho = \frac{\rho_c}{(1+x)(1+x^2)}$ $\rho = \frac{\rho_c}{(1+x)^3}$	c c c	\times \times \times
Einasto Einasto 1965 An & Zhao 2013 coreEinasto Lazar+2020 $\alpha\beta\gamma$ /Di Cintio Zhao 1996 Di Cintio+2014 gNFW coreNFW Read+2016	$\rho = \rho_c \exp\left[-\frac{2}{\alpha}(x^\alpha - 1)\right]$ $\rho = \rho_c \exp\left[\frac{-2}{\alpha}((x+x_c)^\alpha - 1)\right]$ $\rho = \frac{\rho_c}{x^a(1+x^{1/b})^{b(g-a)}}$ $\rho = \frac{\rho_c}{x^a(1+x)^{3-a}}$ $M = f^n M_{\text{NFW}}, f = \tanh(r/r_c)$	c, α c, x_c, α c, a, b, g c, a c, r_c, n	\times $r_c(x_M), c_2(x_M)$ with $\alpha=0.16$ $a(x_M), b(x_M), g(x_M), c_2(x_M)$ \times $c(M_{\text{halo}})$
Dekel-Zhao Zhao 1996 Dekel+2017 Freundlich+2020	$\rho = \frac{\rho_c}{x^a(1+x^{1/2})^{2(3.5-a)}}$	c, a (or c_2, s_1)	$c_2(x_M), s_1(x_M)$

$x = r/r_s$ $c = R_{\text{vir}}/r_s$ $x_M = M_{\text{star}}/M_{\text{halo}}$ $c_2 = R_{\text{vir}}/r_{-2}$ \checkmark available \times non-elementary functions \times not available \times only certain cases

Figure 15. The Dekel-Zhao (DZ) profile against other existing parametrisations of DM halo density profiles. For each parametrisation, we indicate the analytic expression of the density (or mass), its shape parameters, whether analytic expressions for the concentration (c_2) where the logarithmic density slope equals 2 in absolute value, enclosed mass (M), circular velocity (V), radial velocity dispersion (σ_r), gravitational potential (Φ), projected surface density (Σ), average surface density ($\bar{\Sigma}$), and distribution function (f) are available to the best of our knowledge, and whether the shape parameters have been expressed as functions of the stellar and halo masses (M_{star} and M_{halo}) using numerical simulations. The projected surface densities Σ and $\bar{\Sigma}$ enable to define lensing properties such as the convergence, the shear and the magnification. The parametrisations listed alongside the DZ profile include the NFW (e.g. Navarro et al. 1996, 1997; Lokas & Mamon 2001; Evans & An 2006; Elíasdóttir & Möller 2007, AZ13) and “superNFW” (Lilley et al. 2018) cuspy profiles, the pseudo-isothermal (pISO), Burkert (1995), and “Lucky13” (Li et al. 2020) cored profiles, and the Einasto (e.g., Einasto 1965; Retana-Montenegro et al. 2012; Dutton & Macciò 2014, AZ13), “core-Einasto” (Lazar et al. 2020), double power-law $\alpha\beta\gamma$ (e.g., Z96, AZ13, Di Cintio et al. 2014b), generalized NFW (gNFW, e.g., Umetsu et al. 2011; Mamon et al. 2019), and “core-NFW” (Read et al. 2016) profiles with flexible inner slope, more suited to describe the diversity of DM halo shapes in the presence of baryons. The “core-Einasto” profile can become a two-parameter profile by fixing its parameter α (Lazar et al. 2020), but limited to fitting cored profiles in a certain mass range. For the double power-law $\alpha\beta\gamma$ profile (Eq. (2)), $M(r)$, $V(r)$, $\sigma_r(r)$, and $\Phi(r)$ can be expressed using elementary functions in certain cases, in particular within the family of profiles with $b = n$ and $g = 3 + k/n$ where k, n are natural integers (Z96, AZ13). The Di Cintio+ profile corresponds to a double power-law profile whose shape parameters are set by the stellar-to-halo mass ratio (Di Cintio et al. 2014b). In this case, only c_2 , $M(r)$, and $V(r)$ have analytic expressions (using non-elementary functions for the latter two). The mass-dependent prescriptions as a function of halo mass for the NFW and Einasto profiles stem from dark matter only simulations (e.g., Dutton & Macciò 2014). The DZ profile is a double-law profile with $b = 2$ and $g = 3.5$. We show in Section 3.2 that it provides better fits to simulated density profiles and rotation curves than the Einasto and gNFW profiles, with the same number of free parameters, and in Section 4.3 that its mass-dependent prescriptions are as accurate as the Di Cintio et al. (2014b) prescriptions. The DZ profile stands out amongst the parametrisations with variable inner slope for its available analytic expressions and its mass-dependent prescriptions as a function of the stellar-to-halo mass ratio, taking into account the effect of baryons.

dynamical cosmological simulations (NIHAO; Wang et al. 2015), which is notably characterised by a strong stellar feedback implementation with a blast-wave formalism and delayed cooling and no AGN feedback. We note that the Di Cintio+ profile was proposed using a previous suite of simulations (MaGICC; Brook et al. 2012; Stinson et al. 2013) with a similar implementation. Other simulation suites with different feedback schemes (e.g., Mashchenko et al. 2008; Teyssier et al. 2013; Madau et al. 2014; Verbeke et al. 2015; Read et al. 2016) suggest a similar behaviour of the inner density profile of DM haloes as a function of the stellar-to-halo mass ratio. This behaviour can be understood in theoretical terms as a competition between outflows induced by feedback and the confinement imposed by the halo gravity (e.g., Dekel & Silk 1986; Read & Gilmore 2005; Peñarrubia et al. 2012; Pontzen & Governato 2012; Dutton et al. 2016b; El-Zant et al. 2016, F20). As such,

the halo response to baryonic processes may not necessarily depend on the details of the feedback implementation as long as outflows are well-reproduced in the simulations. These outflows are expected to affect the stellar and gaseous components of galaxies, such that the good agreement of NIHAO galaxies with observations in terms of morphologies, color, sizes and rotation curves (Wang et al. 2015; Stinson et al. 2015; Dutton et al. 2016a, 2017; Obreja et al. 2019; Santos-Santos et al. 2020) may reflect outflows comparable to those of actual galaxies (Tollet et al. 2019) and of other simulation suites reproducing the aforementioned observables. We leave detailed tests of the DZ profile in other simulation suites with different feedback implementations for future work.

The accuracy of the DZ profile to describe the DM distributions of simulated haloes makes it a useful tool to study the evolution of DM density profiles, to model rotation curves of galax-

ies, to parametrize gravitational lenses, and to implement in semi-analytical models of galaxy formation and evolution. The analytic expressions for the gravitational potential, the velocity dispersion and the lensing properties can notably be used to model core formation in DM haloes from outflow episodes resulting from feedback, as in F20, to model gravitational lenses, to generate halo potentials or initial conditions for simulations, to compare different DM distributions in semi-analytical models (Jiang et al. 2020), and to quantify simulated and observed rotation curves of galaxies without numerical integrations.

ACKNOWLEDGEMENTS

We thank the referee, HongSheng Zhao, for a detailed and constructive report. We acknowledge A. Wasserman and N. Bouché for providing observational incentives for this work. We thank G. Mamon, A. Burkert, F. Combes, K. Kaur, K. Sarkar, A. Zitrin, F. Lelli, B. Famaey, and K. Malhan for stimulating discussions; D. Maoz for his support. This work has received funding from the European Research Council (ERC) under the European Union's Horizon 2020 research and innovation programme PE9 ERC-2018-ADG. This work was partly supported by the grants France-Israel PICS, I-CORE Program of the PBC/ISF 1829/12, BSF 2014-273, NSF AST-1405962, GIF I-1341-303.7/2016, and DIP STE1869/2-1 GE625/17-1. NIHAO simulations were carried out at the Gauss Centre for Super-computing e.V. (www.gauss-centre.eu) at the GCS Supercomputer SuperMUCat Leibniz Supercomputing Centre (www.lrz.de) and on the High Performance Computing resources at New York University Abu Dhabi. We used the software pynbody (Pontzen et al. 2013) for our analyses.

DATA AVAILABILITY

We provide codes to implement the DZ profile at https://github.com/JonathanFreundlich/Dekel_profile. The simulation data underlying this article will be shared on reasonable request to the corresponding author.

REFERENCES

Adamchick V., 1996, *Mathematica in Education and Research*, 5, 16
 Adams J. J., et al., 2014, *ApJ*, 789, 63
 Allaert F., Gentile G., Baes M., 2017, *A&A*, 605, A55
 An J., Zhao H., 2013, *MNRAS*, 428, 2805
 Baes M., Gentile G., 2011, *A&A*, 525, A136
 Baes M., van Hese E., 2011, *A&A*, 534, A69
 Behroozi P. S., Wechsler R. H., Conroy C., 2013, *ApJ*, 770, 57
 Behroozi P., Wechsler R. H., Hearin A. P., Conroy C., 2019, *MNRAS*, 488, 3143
 Binney J., Tremaine S., 2008, *Galactic Dynamics*. Princeton U. Press
 Blank M., Macciò A. V., Dutton A. A., Obreja A., 2019, *MNRAS*, 487, 5476
 Blumenthal G. R., Faber S. M., Flores R., Primack J. R., 1986, *ApJ*, 301, 27
 Brook C. B., Stinson G., Gibson B. K., Wadsley J., Quinn T., 2012, *MNRAS*, 424, 1275
 Bryan G. L., Norman M. L., 1998, *ApJ*, 495, 80
 Bullock J. S., Kolatt T. S., Sigad Y., Somerville R. S., Kravtsov A. V., Klypin A. A., Primack J. R., Dekel A., 2001, *MNRAS*, 321, 559
 Burkert A., 1995, *ApJ*, 447, L25
 Carleton T., Errani R., Cooper M., Kaplinghat M., Peñarrubia J., Guo Y., 2019, *MNRAS*, 485, 382

Cautun M., et al., 2020, *MNRAS*, 494, 4291
 Chan T. K., Kereš D., Oñorbe J., Hopkins P. F., Muratov A. L., Faucher-Giguère C. A., Quataert E., 2015, *MNRAS*, 454, 2981
 Chandrasekhar S., 1943, *ApJ*, 97, 255
 Cole D. R., Dehnen W., Wilkinson M. I., 2011, *MNRAS*, 416, 1118
 Dehnen W., 1993, *MNRAS*, 265, 250
 Dekel A., Silk J., 1986, *ApJ*, 303, 39
 Dekel A., Devor J., Hetzroni G., 2003a, *MNRAS*, 341, 326
 Dekel A., Arad I., Devor J., Birnboim Y., 2003b, *ApJ*, 588, 680
 Dekel A., Ishai G., Dutton A. A., Macciò A. V., 2017, *MNRAS*, 468, 1005
 Del Popolo A., 2009, *ApJ*, 698, 2093
 Di Cintio A., Brook C. B., Macciò A. V., Stinson G. S., Knebe A., Dutton A. A., Wadsley J., 2014a, *MNRAS*, 437, 415
 Di Cintio A., Brook C. B., Dutton A. A., Macciò A. V., Stinson G. S., Knebe A., 2014b, *MNRAS*, 441, 2986
 Dutton A. A., Macciò A. V., 2014, *MNRAS*, 441, 3359
 Dutton A. A., Macciò A. V., Frings J., Wang L., Stinson G. S., Penzo C., Kang X., 2016a, *MNRAS*, 457, L74
 Dutton A. A., et al., 2016b, *MNRAS*, 461, 2658
 Dutton A. A., et al., 2017, *MNRAS*, 467, 4937
 Eddington A. S., 1916, *MNRAS*, 76, 572
 Einasto J., 1965, *Trudy Astrofizicheskogo Instituta Alma-Ata*, 5, 87
 El-Zant A., Shlosman I., Hoffman Y., 2001, *ApJ*, 560, 636
 El-Zant A. A., Hoffman Y., Primack J., Combes F., Shlosman I., 2004, *ApJ*, 607, L75
 El-Zant A. A., Freundlich J., Combes F., 2016, *MNRAS*, 461, 1745
 Elíasdóttir Á., Möller O., 2007, *J. Cosmology Astropart. Phys.*, 2007, 006
 Evans N. W., 1994, *MNRAS*, 267, 333
 Evans N. W., An J. H., 2006, *Phys. Rev. D*, 73, 023524
 Fikioris G., 2007, *Mellin-Transform Method for Integral Evaluation: Introduction and Applications to Electromagnetics*. Morgan & Claypool
 Flores R. A., Primack J. R., 1994, *ApJ*, 427, L1
 Fox C., 1961, *Trans. Amer. Math. Soc.*, 98, 395
 Freundlich J., Dekel A., Jiang F., Ishai G., Cornuault N., Lapiner S., Dutton A. A., Macciò A. V., 2020, *MNRAS*, 491, 4523
 Gao L., Navarro J. F., Cole S., Frenk C. S., White S. D. M., Springel V., Jenkins A., Neto A. F., 2008, *MNRAS*, 387, 536
 Gnedin O. Y., Kravtsov A. V., Klypin A. A., Nagai D., 2004, *ApJ*, 616, 16
 Goerdt T., Moore B., Read J. I., Stadel J., 2010, *ApJ*, 725, 1707
 Golse G., Kneib J. P., 2002, *A&A*, 390, 821
 Governato F., et al., 2010, *Nature*, 463, 203
 Governato F., et al., 2012, *MNRAS*, 422, 1231
 Hernquist L., 1990, *ApJ*, 356, 359
 Jaffe W., 1983, *MNRAS*, 202, 995
 Jiang F., Dekel A., Freundlich J., den van Bosch F. C., Green S. B., Hopkins P. F., Benson A., Du X., 2020, *arXiv e-prints*, p. arXiv:2005.05974
 Jing Y. P., Suto Y., 2000, *ApJ*, 529, L69
 Kilbas A. A., Saigo M., 1999, *J. Appl. Math. Stochast. Anal.*, 12, 191
 Kilbas A. A., Saigo M., 2004, *H-Transforms: Theory and Applications*. CRC Press
 Kuzio de Naray R., Spekkens K., 2011, *ApJ*, 741, L29
 Lazar A., et al., 2020, *MNRAS*, 497, 2393
 Li P., Lelli F., McGaugh S., Schombert J., 2020, *ApJS*, 247, 31
 Lilley E. J., Evans N. W., Sanders J. L., 2018, *MNRAS*, 476, 2086
 Łokas E. L., Mamon G. A., 2001, *MNRAS*, 321, 155
 Macciò A. V., Dutton A. A., van den Bosch F. C., 2008, *MNRAS*, 391, 1940
 Macciò A. V., Stinson G., Brook C. B., Wadsley J., Couchman H. M. P., Shen S., Gibson B. K., Quinn T., 2012, *ApJ*, 744, L9
 Macciò A. V., Crespi S., Blank M., Kang X., 2020, *MNRAS*
 Madau P., Shen S., Governato F., 2014, *ApJ*, 789, L17
 Mamon G. A., Biviano A., Murante G., 2010, *A&A*, 520, A30
 Mamon G. A., Cava A., Biviano A., Moretti A., Poggianti B., Bettoni D., 2019, *A&A*, 631, A131
 Marichev O. I., 1983, *Handbook of integral transforms of higher transcendental functions: theory and algorithmic tables*. Ellis Horwood series in mathematics and its applications, Horwood, Chichester
 Martizzi D., Teyssier R., Moore B., 2013, *MNRAS*, 432, 1947
 Mashchenko S., Couchman H. M. P., Wadsley J., 2006, *Nature*, 442, 539

- Mashchenko S., Wadsley J., Couchman H. M. P., 2008, *Science*, 319, 174
- Mathai A. M., Saxena R. M., 1978, *The H Function with Applications in Statistics and Other Disciplines*. Wiley
- Mathai A. M., Saxena R. M., Haubold H. J., 2009, *The H-Function: Theory and Applications*. Springer
- Mazure A., Capelato H. V., 2002, *A&A*, 383, 384
- McGaugh S. S., de Blok W. J. G., 1998, *ApJ*, 499, 41
- Meijer C. S., 1936, *Nieuw Archief voor Wiskunde*, 18, 10
- Meneghetti M., Bartelmann M., Moscardini L., 2003, *MNRAS*, 340, 105
- Merritt D., Graham A. W., Moore B., Diemand J., Terzić B., 2006, *AJ*, 132, 2685
- Moore B., 1994, *Nature*, 370, 629
- More S., van den Bosch F. C., Cacciato M., Mo H. J., Yang X., Li R., 2009, *MNRAS*, 392, 801
- More S., Diemer B., Kravtsov A. V., 2015, *ApJ*, 810, 36
- Moster B. P., Naab T., White S. D. M., 2013, *MNRAS*, 428, 3121
- Navarro J. F., Frenk C. S., White S. D. M., 1996, *ApJ*, 462, 563
- Navarro J. F., Frenk C. S., White S. D. M., 1997, *ApJ*, 490, 493
- Navarro J. F., et al., 2004, *MNRAS*, 349, 1039
- Navarro J. F., et al., 2010, *MNRAS*, 402, 21
- Newman A. B., Treu T., Ellis R. S., Sand D. J., Nipoti C., Richard J., Jullo E., 2013a, *ApJ*, 765, 24
- Newman A. B., Treu T., Ellis R. S., Sand D. J., 2013b, *ApJ*, 765, 25
- Nipoti C., Binney J., 2015, *MNRAS*, 446, 1820
- Oñorbe J., Domínguez-Tenreiro R., Sáiz A., Serna A., 2007, *MNRAS*, 376, 39
- Obreja A., et al., 2019, *MNRAS*, 487, 4424
- Oh S.-H., de Blok W. J. G., Brinks E., Walter F., Kennicutt Jr. R. C., 2011, *AJ*, 141, 193
- Oh S.-H., et al., 2015, *AJ*, 149, 180
- Oldham L. J., Auger M. W., 2016, *MNRAS*, 457, 421
- Peñarrubia J., Pontzen A., Walker M. G., Koposov S. E., 2012, *ApJ*, 759, L42
- Peirani S., et al., 2017, *MNRAS*, 472, 2153
- Planck Collaboration et al., 2014, *A&A*, 571, A16
- Pontzen A., Governato F., 2012, *MNRAS*, 421, 3464
- Pontzen A., Governato F., 2014, *Nature*, 506, 171
- Pontzen A., Roškar R., Stinson G., Woods R., 2013, pynbody: N-Body/SPH analysis for python, Astrophysics Source Code Library (ascl:1305.002)
- Prada F., Klypin A. A., Cuesta A. J., Betancort-Rijo J. E., Primack J., 2012, *MNRAS*, 423, 3018
- Read J. I., Gilmore G., 2005, *MNRAS*, 356, 107
- Read J. I., Agertz O., Collins M. L. M., 2016, *MNRAS*, 459, 2573
- Reddick R. M., Wechsler R. H., Tinker J. L., Behroozi P. S., 2013, *ApJ*, 771, 30
- Retana-Montenegro E., van Hese E., Gentile G., Baes M., Frutos-Alfaro F., 2012, *A&A*, 540, A70
- Rodríguez-Puebla A., Primack J. R., Avila-Reese V., Faber S. M., 2017, *MNRAS*, 470, 651
- Romano-Díaz E., Shlosman I., Hoffman Y., Heller C., 2008, *ApJ*, 685, L105
- Santos-Santos I. M. E., et al., 2020, *MNRAS*, 495, 58
- Savitzky A., Golay M. J. E., 1964, *Analytical Chemistry*, 36, 1627
- Schaller M., et al., 2015, *MNRAS*, 451, 1247
- Schneider P., Ehlers J., Falco E. E., 1992, *Gravitational Lenses*, doi:10.1007/978-3-662-03758-4.
- Shen S., Wadsley J., Stinson G., 2010, *MNRAS*, 407, 1581
- Springel V., et al., 2008, *MNRAS*, 391, 1685
- Srivastava H. M., Gupta K. C., Goyal S. P., 1982, *The H-Function of One and Two Variables with Applications*. South Asian Publishers
- Stinson G., Seth A., Katz N., Wadsley J., Governato F., Quinn T., 2006, *MNRAS*, 373, 1074
- Stinson G. S., Brook C., Macciò A. V., Wadsley J., Quinn T. R., Couchman H. M. P., 2013, *MNRAS*, 428, 129
- Stinson G. S., et al., 2015, *MNRAS*, 454, 1105
- Stoeck F., 2006, *MNRAS*, 365, 147
- Teyssier R., Pontzen A., Dubois Y., Read J. I., 2013, *MNRAS*, 429, 3068
- Tollet É., Cattaneo A., Macciò A. V., Dutton A. A., Kang X., 2019, *MNRAS*, 485, 2511
- Tonini C., Lapi A., Salucci P., 2006, *ApJ*, 649, 591
- Tremaine S., Weinberg M. D., 1984, *MNRAS*, 209, 729
- Tremaine S., Richstone D. O., Byun Y.-I., Dressler A., Faber S. M., Grillmair C., Kormendy J., Lauer T. R., 1994, *AJ*, 107, 634
- Umetsu K., Broadhurst T., Zitrin A., Medezinski E., Coe D., Postman M., 2011, *ApJ*, 738, 41
- Verbeke R., Vandenbroucke B., De Rijcke S., 2015, *ApJ*, 815, 85
- Wadsley J. W., Veeravalli G., Couchman H. M. P., 2008, *MNRAS*, 387, 427
- Wadsley J. W., Keller B. W., Quinn T. R., 2017, *MNRAS*, 471, 2357
- Wang L., Dutton A. A., Stinson G. S., Macciò A. V., Penzo C., Kang X., Keller B. W., Wadsley J., 2015, *MNRAS*, 454, 83
- Wasserman A., et al., 2019, *ApJ*, 885, 155
- Wechsler R. H., Bullock J. S., Primack J. R., Kravtsov A. V., Dekel A., 2002, *ApJ*, 568, 52
- Weinberg M. D., Katz N., 2002, *ApJ*, 580, 627
- Zhao H., 1996, *MNRAS*, 278, 488
- Zhao H., 1997, *MNRAS*, 287, 525
- Zolotov A., et al., 2012, *ApJ*, 761, 71
- de Blok W. J. G., 2010, *Advances in Astronomy*, 2010, 789293
- de Blok W. J. G., Walter F., Brinks E., Trachternach C., Oh S.-H., Kennicutt Jr. R. C., 2008, *AJ*, 136, 2648
- van Dokkum P., et al., 2019, *ApJ*, 880, 91
- van den Bosch F. C., Swaters R. A., 2001, *MNRAS*, 325, 1017

APPENDIX A: PROFILE PARAMETERS IN TERMS OF R_{MAX} AND V_{MAX}

In certain situations, it may be useful to express the density profile of Eq. (8) – or the average density profile of Eq. (4) – in terms of the radius r_{max} at which the circular velocity peaks and $V_{\text{max}} = V(r_{\text{max}})$ the maximum velocity instead of R_{vir} and M_{vir} . This can be achieved by writing r_c and $\bar{\rho}_c$ in terms of these two parameters. The circular velocity (Eq. (6)) peaks at r_{max} such that

$$r_c = \left(\frac{\bar{g} - 2}{2 - a} \right)^b r_{\text{max}} \quad (\text{A1})$$

while the expression of the enclosed mass (Eq. (5)) yields

$$V_{\text{max}}^2 = \frac{GM(r_{\text{max}})}{r_{\text{max}}} = \frac{G\mu M_{\text{vir}}}{r_{\text{max}}} \left(\frac{(2-a)^{3-a}}{(\bar{g}-2)^{3-\bar{g}}(\bar{g}-a)^{\bar{g}-a}} \right)^b \quad (\text{A2})$$

and hence

$$\bar{\rho}_c = \frac{3\mu M_{\text{vir}}}{4\pi r_c^3} = \frac{3V_{\text{max}}^2}{4\pi G r_{\text{max}}^2} \left(\frac{(2-a)^a(\bar{g}-a)^{\bar{g}-a}}{(\bar{g}-2)^{\bar{g}}} \right)^b. \quad (\text{A3})$$

In particular, the virial radius of subhaloes is difficult to define in practice so semi-analytical models of satellite evolution may prefer to express subhalo properties in terms of r_{max} and V_{max} (e.g., Jiang et al. 2020).

Given R_{vir} and M_{vir} , the values of r_{max} and V_{max} further enable to retrieve the shape parameters of a DZ halo. For a DZ profile with $\bar{g} = 3$ and $b = 2$, we indeed have

$$\frac{r_{\text{max}}}{R_{\text{vir}}} = \frac{(2-a)^2}{c} = \frac{2.25}{c_2} \quad (\text{A4})$$

and

$$\left(\frac{V_{\text{max}}}{V_{\text{vir}}} \right)^2 = c^{a-2} (1 + c^{1/2})^{6-2a} (2-a)^{4-2a} (3-a)^{2a-6} \quad (\text{A5})$$

with $V_{\text{vir}} = GM_{\text{vir}}/R_{\text{vir}}$, which can also be expressed as a function of s_1 and c_2 using Eqs. (14) and (15). While the $V_{\text{max}}/V_{\text{vir}}$ velocity ratio only depends on the concentration for an NFW halo (e.g., Prada et al. 2012), it depends on the two shape parameters for a DZ profile. Fig. A1 shows how this ratio varies with the concentration c_2 for different values of s_1 (red lines) and compares it with the NFW relation (black dotted line). Having the values of $r_{\text{max}}/R_{\text{vir}}$ and $V_{\text{max}}/V_{\text{vir}}$ enables to retrieve the shape parameters by numerically solving Eqs. (A4) and (A5), as illustrated in the figure.

Radius r_{max} also defines a concentration $c_{\text{max}} \equiv R_{\text{vir}}/r_{\text{max}}$, which is

$$c_{\text{max}} = c \left(\frac{\bar{g} - 2}{2 - a} \right)^b \quad (\text{A6})$$

for the general double power-law profile of Eq. (4) and

$$c_{\text{max}} = \frac{c}{(2-a)^2} \quad (\text{A7})$$

for a DZ profile with $\bar{g} = 3$ and $b = 2$. In this case, there are bijections between the couples (a, c) , (s_1, c_2) , and (s_1, c_{max}) , with

$$a = \frac{s_1 - 2(3.5 - s_1)(r_1/R_{\text{vir}})^{1/2} c_{\text{max}}^{1/2}}{1 - (3.5 - s_1)(r_1/R_{\text{vir}})^{1/2} c_{\text{max}}^{1/2}} \quad (\text{A8})$$

and

$$c = \left(\frac{s_1 - 2}{(3.5 - s_1)(r_1/R_{\text{vir}})^{1/2} - c_{\text{max}}^{1/2}} \right)^2. \quad (\text{A9})$$

The couple (s_1, c_{max}) is thus equivalent to the other two couples to describe the DZ profile (cf. Section 2.2.1).

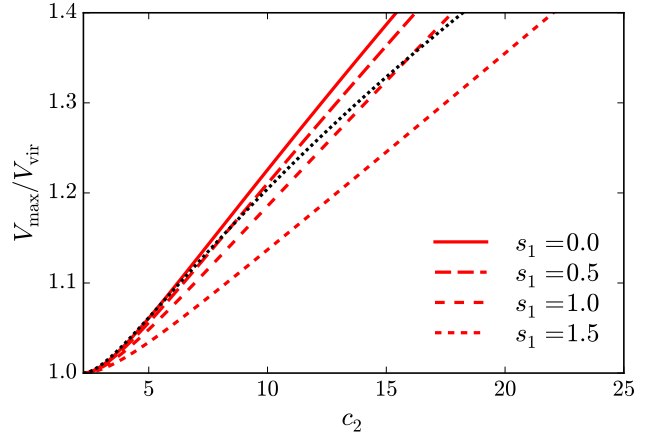


Figure A1. Relation between the ratio of the maximum circular velocity V_{max} to the circular velocity at the virial radius V_{vir} and the concentration c_2 for DZ profiles with different values of the inner slope s_1 . The black dotted line corresponds to the NFW relation, where the velocity ratio only depends on the concentration. The lower limit of the x-axis corresponds to $c_2 = 2.25$, for which $r_{\text{max}} = R_{\text{vir}}$ and $V_{\text{max}} = V_{\text{vir}}$.

APPENDIX B: THE VELOCITY DISPERSION AS A SUM OF ELEMENTARY FUNCTIONS

Eq. (22) expressing the velocity dispersion in a DZ halo involves incomplete beta functions, i.e., non-elementary functions. Following Eqs. (19) and (A.9)–(A.11) of Z96, this equation can also be expressed (see also D17, Eq. (A.10)) as the following sum:

$$\sigma_r^2(r) = 2c\mu \frac{GM_{\text{vir}}}{R_{\text{vir}}} x^a (1 + x^{1/2})^{2(3.5-a)} \sum_{i=0}^8 \frac{(-1)^i 8!}{i!(8-i)!} \frac{1 - \chi^{4(1-a)+i}}{4(1-a) + i}, \quad (\text{B1})$$

which only involves elementary functions, since $\chi = x^{1/2}/(1+x^{1/2})$. Alternatively, noticing that $\mathcal{B}(a, b, x) = a^{-1} x^a (1-x)^{b-1} + a^{-1} (b-1) \times \mathcal{B}(a+1, b-1, x)$, we can deduce that

$$\mathcal{B}(a, 9, x) = \sum_{i=0}^8 \frac{8!}{i!} \frac{\Gamma(a)}{\Gamma(a+9-i)} x^{a+8-i} (1-x)^i, \quad (\text{B2})$$

where Γ denotes the usual gamma function. This enables to write the local kinetic energy also as

$$\sigma_r^2(r) = 2c\mu \frac{GM_{\text{vir}}}{R_{\text{vir}}} x^a (1 + x^{1/2})^{2(3.5-a)} \left[\frac{8!\Gamma(4(1-a))}{\Gamma(4(1-a)+9)} - \sum_{i=0}^8 \frac{8!}{i!} \frac{\Gamma(4(1-a))}{\Gamma(4(1-a)+9-i)} \chi^{4(1-a)+8-i} (1-\chi)^i \right]. \quad (\text{B3})$$

The different expressions for σ_r^2 are formally equivalent, but our numerical implementation using `scipy` (cf. https://github.com/JonathanFreundlich/Dekel_profile) results in significantly larger numerical errors with Eq. (B1) than with Eqs. (22) and (B3).

APPENDIX C: POTENTIAL AND VELOCITY DISPERSION WITH AN ADDITIONAL MASS

In the presence of baryons or more generally when the DZ profile only describes part of the mass distribution, the enclosed mass

entering the integral defining the gravitational potential,

$$U_{\text{tot}}(r) = - \int_r^{R_{\text{vir}}} \frac{GM(y)}{y^2} dy - \frac{GM_{\text{vir}}}{R_{\text{vir}}} \quad (\text{C1})$$

for a halo truncated at the virial radius R_{vir} , and that defining the radial velocity dispersion (Eq. (20)) should include all components. We indicate here analytical expressions for the potential and the radial velocity dispersion of a DZ DM halo in the presence of an additional component, focussing on the following cases: (1) a radial power-law between the total mass and the dark matter mass, as assumed in F20; (2) an additional point mass at the center of the halo; (3) an additional sphere of constant density; and (4) an additional isothermal sphere. In this effect, we consider U_m and σ_m the contributions of the additional mass to the potential and radial velocity dispersion, such that

$$U_{\text{tot}} = U + U_m \quad (\text{C2})$$

and

$$\sigma_{r,\text{tot}}^2 = \sigma_r^2 + \sigma_m^2 \quad (\text{C3})$$

where U and σ_r are those of the DZ profile (Eqs. (19) and (22)).

C1 Power law multi-component halo

To account for the difference between the total enclosed mass M_{tot} and the enclosed dark matter mass M , we can model their ratio as a power law

$$\frac{M_{\text{tot}}}{M} = X_M \left(\frac{r}{R_{\text{vir}}} \right)^{-n}, \quad (\text{C4})$$

where X_M and n are adjustable parameters as in F20. With this parametrization, the gravitational potential from Eq. (C1) becomes

$$U_{\text{tot}}(r) = -X_M V_{\text{vir}}^2 \left(1 + \mu c^{n+1} \int_x^c \frac{1}{z^{a+n-1} (1+z^{1/2})^{2(3-a)}} dz \right) \quad (\text{C5})$$

$$= -X_M V_{\text{vir}}^2 \left(1 + 2\mu c^{n+1} \int_\chi^{\chi_c} \zeta^{3-2n-2a} (1-\zeta)^{1+2n} d\zeta \right) \quad (\text{C6})$$

$$U_{\text{tot}}(r) = -X_M V_{\text{vir}}^2 \left(1 + 2\mu c^{n+1} [\mathcal{B}(4-2n-2a, 2+2n, \zeta)]_{\chi}^{\chi_c} \right), \quad (\text{C7})$$

which reverts to Eq. (19) when $n = 0$ and $X_M = 1$. These calculations use the variable change $\zeta = z^{1/2}/(1+z^{1/2})$, highlighted for Eq. (18), and the incomplete beta function as in Eq. (22). The radial velocity dispersion per unit mass from Eq. (20) similarly becomes

$$\sigma_{r,\text{tot}}^2(r) = \mu X_M c^{n+1} V_{\text{vir}}^2 \frac{\rho_c}{\rho(r)} \int_x^\infty \frac{y^{1-2a-n}}{(1+y^{1/2})^{13-4a}} dy \quad (\text{C8})$$

$$= 2\mu X_M c^{n+1} V_{\text{vir}}^2 \frac{\rho_c}{\rho(r)} \int_\chi^1 \zeta^{3-4a-2n} (1-\zeta)^{8+2n} d\zeta \quad (\text{C9})$$

$$\sigma_{r,\text{tot}}^2(r) = 2\mu X_M c^{n+1} V_{\text{vir}}^2 \frac{\rho_c}{\rho(r)} [\mathcal{B}(4-4a-2n, 9+2n, \zeta)]_{\chi}^1, \quad (\text{C10})$$

which reverts to Eq. (22) when $n = 0$ and $X_M = 1$.

C2 Additional point mass

The contribution of an additional mass m at the center of the halo to the gravitational potential is

$$U_m = -\frac{Gm}{r}. \quad (\text{C11})$$

The corresponding contribution to the kinetic energy assuming isotropy can be derived from Eq. (20), with $\rho(r')$ the DZ density expressed in Eq. (11) and $M(r') = m$:

$$\sigma_m^2(r) = \frac{Gm}{\rho(r)} \int_r^\infty \rho(r') r'^{-2} dr' \quad (\text{C12})$$

$$= \frac{Gmc}{R_{\text{vir}}} \frac{\rho_c}{\rho(r)} \int_x^\infty \frac{1}{y^{2+a} (1+y^{1/2})^{2(3.5-a)}} dy \quad (\text{C13})$$

$$= \frac{2Gmc}{R_{\text{vir}}} \frac{\rho_c}{\rho(r)} \int_\chi^1 \zeta^{-3-2a} (1-\zeta)^8 d\zeta \quad (\text{C14})$$

$$\sigma_m^2(r) = \frac{2Gmc}{R_{\text{vir}}} \frac{\rho_c}{\rho(r)} [\mathcal{B}(-2-2a, 9, \zeta)]_{\chi}^1. \quad (\text{C15})$$

C3 Additional uniform sphere

The mass distribution of a uniform sphere of total mass m and radius r_m can be written as

$$m(r) = \begin{cases} m & \text{if } r \geq r_m \\ m \left(\frac{r}{r_m} \right)^3 & \text{if } r \leq r_m. \end{cases} \quad (\text{C16})$$

Its contribution to the gravitational potential according to Eq. (C1) is

$$U_m(r) = \begin{cases} -\frac{Gm}{r} & \text{if } r \geq r_m \\ -\frac{Gm}{2r_m} \left[3 - \left(\frac{r}{r_m} \right)^2 \right] & \text{if } r \leq r_m. \end{cases} \quad (\text{C17})$$

If $r \geq r_m$, its contribution to the radial velocity dispersion corresponds to that of a point mass m as in Eq. (C15), i.e.,

$$\sigma_m^2(r) = \frac{2Gmc}{R_{\text{vir}}} \frac{\rho_c}{\rho(r)} [\mathcal{B}(-2-2a, 9, \zeta)]_{\chi}^1. \quad (\text{C18})$$

However, if $r \leq r_m$, Eq. (20) yields

$$\sigma_m^2(r) = \frac{G}{\rho(r)} \left[\int_r^{r_m} \rho(r') m \left(\frac{r'}{r_m} \right)^3 r'^{-2} dr' + \int_{r_m}^\infty \rho(r') m r'^{-2} dr' \right], \quad (\text{C19})$$

where the second term corresponds to the contribution of a point mass m evaluated at r_m . Hence if $r \leq r_m$,

$$\sigma_m^2(r) = \frac{2Gmc}{R_{\text{vir}}} \frac{\rho_c}{\rho(r)} \left(\frac{1}{2x_m^3} \int_x^{x_m} \frac{dz}{z^{a-1} (1+z^{1/2})^{7-2a}} + [\mathcal{B}(-2-2a, 9, \zeta)]_{\chi_m}^1 \right) \quad (\text{C20})$$

$$= \frac{2Gmc}{R_{\text{vir}}} \frac{\rho_c}{\rho(r)} \left(\frac{1}{x_m^3} \int_\chi^{\chi_m} \zeta^{3-2a} (1-\zeta)^2 d\zeta + [\mathcal{B}(-2-2a, 9, \zeta)]_{\chi_m}^1 \right) \quad (\text{C21})$$

$$\sigma_m^2(r) = \frac{2Gmc}{R_{\text{vir}}} \frac{\rho_c}{\rho(r)} \left(\frac{1}{x_m^3} [\mathcal{B}(4-2a, 3, \zeta)]_{\chi}^{\chi_m} + [\mathcal{B}(-2-2a, 9, \zeta)]_{\chi_m}^1 \right) \quad (\text{C22})$$

where $x_m = r_m/r_c$ and $\chi_m = \chi(x_m)$.

C4 Additional singular isothermal sphere

The mass distribution of a singular isothermal sphere of total mass m and radius r_m can be written as

$$m(r) = \begin{cases} m & \text{if } r \geq r_m \\ m \left(\frac{r}{r_m} \right) & \text{if } r \leq r_m. \end{cases} \quad (\text{C23})$$

Its contribution to the gravitational potential according to Eq. (C1) is

$$U_m(r) = \begin{cases} -\frac{Gm}{r} & \text{if } r \geq r_m \\ -\frac{Gm}{r_m} \left[1 + \ln\left(\frac{r_m}{r}\right) \right] & \text{if } r \leq r_m. \end{cases} \quad (\text{C24})$$

If $r \geq r_m$, its contribution to the kinetic energy corresponds to that of a point mass m as in Eqs. (C15) and (C18). If $r \leq r_m$, Eq. (C19) yields

$$\sigma_m^2(r) = \frac{2Gmc}{R_{\text{vir}}} \frac{\rho_c}{\rho(r)} \left(\frac{1}{2x_m} \int_{x_m}^{x_m} \frac{dz}{z^{a+1}(1+z^{1/2})^{7-2a}} + [\mathcal{B}(-2-2a, 9, \zeta)]_{x_m}^1 \right) \quad (\text{C25})$$

$$= \frac{2Gmc}{R_{\text{vir}}} \frac{\rho_c}{\rho(r)} \left(\frac{1}{x_m} \int_{x_m}^{x_m} \zeta^{-1-2a}(1-\zeta)^6 d\zeta + [\mathcal{B}(-2-2a, 9, \zeta)]_{x_m}^1 \right) \quad (\text{C26})$$

$$\sigma_m^2(r) = \frac{2Gmc}{R_{\text{vir}}} \frac{\rho_c}{\rho(r)} \left(\frac{1}{x_m} [\mathcal{B}(-2a, 7, \zeta)]_{x_m}^{x_m} + [\mathcal{B}(-2-2a, 9, \zeta)]_{x_m}^1 \right). \quad (\text{C27})$$

APPENDIX D: NOTES ON THE DISTRIBUTION FUNCTION

The ergodic distribution function for a spherical density distribution can be recovered by Eddington's formula (Eddington 1916; Binney & Tremaine 2008, Eq. 4.46),

$$f(\mathcal{E}) = \frac{1}{\sqrt{8\pi}} \left[\int_0^\infty \frac{d\Psi}{\sqrt{\mathcal{E} - \Psi}} \frac{d^2\nu}{d\Psi^2} + \frac{1}{\sqrt{\mathcal{E}}} \left(\frac{d\nu}{d\Psi} \right)_{\Psi=0} \right], \quad (\text{D1})$$

where the relative potential $\Psi = -U$ is defined with respect to the potential at infinity and $\nu(r)$ is the probability density. For a DZ profile truncated at R_{vir} , the probability density corresponding to the mass density is

$$\nu(r) = \frac{(3-a)\mu c^3}{4\pi R_{\text{vir}}^3} \frac{1}{x^a(1+x^{1/2})^{2(3.5-a)}} \quad (\text{D2})$$

within R_{vir} and zero outside, with

$$\frac{d\nu}{d\Psi} = \frac{d\nu}{dx} \frac{dx}{d\Psi} = \frac{(3-a)c^2}{4\pi GR_{\text{vir}}^2 M_{\text{vir}}} \frac{a+3.5x^{1/2}}{x^2(1+x^{1/2})^2} \quad (\text{D3})$$

within R_{vir} and zero at $\Psi = 0$ when $x \rightarrow +\infty$ so the second term of Eq. (D1) vanishes,

$$\frac{d}{dx} \left(\frac{d\nu}{d\Psi} \right) = -\frac{(3-a)c^2}{4\pi GR_{\text{vir}}^2 M_{\text{vir}}} \frac{2a + (5.25 + 3a)x^{1/2} + 8.75x}{x^3(1+x^{1/2})^3} \quad (\text{D4})$$

within R_{vir} , and Eddington's formula can be rewritten

$$f(\mathcal{E}) = \frac{1}{\sqrt{8\pi}} \int_{\Psi^{-1}(\mathcal{E})}^\infty \frac{1}{\sqrt{\mathcal{E} - \Psi(x)}} \left| \frac{d}{dx} \left(\frac{d\nu}{d\Psi} \right) \right| dx, \quad (\text{D5})$$

introducing Ψ^{-1} the inverse function of Ψ . The distribution function $f(\mathcal{E})$ can be evaluated numerically from this equation, using the analytic expression of $\Psi(r) = -U(r)$ and Eq. (D4) while evaluating $\Psi^{-1}(\mathcal{E})$ numerically. Z96 gives an explicit analytic expression of $f(\mathcal{E})$ when $a = 1.5$ in their Eq. (27), but there is sadly no simple analytic expressions for $\Psi^{-1}(\mathcal{E})$ and $f(\mathcal{E})$ in the general case. It can however be shown (cf. below) and seen in the bottom right panel of Fig. 1 that the slope of $f(\mathcal{E})$ primarily depends on c_2 and only weakly on s_1 for $\mathcal{E}_0/V_{\text{vir}}^2 \lesssim 5$ while the trend reverses when \mathcal{E} approaches its maximum value $\Psi(0)$. The differences between the distributions functions shown in Fig. 1 mainly reflect the different

gravitational potentials: stars in the deeper potential of the more concentrated ($c_2 = 15$) haloes are distributed through larger volumes of phase space. We note that the DZ distribution function is always divergent as \mathcal{E} tends to the central $\Psi(0)$.

The integral of Eq. (D5) expressing the distribution function $f(\mathcal{E})$ from Eddington's formula can be integrated by parts twice to obtain

$$f(\mathcal{E}) = A \sqrt{\mathcal{E} - \Psi(c)} - B(\mathcal{E} - \Psi(c))^{3/2} - F[\mathcal{E}, \mathcal{E}] \quad (\text{D6})$$

with

$$A = \frac{-1}{\sqrt{2\pi}} \frac{g(c)}{\Psi'(c)}, \quad (\text{D7})$$

$$B = \frac{\sqrt{2}}{3\pi} \left(\frac{g'(c)\Psi'(c) - g(c)\Psi''(c)}{(\Psi'(c))^3} \right), \quad (\text{D8})$$

and

$$F[u, v] = \frac{\sqrt{2}}{3\pi} \int_{\Psi(c)}^u (v - y)^{3/2} h''(y) dy \quad (\text{D9})$$

where

$$g(x) \equiv \left| \frac{d}{dx} \left(\frac{d\nu}{d\Psi} \right) \right| \quad (\text{D10})$$

is expressed in Eq. (D4), and

$$h(y) = \frac{g(\Psi^{-1}(y))}{\Psi'(\Psi^{-1}(y))}. \quad (\text{D11})$$

Derivatives are indicated by primes. Eq. (D6) not only enables to minimize numerical errors when estimating $f(\mathcal{E})$, since the double integration by parts removes the $\sqrt{\mathcal{E} - \Psi(x)}$ denominator of the integrand of Eq. (D5), but also to expand $f(\mathcal{E})$ as a series around any energy \mathcal{E}_0 . In particular, if we define $\delta = \mathcal{E} - \mathcal{E}_0$, we can expand F for $u = v = \mathcal{E}_0 + \delta$ around $\delta = 0$. One gets at the first order

$$F[\mathcal{E}_0 + \delta, \mathcal{E}_0 + \delta] \simeq F[\mathcal{E}_0, \mathcal{E}_0] + \delta \left(\frac{\partial F}{\partial u} + \frac{\partial F}{\partial v} \right)_{\mathcal{E}_0, \mathcal{E}_0} \simeq F[\mathcal{E}_0, \mathcal{E}_0] + C\delta \quad (\text{D12})$$

where

$$C = \frac{1}{\sqrt{2\pi}} \int_c^{\Psi^{-1}(\mathcal{E}_0)} \sqrt{\mathcal{E}_0 - \Psi(x)} \eta(x) dx \quad (\text{D13})$$

with $\eta = \frac{\Lambda'}{\Psi''} - \frac{\Lambda\Psi''}{(\Psi')^2}$ and $\Lambda = \frac{g'}{\Psi''} - g\frac{\Psi''}{(\Psi')^2}$. Eq. (D12) yields

$$\log_{10} f(\mathcal{E}) \simeq \log_{10}(f(\mathcal{E}_0)) + \delta \frac{A - 3B(\mathcal{E}_0 - \Psi(c)) - 2C\sqrt{\mathcal{E}_0 - \Psi(c)}}{2\ln(10)f(\mathcal{E}_0)\sqrt{\mathcal{E}_0 - \Psi(c)}}, \quad (\text{D14})$$

which notably enables to express the slope of the distribution function and to show that it primarily depends on c_2 and only weakly on s_1 for $\mathcal{E}_0/V_{\text{vir}}^2 \lesssim 5$. Expansions at higher order can be similarly obtained. Alternatively, Zhao (1997) provides an analytic approximation to the distribution function.

APPENDIX E: ANALYTICAL LENSING PROPERTIES WITH THE MELLIN TRANSFORM METHOD

E1 Principle

The Mellin transform method (Marichev 1983; Adamchick 1996; Fikioris 2007) enables to express definite integrals as Mellin-Barnes integrals. It was notably used by Mazure & Capelato (2002),

Baes & van Hese (2011), Baes & Gentile (2011), and Retana-Montenegro et al. (2012) to obtain analytic expressions for projected quantities relevant to gravitational lensing from the three-dimensional Einasto profile.

The Mellin transform $\mathfrak{M}_f(u)$ of a function $f(z)$ is defined as

$$\mathfrak{M}_f(u) = \phi(u) = \int_0^{+\infty} f(z) z^{u-1} dz \quad (\text{E1})$$

and its inverse

$$\mathfrak{M}_\phi^{-1}(z) = f(z) = \frac{1}{2\pi i} \int_{\mathcal{L}} \phi(u) z^{-u} du, \quad (\text{E2})$$

where \mathcal{L} is a vertical line in the complex plane. The Mellin convolution of two functions $f_1(z)$ and $f_2(z)$ is defined as

$$(f_1 \star f_2)(z) = \int_0^{+\infty} f_1(t) f_2\left(\frac{z}{t}\right) \frac{dt}{t} \quad (\text{E3})$$

and, as for the better-known Fourier transform, the Mellin transform of a Mellin convolution of two functions is equal to the product of their Mellin transforms, i.e.,

$$\mathfrak{M}_{f_1 \star f_2}(u) = \mathfrak{M}_{f_1}(u) \times \mathfrak{M}_{f_2}(u). \quad (\text{E4})$$

It can be shown that any definite integral

$$f(z) = \int_0^{+\infty} g(t, z) dt \quad (\text{E5})$$

can be written as the Mellin convolution of two functions f_1 and f_2 and hence transformed into an inverse Mellin transform,

$$f(z) = \frac{1}{2\pi i} \int_{\mathcal{L}} \mathfrak{M}_{f_1}(u) \mathfrak{M}_{f_2}(u) z^{-u} du. \quad (\text{E6})$$

If f_1 and f_2 are hypergeometric functions, i.e., in a large number of cases, the integral of Eq. (E6) is a Mellin-Barnes integral that can be expressed as a Meijer G or a Fox H function (e.g., Meijer 1936; Fox 1961; Mathai & Saxena 1978; Srivastava et al. 1982; Kilbas & Saigo 1999, 2004; Mathai et al. 2009). Under certain conditions, these functions are analytical and the line integral can be evaluated using the residue theorem.

E2 Application to the surface density

The integral entering the expression of the surface density $\tilde{\Sigma}(X)$ (Eq. (28)) can be expressed with $z = 1$ as the Mellin convolution of

$$f_1(t) = 2\rho_c r_c \frac{t^2}{t^a(1+t^{1/2})^{2(3.5-a)}} \quad (\text{E7})$$

and

$$f_2(t) = \begin{cases} \frac{t}{\sqrt{1-X^2 t^2}} & \text{if } 0 \leq t \leq X^{-1} \\ 0 & \text{if } t > X^{-1}. \end{cases} \quad (\text{E8})$$

The Mellin transform of f_1 is

$$\mathfrak{M}_{f_1}(u) = 4\rho_c r_c \mathcal{B}(4+2u-2a, 3-2u) \quad (\text{E9})$$

with the variable change used for Eq. (18), while that of f_2 is

$$\mathfrak{M}_{f_2}(u) = \frac{\sqrt{\pi} \Gamma(\frac{1+u}{2})}{\Gamma(\frac{u}{2})} \frac{1}{u X^{1+u}} \quad (\text{E10})$$

as in Baes & van Hese (2011), Baes & Gentile (2011) and Retana-Montenegro et al. (2012). Following Eq. (E6), the surface density can thus be expressed as

$$\tilde{\Sigma}(R) = 4\sqrt{\pi} \rho_c r_c \frac{1}{2\pi i} \int_{\mathcal{L}} \mathcal{B}(4+2u-2a, 3-2u) \frac{\Gamma(\frac{1+u}{2})}{\Gamma(\frac{u}{2}) u X^{1+u}} du, \quad (\text{E11})$$

which becomes

$$\tilde{\Sigma}(R) = 4\sqrt{\pi} \rho_c r_c \frac{X}{2\pi i} \int_{\mathcal{L}} \frac{\Gamma(4y-2a)\Gamma(7-4y)}{\Gamma(7-2a)} \frac{\Gamma(y-\frac{1}{2})}{\Gamma(y)} [X^2]^{-y} dy \quad (\text{E12})$$

with the variable change $y = 1+u/2$ and $\mathcal{B}(a, b) = \Gamma(a)\Gamma(b)/\Gamma(a+b)$ (Eq. (30)). This integral is a Fox H function, specified in Eq. (32).

As a sanity check, Eq. (32) can be used to retrieve the total mass $M_{\text{tot}} = \mu M_{\text{vir}}$ of an untruncated DZ halo by integrating the surface density $\tilde{\Sigma}$ over the plane of the sky,

$$M_{\text{tot}} = 2\pi \int_0^{+\infty} \tilde{\Sigma}(R) R dR = \frac{4\pi^{3/2} \rho_c r_c^3}{\Gamma(7-2a)} \int_0^{+\infty} t^{1/2} H_{2,2}^{2,1} \left[\begin{matrix} (-6,4), (0,1) \\ (-\frac{1}{2},1), (-2a,4) \end{matrix} \middle| t \right] dt \quad (\text{E13})$$

with the variable change $t = X^{1/2}$. This integral, which is the Mellin transform of a Fox H function, can be calculated using Eq. (2.8) of Mathai et al. (2009). This yields

$$M_{\text{tot}} = \frac{4\pi^{3/2} \rho_c r_c^3}{\Gamma(7-2a)} \frac{\Gamma(1)\Gamma(6-2a)\Gamma(1)}{\Gamma(\frac{3}{2})} = \frac{4\pi \rho_c r_c^3}{3-a} = \mu M_{\text{vir}} \quad (\text{E14})$$

since $\rho_c = (3-a)\mu M_{\text{vir}}/4\pi r_c^3$.

APPENDIX F: SERIES EXPANSION OF THE LENSING PROPERTIES

F1 Principle

The Fox H function

$$H_{p,q}^{m,n} \left[\begin{matrix} (\mathbf{a}, \mathbf{A}) \\ (\mathbf{b}, \mathbf{B}) \end{matrix} \middle| z \right] = \frac{1}{2\pi i} \int_{\mathcal{L}} \frac{\prod_{j=1}^m \Gamma(b_j + B_j y) \prod_{j=1}^n \Gamma(1-a_j - A_j y)}{\prod_{j=m+1}^q \Gamma(1-b_j - B_j y) \prod_{j=n+1}^p \Gamma(a_j + A_j y)} z^{-y} dy \quad (\text{F1})$$

has analytical series expansions under certain conditions satisfied by the Fox H functions considered in this paper (cf. Kilbas & Saigo 1999; Mathai et al. 2009; Baes & van Hese 2011; Baes & Gentile 2011). As explicated in Appendix A of Baes & van Hese (2011), if all functions $\Gamma(b_i + B_i y)$ with $0 \leq i \leq m$ have only single poles $b_{i,k} = -(b_i + k)/B_i$,

$$H_{p,q}^{m,n} \left[\begin{matrix} (\mathbf{a}, \mathbf{A}) \\ (\mathbf{b}, \mathbf{B}) \end{matrix} \middle| z \right] = \sum_{i=1}^m \sum_{k=0}^{\infty} \frac{(-1)^k}{k! B_i} \frac{\prod_{j=1, j \neq i}^m \Gamma(b_j - B_j \frac{b_i+k}{B_i}) \prod_{j=1}^n \Gamma(1-a_j + A_j \frac{b_i+k}{B_i})}{\prod_{j=m+1}^q \Gamma(1-b_j + B_j \frac{b_i+k}{B_i}) \prod_{j=n+1}^p \Gamma(a_j - A_j \frac{b_i+k}{B_i})} z^{(b_i+k)/B_i}, \quad (\text{F2})$$

while if several gamma functions share the same pole, the Fox H function can be expressed as a logarithmic-power series rather than a power series (Kilbas & Saigo 1999). In the case where two gamma functions $\Gamma(b_i + B_i y)$ with $1 \leq i \leq m$ share at least one pole,

$$H_{p,q}^{m,n} \left[\begin{matrix} (\mathbf{a}, \mathbf{A}) \\ (\mathbf{b}, \mathbf{B}) \end{matrix} \middle| z \right] = \sum_{i,k}' \frac{(-1)^k}{k! B_i} \frac{\prod_{j=1, j \neq i}^m \Gamma(b_j - B_j \frac{b_i+k}{B_i}) \prod_{j=1}^n \Gamma(1-a_j + A_j \frac{b_i+k}{B_i})}{\prod_{j=m+1}^q \Gamma(1-b_j + B_j \frac{b_i+k}{B_i}) \prod_{j=n+1}^p \Gamma(a_j - A_j \frac{b_i+k}{B_i})} z^{(b_i+k)/B_i} \\ + \sum_{k_1}'' \frac{(-1)^{k_1+k_2}}{k_1! k_2! B_1 B_2} \frac{\prod_{j=3}^m \Gamma(b_j - B_j \frac{b_1+k_1}{B_1}) \prod_{j=1}^n \Gamma(1-a_j + A_j \frac{b_1+k_1}{B_1})}{\prod_{j=m+1}^q \Gamma(1-b_j + B_j \frac{b_1+k_1}{B_1}) \prod_{j=n+1}^p \Gamma(a_j - A_j \frac{b_1+k_1}{B_1})} \\ \times z^{(b_1+k_1)/B_1} (C_{k_1} - \ln z) \quad (\text{F3})$$

where the two gamma functions sharing poles are described by the first two indices $j = 1$ and $j = 2$, the first sum (with a prime) covers the single poles, the second sum (with a double prime) covers the second-order poles, $k_2 = B_2(b_1 + k_1)/B_1 - b_2$,

$$\begin{aligned} C_{k_1} = & B_1\psi(k_1 + 1) + B_2\psi(k_2 + 1) \\ & + \sum_{j=3}^m B_j\psi(b_j - B_j \frac{b_1 + k_1}{B_1}) - \sum_{j=1}^n A_j\psi(1 - a_j + A_j \frac{b_1 + k_1}{B_1}) \\ & + \sum_{j=m+1}^q B_j\psi(1 - b_j + B_j \frac{b_1 + k_1}{B_1}) - \sum_{j=n+1}^p A_j\psi(a_j - A_j \frac{b_1 + k_1}{B_1}), \end{aligned} \quad (\text{F4})$$

and ψ is the digamma function (Baes & van Hese 2011, Appendix A). Poles of the Fox H functions considered in this paper are of the form $a/2 - k/4$ and $n/2 - k$ where a is the DZ slope parameter and the n are odd integers. In most realistic cases, a is either a non-rational number or a rational number with an odd denominator such that the two types of poles do not overlap. In this case, it is Eq. (F2) that enables to express the different Fox H functions encountered in this article as series expansions. The following series expansions assume that a is either a non-rational number or a rational number with an odd denominator, but other series expressions could be deduced from Eq. (F3) if a were rational with an even denominator.

F2 Surface density

Assuming a to be either non-rational or rational with an even denominator, Eq. (32) and the series expansion (F2) yields for the surface density of an untruncated DZ profile

$$\begin{aligned} \bar{\Sigma}(X) = & \frac{4\sqrt{\pi}\rho_c r_c}{\Gamma(7-2a)} \left[\sum_{k=0}^{\infty} \frac{(-1)^k}{k!} \frac{\Gamma(-2a+2-4k)\Gamma(5+4k)}{\Gamma(\frac{1}{2}-k)} X^{2k} \right. \\ & \left. + \sum_{k=0}^{\infty} \frac{1}{4} \frac{(-1)^k}{k!} \frac{\Gamma(-\frac{1}{2}+\frac{a}{2}-\frac{k}{4})\Gamma(7-2a+k)}{\Gamma(\frac{a}{2}-\frac{k}{4})} X^{1-a+k/2} \right], \end{aligned} \quad (\text{F5})$$

where $X = r/r_c$ the two-dimensional radius scaled by the DZ characteristic radius (cf. Eq. (11)). If $a > 1$, this surface density is divergent in $X = 0$, while if $a < 1$ – which is the most frequent case –, one can retrieve the central density expressed in Eq. (29) as a consistency check. We recall that the surface density of a DZ profile truncated at the virial radius is $\Sigma(X) = \bar{\Sigma}(X) - \bar{\Sigma}(c)$.

F3 Cumulative mass and deflection angle

The series expansion of $\bar{\mathcal{M}}(X)$ can be obtained either by applying Eq. (F2) to the Fox H function of Eq. (34) or by directly integrating Eq. (F5):

$$\begin{aligned} \bar{\mathcal{M}}(X) = & \frac{4\pi^{3/2}\rho_c r_c^3}{\Gamma(7-2a)} \left[\sum_{k=0}^{\infty} \frac{(-1)^k}{k!} \frac{\Gamma(-2a+2-4k)\Gamma(5+4k)}{\Gamma(\frac{1}{2}-k)(k+1)} X^{2k+2} \right. \\ & \left. + \sum_{k=0}^{\infty} \frac{1}{4} \frac{(-1)^k}{k!} \frac{\Gamma(-\frac{1}{2}+\frac{a}{2}-\frac{k}{4})\Gamma(7-2a+k)}{\Gamma(\frac{a}{2}-\frac{k}{4})(\frac{3}{2}-\frac{a}{2}+\frac{k}{4})} X^{3-a+k/2} \right]. \end{aligned} \quad (\text{F6})$$

The series expansions of $\mathcal{M}(X) = \bar{\mathcal{M}}(X) - \bar{\mathcal{M}}(c)$, the deflection angle $\bar{\alpha}(X) = \bar{\mathcal{M}}(X)/\pi r_c^2 \Sigma_{\text{crit}} X$, and $\alpha(X) = \bar{\alpha}(X) - \bar{\mathcal{M}}(c)/\pi r_c^2 \Sigma_{\text{crit}} X$ can be deduced from Eq. (F6).

F4 Deflection potential

For a thin axially-symmetric lens, the deflection potential such that the scaled deflexion angle $\alpha = \nabla\psi$ is

$$\psi(X) = 2 \int_0^X x\kappa(x) \ln\left(\frac{X}{x}\right) dx \quad (\text{F7})$$

(Schneider et al. 1992, Eq. (8.8)). Injecting Eq. (30) and following similar steps as for Eq. (34) yields

$$\bar{\psi}(X) = \frac{2\sqrt{\pi}\rho_c r_c}{\Gamma(7-2a)\Sigma_{\text{crit}}} X^3 H_{4,4}^{2,3} \left[\begin{matrix} (-6, 4), (-\frac{1}{2}, 1), (-\frac{1}{2}, 1), (0, 1) \\ (-\frac{1}{2}, 1), (-2a, 4), (-\frac{3}{2}, 1), (-\frac{3}{2}, 1) \end{matrix} \middle| X^2 \right] \quad (\text{F8})$$

for an untruncated DZ profile. As for the cumulative mass, the series expansion of $\bar{\psi}(X)$ can be obtained either by applying Eq. (F2) to the Fox H function of Eq. (F8) or by directly injecting Eq. (F5) into Eq. (F7), yielding

$$\begin{aligned} \bar{\psi}(X) = & \frac{2\sqrt{\pi}\rho_c r_c}{\Gamma(7-2a)\Sigma_{\text{crit}}} \left[\sum_{k=0}^{\infty} \frac{(-1)^k}{k!} \frac{\Gamma(-2a+2-4k)\Gamma(5+4k)}{\Gamma(\frac{1}{2}-k)(1+k)^2} X^{2k+2} \right. \\ & \left. + \sum_{k=0}^{\infty} \frac{1}{4} \frac{(-1)^k}{k!} \frac{\Gamma(-\frac{1}{2}+\frac{a}{2}-\frac{k}{4})\Gamma(7-2a+k)}{\Gamma(\frac{a}{2}-\frac{k}{4})(\frac{3}{2}-\frac{a}{2}+\frac{k}{4})^2} X^{3-a+k/2} \right]. \end{aligned} \quad (\text{F9})$$

For a DZ profile truncated at the virial radius, the deflection potential is $\psi(X) = \bar{\psi}(X) - X^2 \bar{\Sigma}(c)/\Sigma_{\text{crit}}$, whose series expansion can be deduced from Eqs. (F5) and (F9). The associated Fermat potential $\phi(x, y) = (x - y)^2/2 - \psi(x)$ and its series expansion can be similarly deduced.

F5 Average surface density

As previously, the average surface density for an untruncated DZ profile yields

$$\begin{aligned} \bar{\bar{\Sigma}}(X) = & \frac{4\sqrt{\pi}\rho_c r_c}{\Gamma(7-2a)} \left[\sum_{k=0}^{\infty} \frac{(-1)^k}{k!} \frac{\Gamma(-2a+2-4k)\Gamma(5+4k)}{\Gamma(\frac{1}{2}-k)(1+k)} X^{2k} \right. \\ & \left. + \sum_{k=0}^{\infty} \frac{1}{4} \frac{(-1)^k}{k!} \frac{\Gamma(-\frac{1}{2}+\frac{a}{2}-\frac{k}{4})\Gamma(7-2a+k)}{\Gamma(\frac{a}{2}-\frac{k}{4})(\frac{3}{2}-\frac{a}{2}+\frac{k}{4})} X^{1-a+k/2} \right], \end{aligned} \quad (\text{F10})$$

while it is $\bar{\Sigma}(X) = \bar{\bar{\Sigma}}(X) - X\bar{\bar{\Sigma}}(c)$ for a DZ profile truncated at the virial radius. Expressions for the lensing shear $\gamma(X) = [\bar{\Sigma}(X) - \Sigma(X)]/\Sigma_{\text{crit}}$ and the magnification $\mu(X) = [(1 - \kappa(X))^2 - \gamma^2(X)]^{-1}$ can be deduced from Eqs. (F5) and (F10).

APPENDIX G: MASS-DEPENDENT PRESCRIPTIONS

Figs. G1 and G2 complement Section 4.2 by comparing the DM density and circular velocity profiles resulting directly from the mass-dependent prescriptions of Section 4.1 (without leaving the concentration free as in Section 4.3) for the eight fiducial NIHAO haloes at different masses shown in Fig. 3 with their simulated profiles. The two shape parameters s_1 and c_2 of the DZ profiles shown in Figs. G1 and G2 are set by the fitting functions shown in Fig. 9, expressed in Eqs. (45) and (49), and whose best-fit parameters are given in Table 1. The figures also show the Di Cintio+ mass-dependent prescriptions, for which the four shape parameters of the double power-law profile (a, b, g in Eq. (2) and c_2) are obtained from the stellar and halo masses as indicated in the Appendix of Di Cintio et al. (2014b). Fig. G3 systematically compares the rms

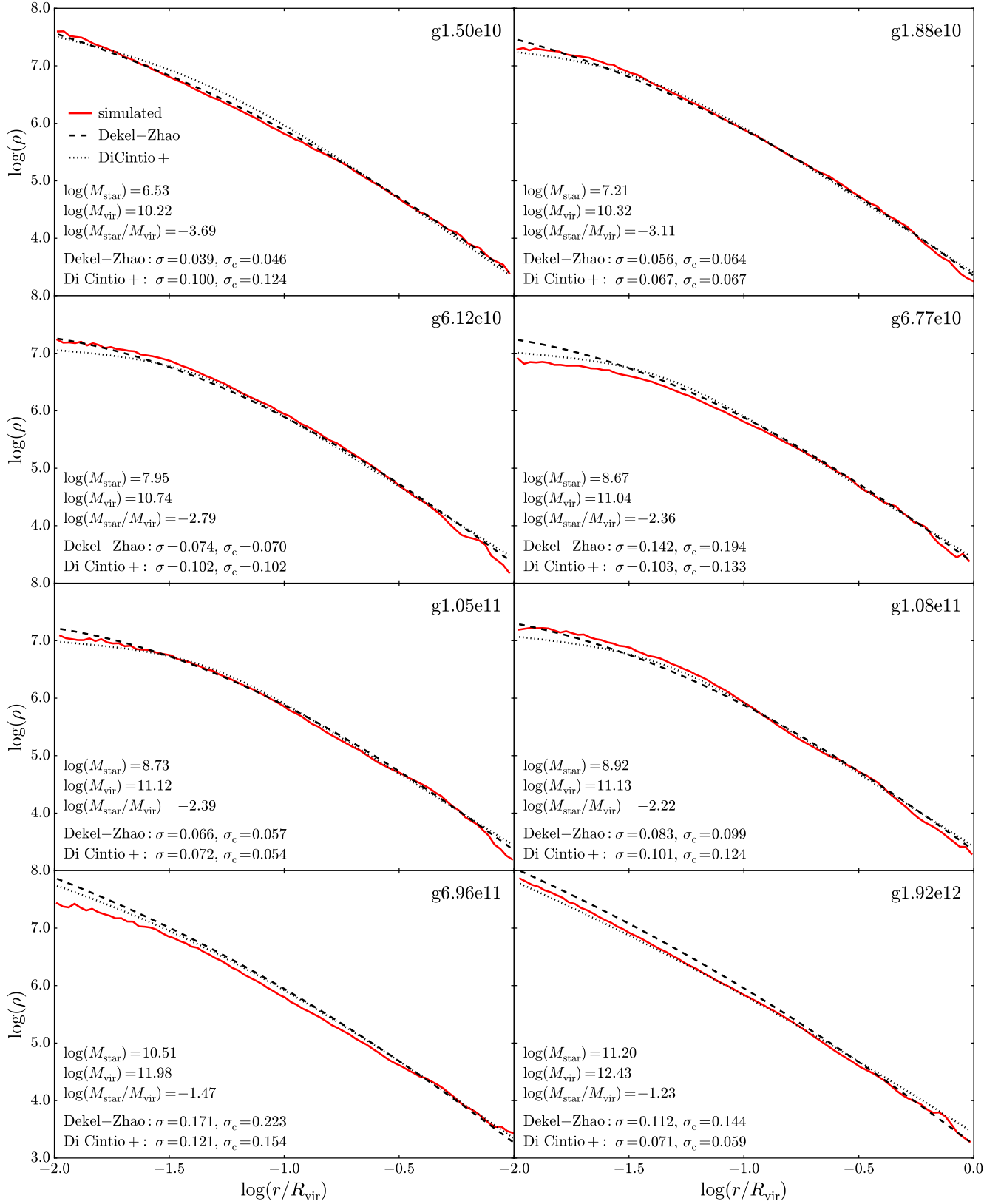


Figure G1. The dark matter density profiles at $z = 0$ of the 8 arbitrary NIHAO galaxies shown in Fig. 3 (plain red line) with their current DZ (dashed) and DiCintio+ (dotted) mass-dependent prescriptions. The masses M_{star} , M_{vir} , $M_{\text{star}}/M_{\text{vir}}$ and the rms errors σ and σ_c are indicated.

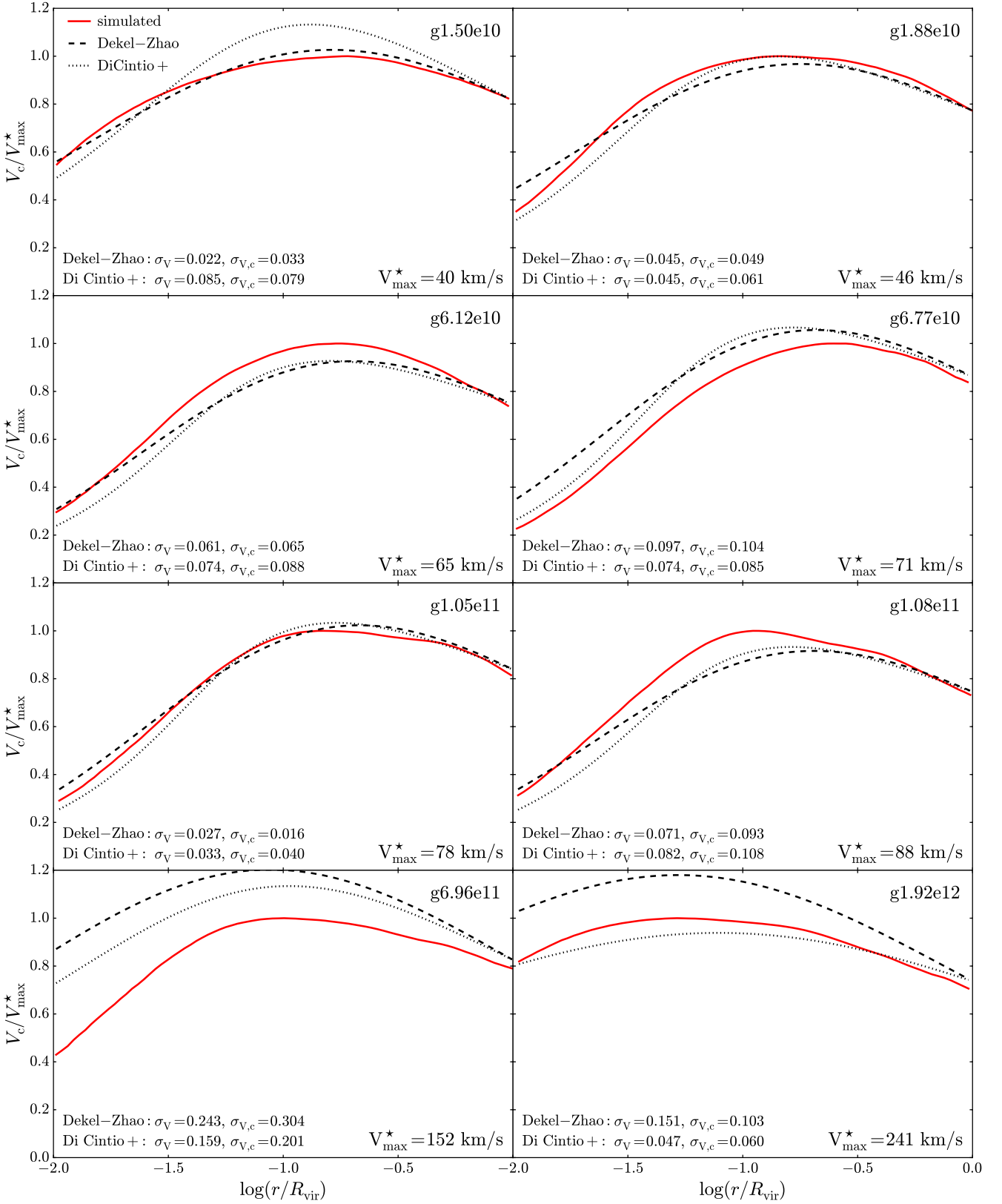


Figure G2. Dark matter circular velocity profiles, $V_c(r) = \sqrt{GM(r)/r}$, of the eight $z = 0$ NIHAO galaxies shown in Fig. 3 (plain red line) together with those inferred from the current DZ and Di Cintio+ mass-dependent prescriptions (dashed and dotted lines, respectively). The velocity of each galaxy is normalized to its maximum value V_{\max}^* , which is an increasing function of mass.

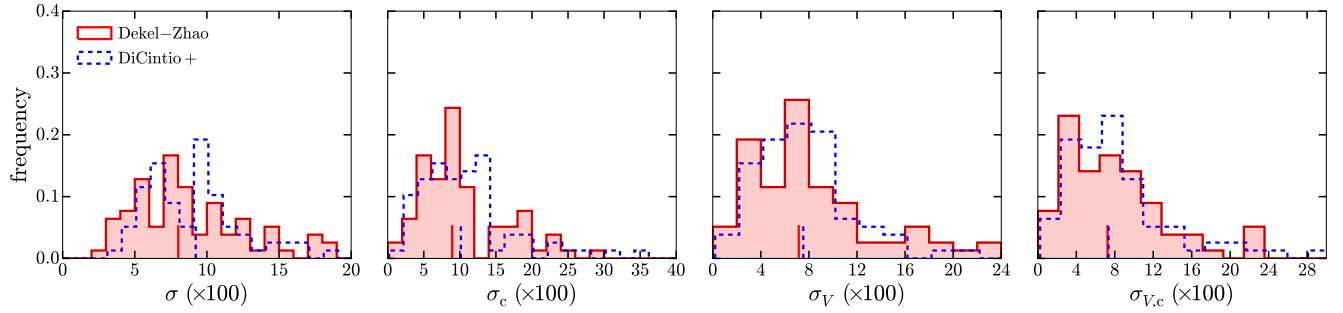


Figure G3. Comparison between the current DZ (plain red line) and *Di Cintio+* (blue dashed line) mass-dependent prescriptions in terms of their rms errors in $\log \rho$ and V_c/V_{\max} over the ranges $0.01R_{\text{vir}} - R_{\text{vir}}$ and $0.01R_{\text{vir}} - 0.1R_{\text{vir}}$ for all NIHAO galaxies at $z = 0$. The median values for the two prescriptions, which are highlighted by vertical lines above the x-axis, respectively yield 0.080 & 0.092 for σ , 0.089 & 0.101 for σ_c , 0.072 & 0.075 for σ_V , 0.072 & 0.074 for $\sigma_{V,c}$. The standard deviations respectively yield 0.041 & 0.043 for σ , 0.060 & 0.064 for σ_c , 0.054 & 0.043 for σ_V , 0.058 & 0.055 for $\sigma_{V,c}$. The current prescription provides equivalent (or marginally better fits) to the DM density profile and the circular velocity profile than the *Di Cintio+* prescriptions.

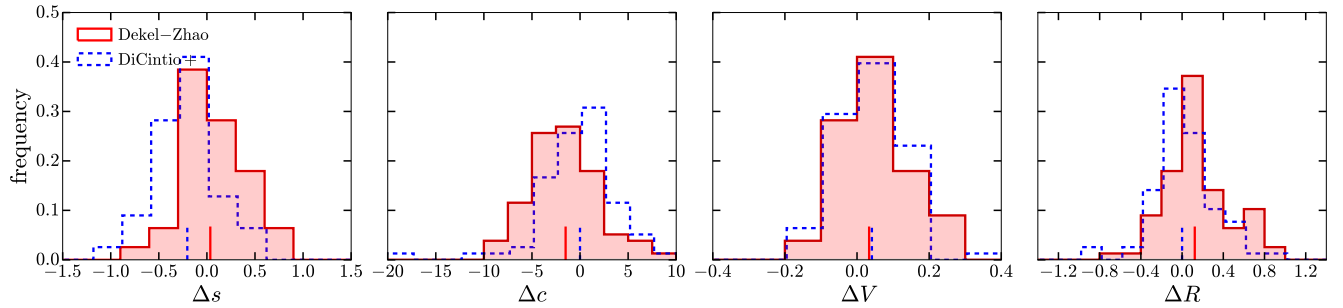


Figure G4. Comparing the current DZ and the *Di Cintio+* mass-dependent prescriptions: inner slope and concentration differences, $\Delta s = s_{1,\text{model}} - s_1^*$ and $\Delta c = c_{2,\text{model}} - c_2^*$, as well as the maximum velocity and radius relative differences, $\Delta V = (V_{\text{max,model}} - V_{\text{max}}^*)/V_{\text{max}}^*$ and $\Delta R = (R_{\text{max,model}} - R_{\text{max}}^*)/R_{\text{max}}^*$, between the current DZ (plain red line) and the *Di Cintio+* (blue dashed line) mass-dependent prescriptions and the simulated profiles for all $z = 0$ NIHAO galaxies simulated with baryons. The median values for the two prescriptions, which are highlighted by vertical lines above the x-axis, respectively yield 0.03 & -0.20 for Δs , -1.5 & -0.0 for Δc , 0.034 & 0.041 for ΔV , 0.123 & 0.00 for ΔR . The standard deviations respectively yield 0.31 & 0.31 for Δs , 8.7 & 9.3 for Δc , 0.089 & 0.086 for ΔV , 0.312 & 0.298 for ΔR . The current prescription provides fits whose accuracy is comparable to the *Di Cintio+* prescription despite having two shape parameters instead of four (concentration included).

of the residuals between the simulated density and circular velocity profiles and those stemming from the current DZ and *Di Cintio+* prescriptions. Figs. G4 further shows the distributions of Δs , Δc , ΔV and ΔR resulting from the two mass-dependent prescriptions.

APPENDIX H: ADDITIONAL FIGURES

H1 Measuring the inner slope and concentration

Fig. H1 illustrates how the inner slope s_1^* and the concentration c_2^* are measured from the simulated density and logarithmic slope profiles. As explained in Section 3.2.2, s_1^* is the average slope between $0.01R_{\text{vir}}$ and $0.02R_{\text{vir}}$, c_2^* corresponds to the radius where the logarithmic slope equals 2. To define c_2^* , the logarithmic slope profile is smoothed with a Savitsky-Golay filter with maximum window size. This window size choice maximizes the smoothing in order to have a measure of c_2^* that is not affected by the slope fluctuations, as exemplified in the figure.

H2 Density residuals

Figs. H2, H3, and H4 respectively show the residuals (in $\log \rho$) between the simulated dark matter density profiles and (i) the DZ, Einasto and gNFW fits (Fig. 3), (ii) the current DZ and *Di Cintio+*

mass-dependent prescriptions (Fig. G1), and (iii) the density profiles inferred from one-parameter DZ and *Di Cintio+* fits to the rotation curves (Fig. 11). As stated in Sections 3.2, 4.2, and 4.3, the DZ profile provides significantly better fits to simulated density profiles than the Einasto profile and marginally better fits than the gNFW profile; its mass-dependent prescriptions are as successful or even marginally better than the *Di Cintio+* ones. We note a certain degree of stochasticity in the radial dependence of the residuals in $\log \rho$.

H3 Velocity residuals

Figs. H5, H6, and H7 respectively show the residuals between the simulated rotation curves and (i) those stemming from DZ, Einasto and gNFW fits to the density profiles (Fig. 4), (ii) the current DZ and *Di Cintio+* mass-dependent prescriptions (Fig. G2), and (iii) one-parameter DZ and *Di Cintio+* fits to the rotation curves (Fig. 12). As stated in Sections 3.2, 4.2, and 4.3, the DZ profile provides significantly better fits to simulated density profiles than both the Einasto and the gNFW profiles; its mass-dependent prescriptions are as successful or even marginally better than the *Di Cintio+* ones.

This paper has been typeset from a \LaTeX file prepared by the author.

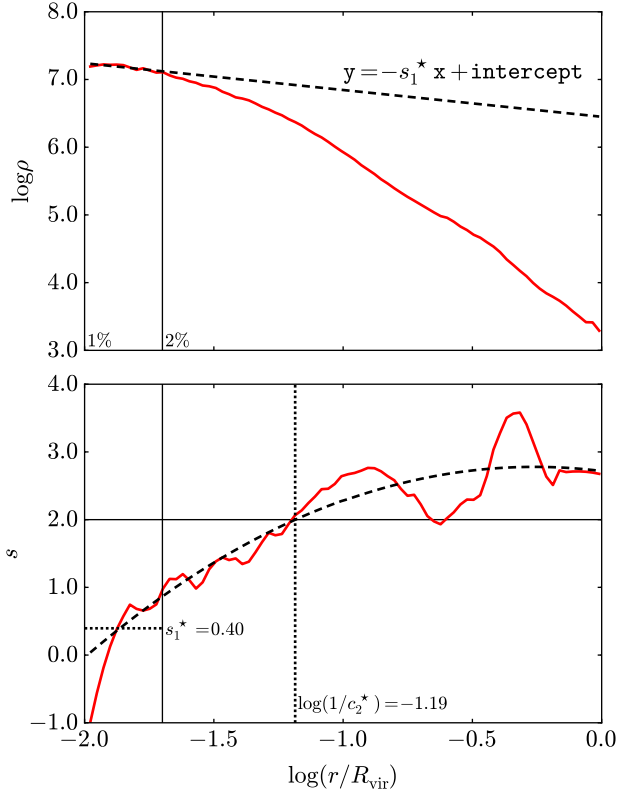


Figure H1. Measurement of the inner slope s_1^* and concentration c_2^* of NIHAO halo g1.08e11 at $z = 0$ from its density and logarithmic slope profiles. The upper panel shows the density profile (plain red line). A linear least-square fit to $\log \rho$ between $0.01R_{\text{vir}}$ and $0.02R_{\text{vir}}$ (dashed line) enables to determine s_1^* the average inner slope in this radius range. The lower panel shows the corresponding logarithmic slope s , obtained with a Savitzky-Golay smoothing filter (Savitzky & Golay 1964, implemented as `scipy.signal.savgol_filter` in `scipy`) with a polynomial order $n = 3$. The plain red line correspond to a Savitzky-Golay window size $w = 11$, the black dashed line to a smoother curve obtained with a maximal window size ($w = 77$ here). The concentration c_2^* corresponds to the radius $r_2^* = R_{\text{vir}}/c_2^*$ where the smooth curve intersects the line $y = 2$.

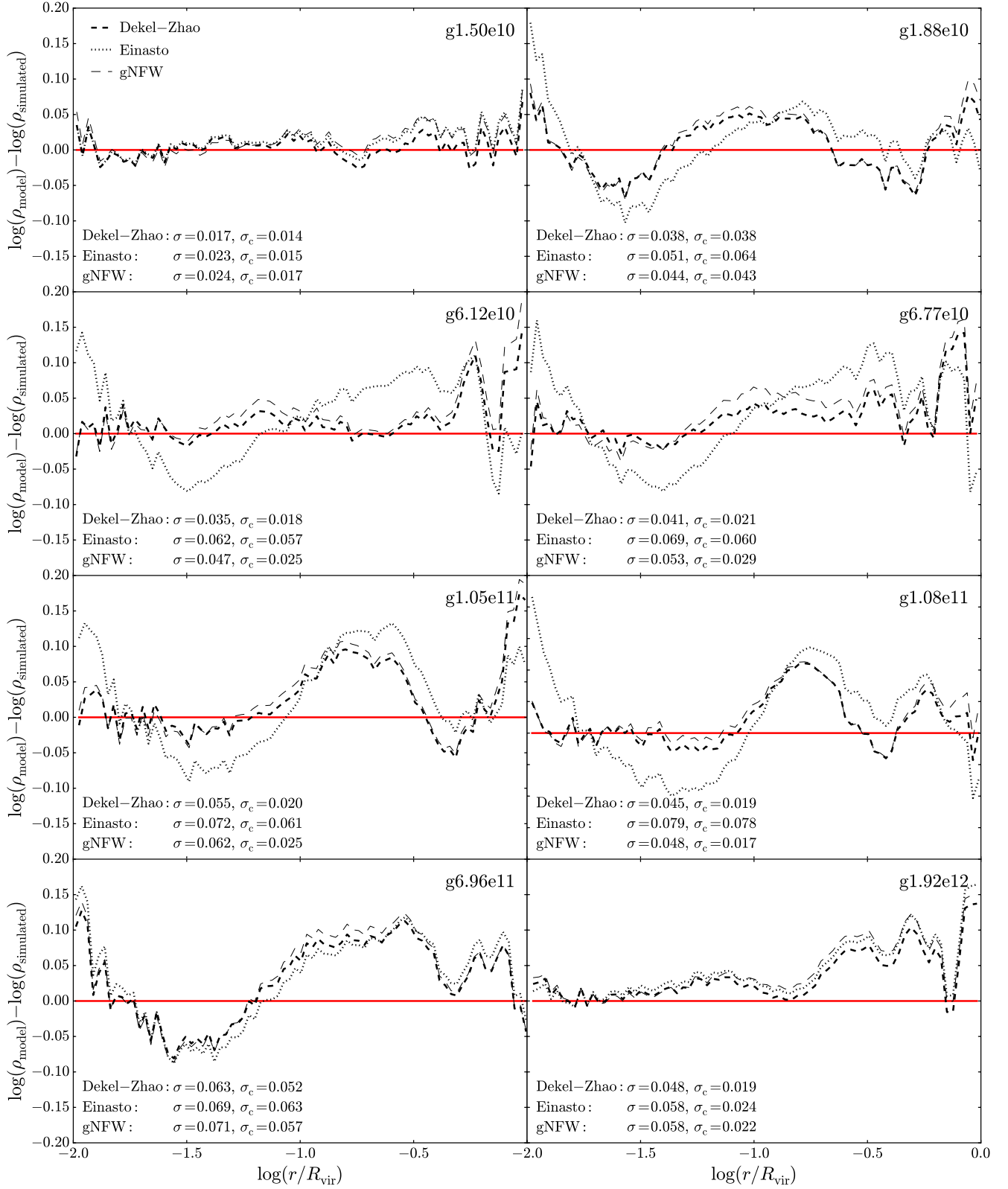


Figure H2. Residuals for the dark matter density profile DZ, Einasto and gNFW least-square fits shown in Fig. 3, respectively traced as dashed, dotted, and thin dashed black lines. The rms errors σ and σ_{center} are indicated.

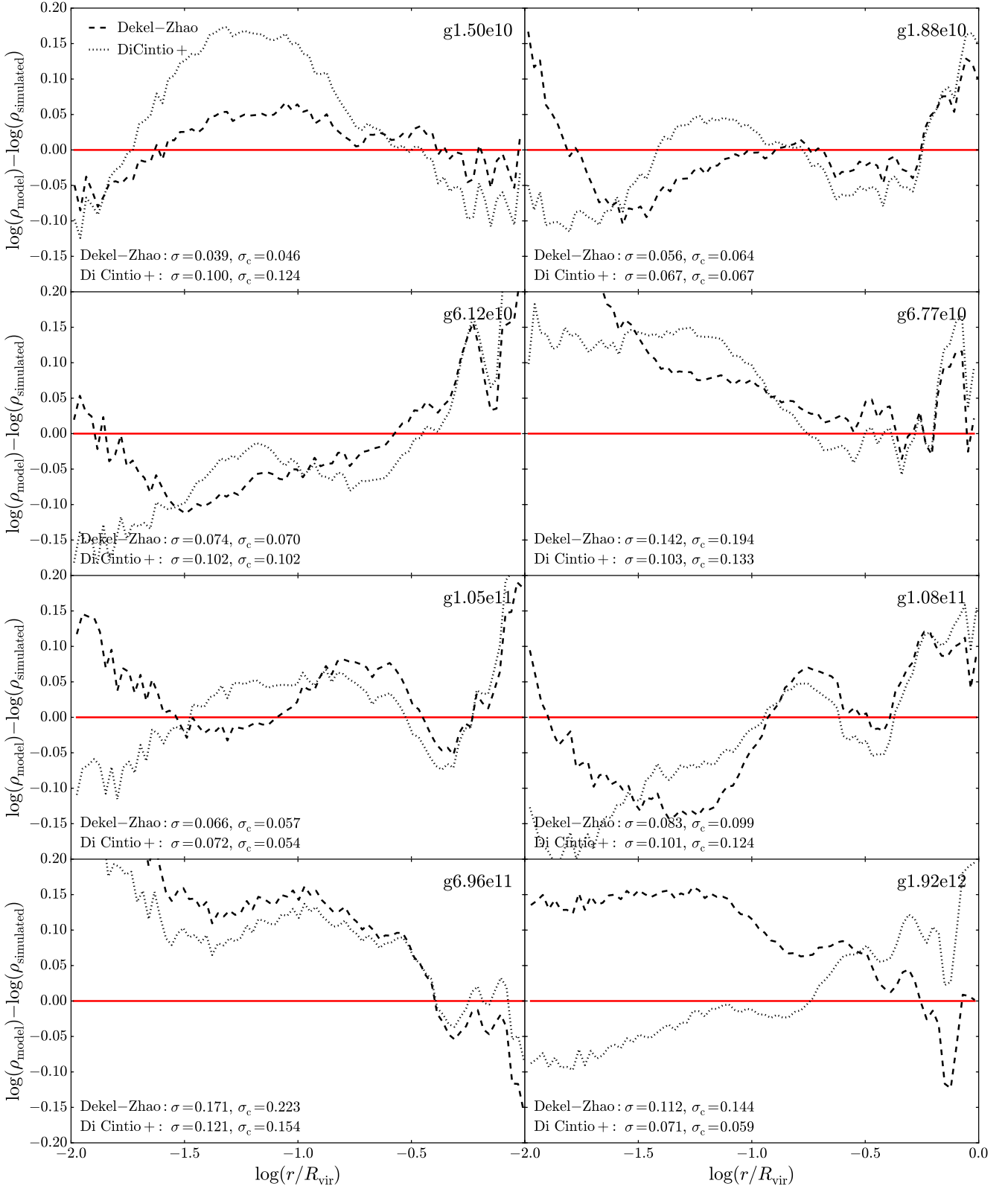


Figure H3. Residuals between the simulated density profiles shown in Fig. G1 and the current DZ (dashed) and Di Cintio+ (dotted) mass-dependent prescriptions. The rms errors σ and σ_{center} are indicated.

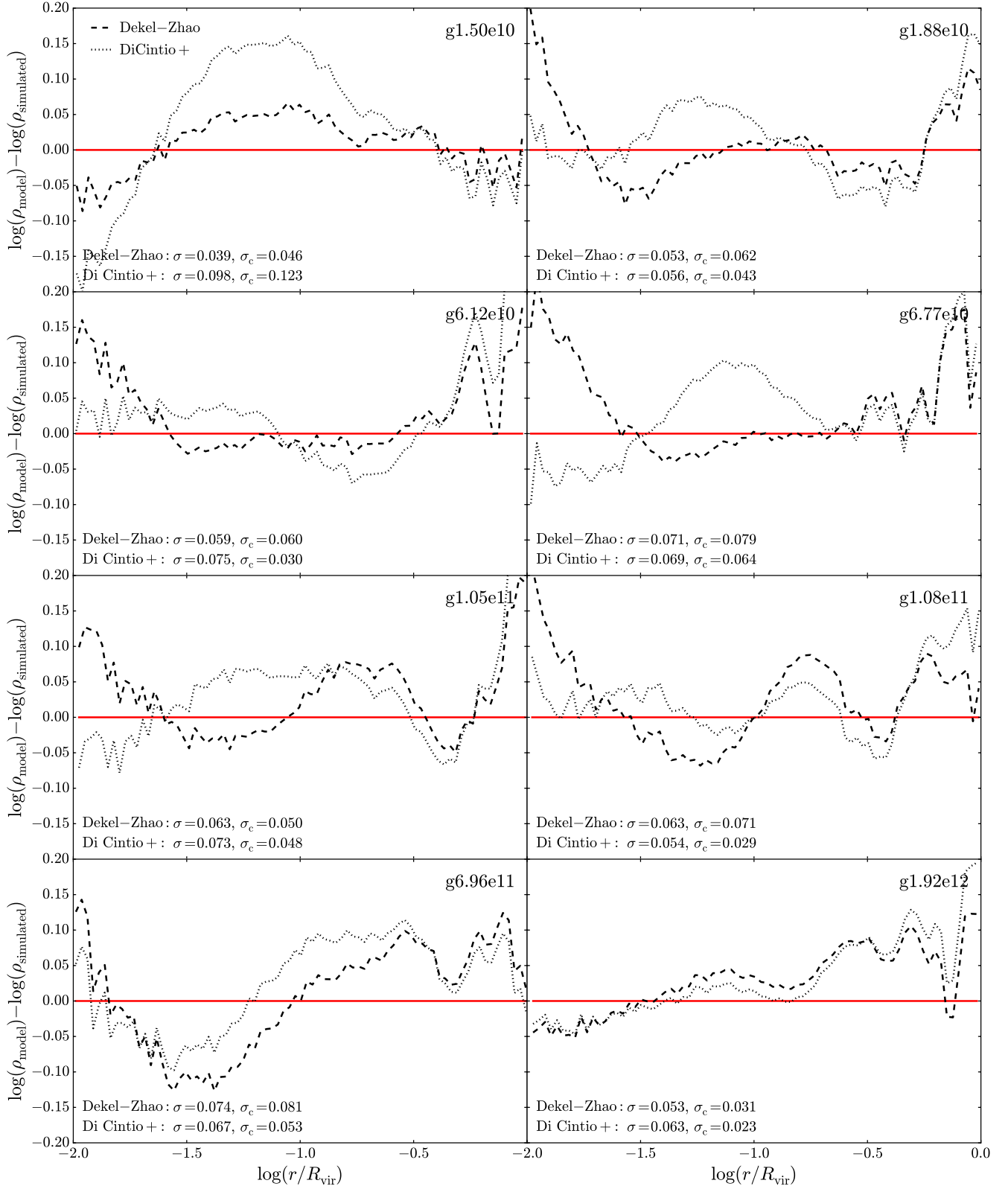


Figure H4. Residuals between the simulated density profiles shown in Fig. 11 and those stemming from one-parameter DZ (dashed) and Di Cintio+ (dotted) fits to the rotation curves. The rms errors σ and σ_{center} are indicated.

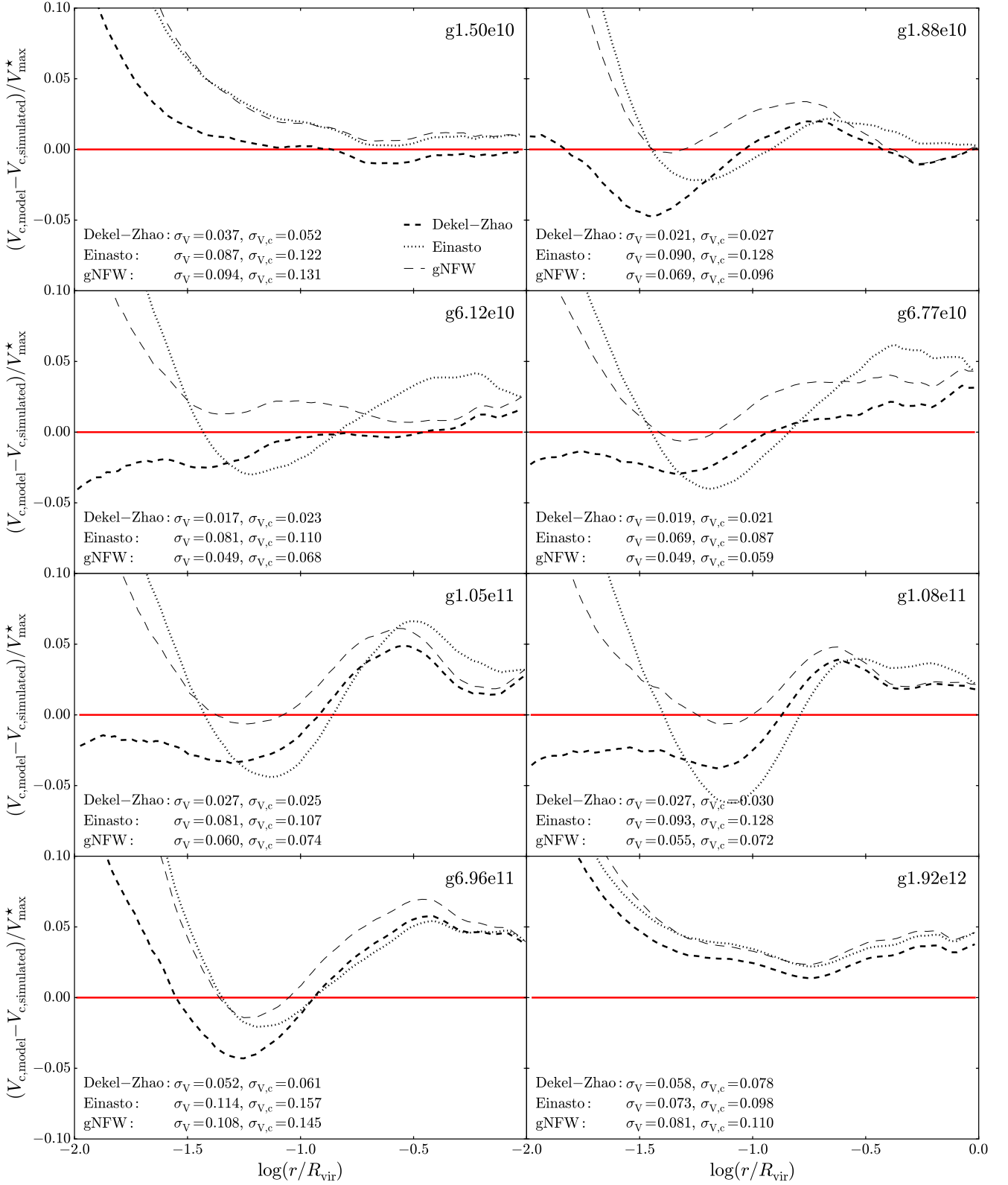


Figure H5. Residuals between the simulated rotation curves and those inferred from DZ (dashed), Einasto (dotted) and gNFW (thin dashed) fits to the density profiles shown in Fig. 4. The rms errors σ and σ_{center} are indicated.

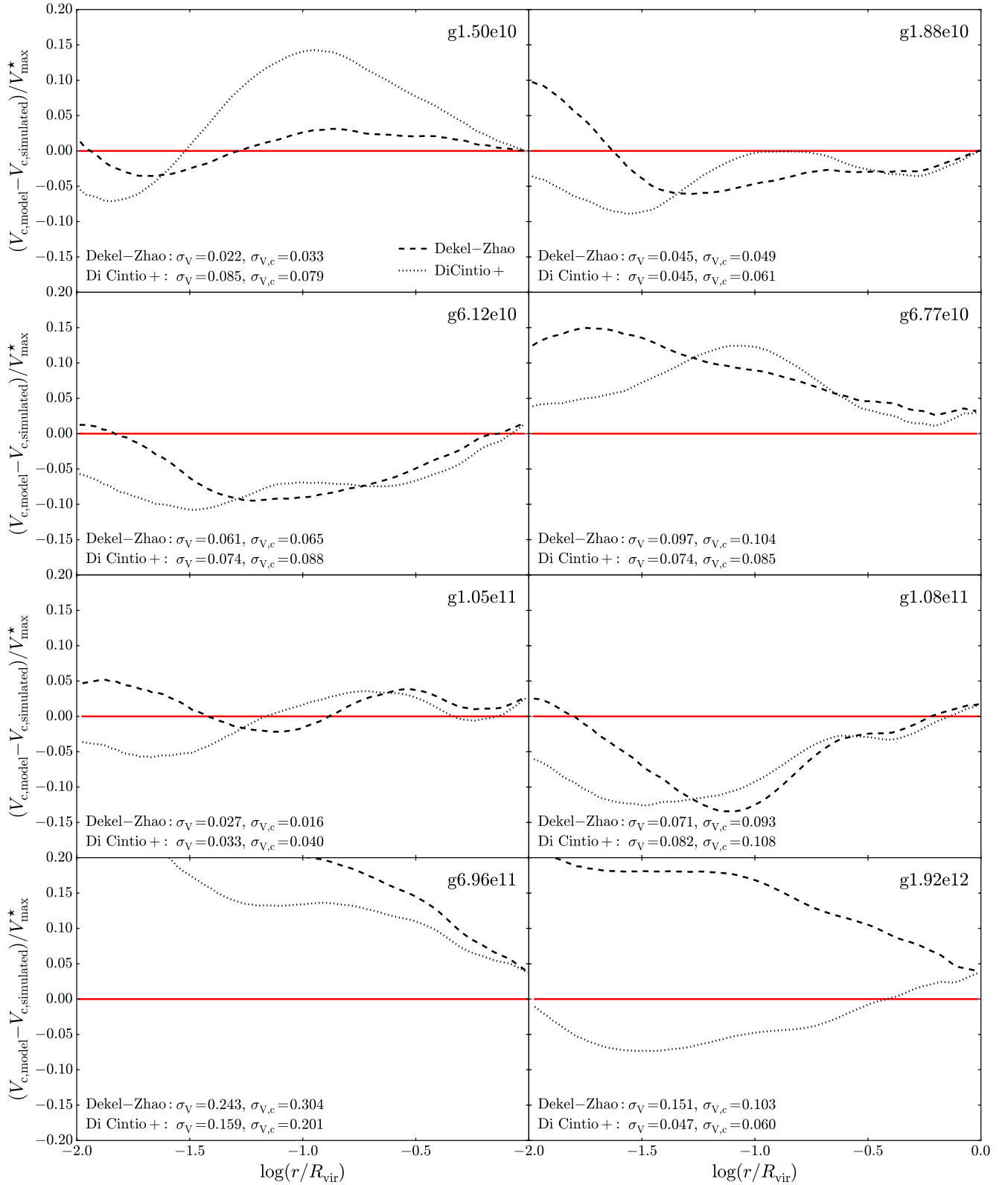


Figure H6. Residuals between the simulated rotation curves and the current DZ (dashed) and Di Cintio+ (dotted) mass-prescriptions shown in Fig. G2. The rms errors σ and σ_{center} are indicated.

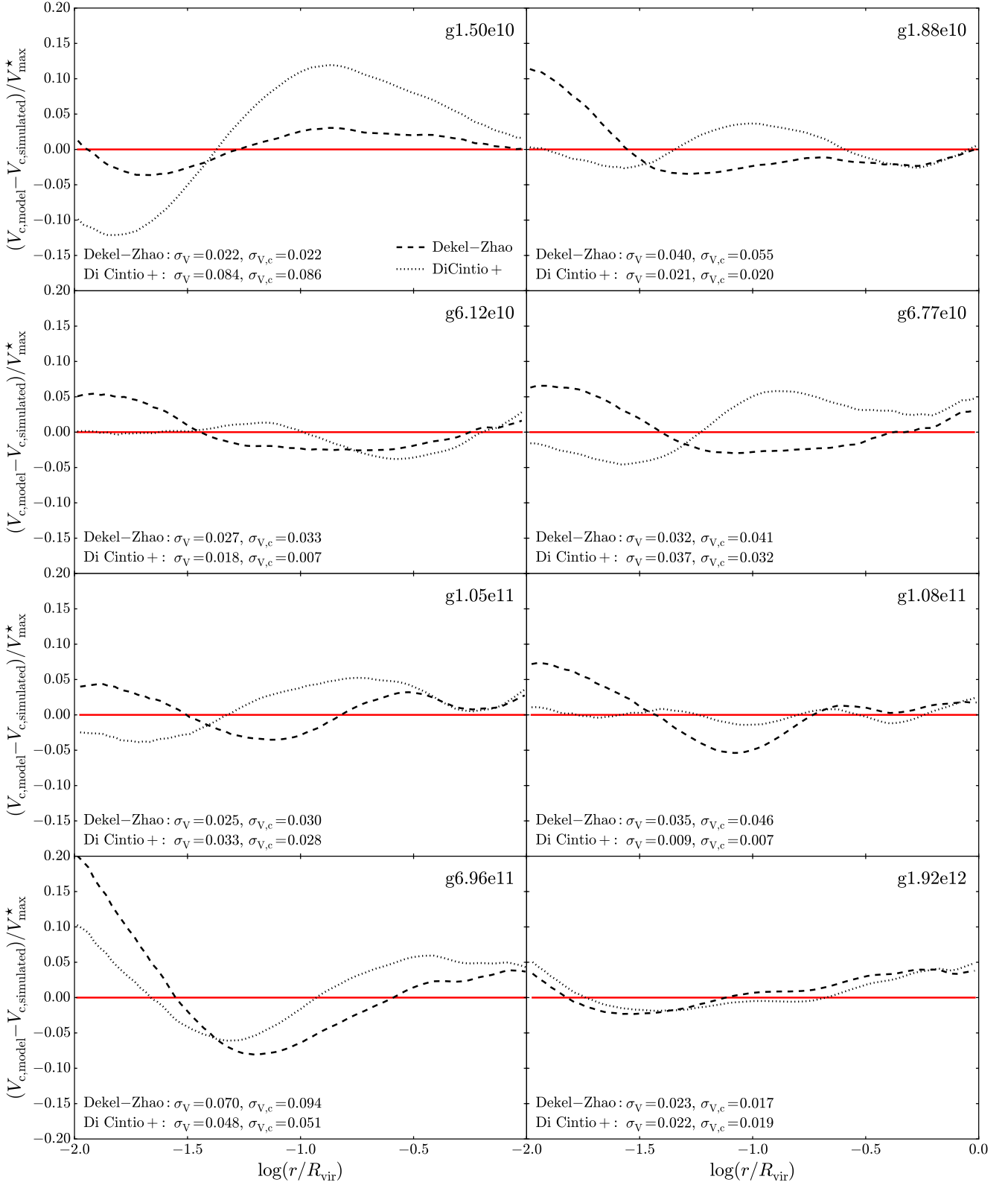


Figure H7. Residuals between the simulated rotation curves and the one-parameter DZ (dashed) and Di Cintio+ (dotted) fits to them shown in Fig. 12. The rms errors σ and σ_{center} are indicated.